4/17 3

UCRL-50051-77-4

MAGNETIC FUSION ENERGY QUARTERLY REPORT
October through December 1977

Scientific Editor: M. A. Harrison
General Editor: C. K. McGregor

MASTER

February 28, 1978

Work performed under the auspices of the U.S. Department of Energy by the UCLLL under contract number W-7405-ENG-48

LAWRENCE
LIVERMORE
LABORATORY
University of California Livermore

LAWRENCE LIVERMORE LABORATORY

[illegible]

UCRL-50051-77-4

MAGNETIC FUSION ENERGY QUARTERLY REPORT
October through December 1977

Scientific Editor: M. A. Harrison
General Editor: C. K. McGregor

MS. date: February 28, 1978

PREFACE

Effective with the beginning of FY 1978, the *Magnetic Fusion Energy Annual Report* for the Magnetic Fusion Energy (MFE) Program at the Lawrence Livermore Laboratory (LLL) is being replaced by quarterly reports; this is the first in the new series.

Our intent is to provide a timely summary of activities within the MFE Program at LLL. In a given *Quarterly*, not all MFE projects are necessarily represented. Throughout, details are kept to a minimum; readers desiring additional information are encouraged to read referenced documents or to contact the individuals engaged in the projects.

The information in each *Quarterly* is presented in the same sequence as in the *Form 189* submissions prepared for the U.S. Department of Energy; the three main sections are Open Confinement Systems, Development and Technology, and Applied Plasma Physics. Each of these sections is introduced by an overall statement of the goals and purposes of the groups reporting in it. As appropriate within each section, statements of the goals of individual programs and projects are followed by articles containing summaries of significant recent activity and descriptive text.

The last *Quarterly* in each fiscal year will contain a list of all publications and presentations prepared by MFE personnel during that year.

CONTENTS

MAGNETIC FUSION ENERGY QUARTERLY REPORT
October through December 1977

1. OPEN CONFINEMENT SYSTEMS

Lawrence Livermore Laboratory (LLL) has primary national responsibility for magnetic mirror programs, an approach pioneered here since the early 1950's. A goal of LLL's magnetic fusion energy (MFE) program is to provide the technology to develop a continuously operating fusion reactor. The heart of this reactor will be a plasma confined by magnetic mirror geometry and continuously sustained by injection of beams of energetic neutral atoms (such as deuterium).

There are three confinment systems now in operation or under construction at LLL, the 2XIIB, the Tandem Mirror Experiment (TMX), and the Mirror Fusion Test Facility (MFTF).

- 2XIIB relies on pulsed magnetic fields to confine a hot, dense plasma for a short time. It features C-shaped magnetic coils that form the confining magnetic field. Their unique shape (in what is known as a yin-yang geometry) stabilizes the confined plasma by creating a magnetic field (a magnetic well) that increases in every direction from the plasma center.
- In 1976, we proposed a new idea the tandem mirror concept. A tandem mirror reactor would contain a long solenoidal magnet terminated at both ends by conventional mirror cells. These cells would act as "end plugs" to prevent plasma leakage out the ends of the solenoid. The TMX is being constructed to test the principles of this concept.
- The MFTF now being constructed will bridge the physics and engineering gaps between present experiments and an experimental fusion reactor planned for operation by 1990. The MFTF will use a superconducting magnet of yin-yang design (similar to the 2XIIB experiment). This magnet will be capable of continuous operation.

2XIIB

The 2XIIB magnetic mirror machine was built to study the scaling of plasma confinement with ion energy. We have raised the mean plasma ion energy to 13 keV and the peak energy confinement parameter $\bar{n}\tau_i$ [illegible] 10 [illegible] cm [illegible] s. After reaching high betas ($\beta \approx 8\pi nW/B_{vac}^2$), experiments attempting to achieve field reversal reached a field-reversal factor $\Delta B/B$ [illegible] 0.9. Experiments attempting to improve the microstability of mirror-confined plasma and to further increase beta are underway.

Field-Reversal Experiments With Variable Quadrupole Magnetic Field Strength

W. C. Turner

Field-reversal experiments were conducted by varying the quadrupole magnetic field strength. Results indicate no rapid increase in ion losses with increasing quadrupole field strength.

Our field-reversal experiments with variable quadrupole magnetic field strength were motivated by work at Cornell using the relativistic electron compression experiment (RECE-Berta) electron-ring (E-ring) device. In those experiments, anomalous electron losses were observed to increase linearly with quadrupole field strength. Also E-ring decay rates up to five to six times the rate for ring loss due to collisional diffusion on background neutral density were measured. Although our 2XIIB experiments were conducted at even higher quadrupole field strength, they showed ion loss rates within a factor of two of electron drag and they did not show a linear dependence on quadrupole field strength. We conclude from these experiments that 2XIIB ion losses are not enhanced by a quadrupole magnetic field as are RECE-Berta electron losses.

In the 2XIIB experiment, we can vary the ratio of quadrupole field strength B_q to total field strength B_0 by varying the ratio of the current in the yin-yang coil to that of the solenoidal coils. The 2XIIB experiment is limited to a 0.4-T maximum solenoidal field strength and to a 0.83-T central yin-yang field strength. The lower limit of B_q is set by the need to maintain an adequate longitudinal mirror ratio. Experiments were performed in 2XIIB over the range 0.14 < $B_q' R_p / B_0$ < 0.29 with a constant 0.67-T central vacuum field and a constant 500-A neutral beam current. As can be seen in Figs. 1 and 2, the quadrupole field strengths investigated in 2XIIB are two to four times the RECE-Berta maximum.

Figure 1 shows the volume-average energy confinement parameter vs the quadrupole field strength evaluated at R_p, the plasma radius defined as the Gaussian e-folding radius, i.e., $n(r) = n \exp(-r^2/R_p^2)$. Such volume-averaged $\langle n\tau_E \rangle$ are a factor of 2 to 3 lower than those obtained by multiplying central density n by average ion energy lifetime τ_E. Figure 1 shows that $n\tau_E$ is approximately constant and does not increase linearly with $B_q' R_p / B_0$. Furthermore, it is seen in Fig. 2 that electron temperature was about 100 eV, from which we expect that $n\tau_E \approx 4 \times 10^{10}$ because of electron drag. The factor of 2 difference in $n\tau_E$ is attributed to quasilinear diffusion losses and to radial electron temperature profiles. The factor of 2 is considerably smaller than the factor of 10 to 20 one could extrapolate from the quadrupole T-ring experiments. Consequently, we have concluded that 2XIIB ion losses are not similarly enhanced by a quadrupole magnetic field.

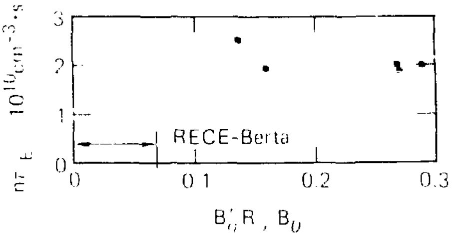

Fig. 1. Volume-averaged ion energy confinement versus quadrupole field strength, where B_{total} = 0.67 T and $B_q = B_q' R_p$.

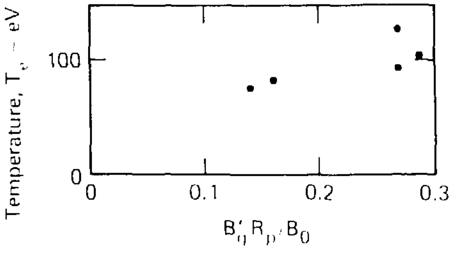

Fig. 2. Electron temperature versus quadrupole field strength.

Experiments with the Stabilizing Stream Located at the Edge of the Plasma

T. C. Simonen and J. H. Foote

Experiments were initiated with a stabilizing plasma stream supplied to the plasma boundary. These experiments showed that the plasma stream can be localized to a radius of ~6 cm, that at this location the stream can stabilize the drift-cyclotron loss-cone mode, and that the electron temperature increases from 90 eV to 140 eV.

We conducted field-reversal experiments in which the stabilizing plasma stream was located at the edge of the plasma rather than in the center as in previous experiments. These experiments were motivated by our desire to increase electron temperature in the center of the plasma and to thereby reduce the electron-drag cooling of hot ions in the center. For the results of these experiments, which were conducted at the beginning of this quarter, see Ref. 1. In summary, locating the stabilizing plasma streams at the edge of the plasma allowed the electron temperature to reach 140 eV on a consistent basis. We recorded a few shots as high as 180 eV. The hot-ion lifetime did not continue to improve above ~100 eV; we attribute this to an increase in ion cyclotron activity.

In an attempt to reduce these ion cyclotron fluctuations, we first located 2-in.-diam, deuterium-loaded-titanium washer guns (rather than the usual 1/2-in.-diam guns) at the mirror throats. Our aim was to supply additional streaming plasma to improve microstability, a method which had been successful in the past. The 2-in.-diam plasma guns broke when located near the mirror throat, presumably because of the mechanical shock imparted to the guns when the yin-yang magnet was fired. We therefore stopped using the large 2-in.-diam reentrant guns.

We then shifted experimental priority to examining the use of edge streams for application to experiments with large-diameter plasma. The experimental milestone calls for creating plasmas of size $R_p/a_i \approx 5$ to 10. Among the experimental objectives of these experiments are

- To create larger plasmas by beam aiming and streaming-plasma location, and
- *To then investigate microstability, and ion and electron confinement in larger-diameter plasmas*

As an initial step during [illegible] measurements of mapping of streaming plasma [illegible] into the center of 2XIIB.

Calculated Projections of Streaming-Gun Emitting Areas Along Magnetic-Field Lines to the 2XIIB Midplane. We have calculated the projection of the emitting area of a titanium washer-stack streaming-plasma gun along magnetic-field lines to the 2XIIB midplane for various possible gun positions and emitting areas. Figure 3 and Table 1 summarize the positions and diameters of the emitting areas used. Figure 4 shows the resulting mappings to the midplane. Results for the east end of 2XIIB are shown; they represent the west end if the horizontal and vertical planes are interchanged (the east magnetic-field line fan is vertical; the west fan is horizontal).

Positions A, B and C in Fig. 3 correspond to the standard 2-in.-diam streaming plasma gun mounted at the outer end of the east vacuum tank. Position D represents a 1 2-in.-diam reentrant gun placed near the mirror region.

The mappings depend on the relative values of the pulsed and dc guide fields. For the projections in Fig. 4, the magnetic field at the center of 2XIIB is 0.65 T, [illegible]

Table 1. Center positions and diameters of emitting areas of streaming guns.

Position (see Figs. 3, 4)	x (cm)	y (cm)	z (cm)	Diameter (cm)
A	0	8	[illegible]	5.1
B	0	19	[illegible]	5.1
C	0	42	[illegible]	5.1
D	0	42	[illegible]	2.54

[illegible]

[illegible] suggest motion of the st[illegible] lines. Here we as[illegible] to the field lines w[illegible]

Measurement of Edge Streams. [illegible] we could map st[illegible] 2XIIB, we made two s[illegible]

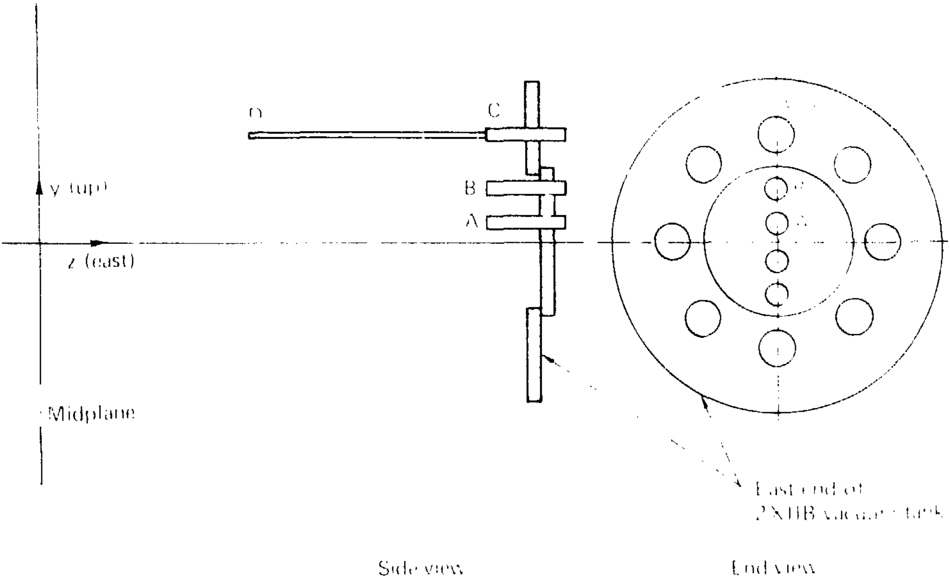

Fig. 3. Positions of streaming-plasma guns in mapping calculations.

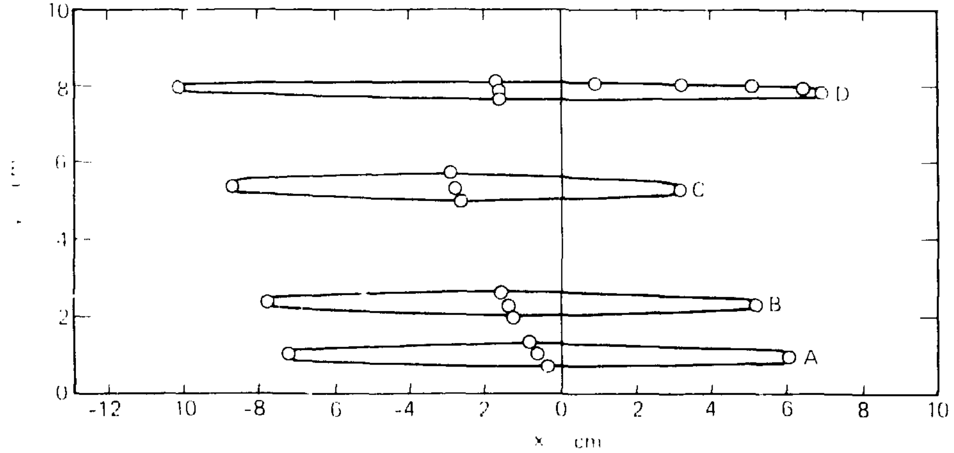

Fig. 4. Calculated projections to the midplane (z = 0 plane) of the emitting areas of the various selected streaming guns. (B = 0.68 T at *the magnetic-well center, which includes 0.20 T from the guide field.) The circles are calculated values. Projections are not quite symmetric* with respect to the vertical plane because of asymmetries in the yin-yang coil windings.

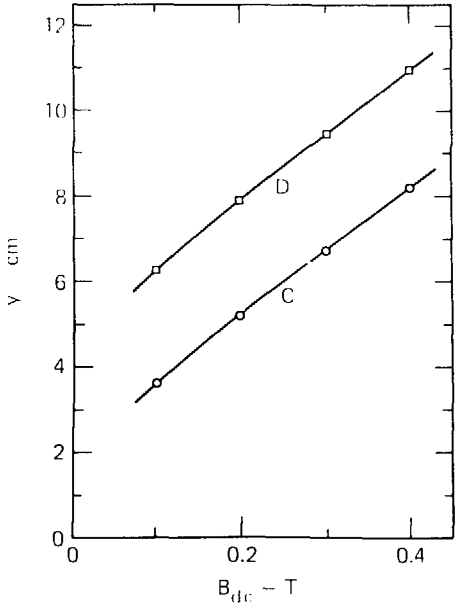

Fig. 5. Vertical position at midplane of center of plasma gun *projected from the east end of* **2XIIB**, *for gun locations C and D,* vs guide-field magnitude (yin-yang pulsed field is 0.48 T at the center of the magnetic well).

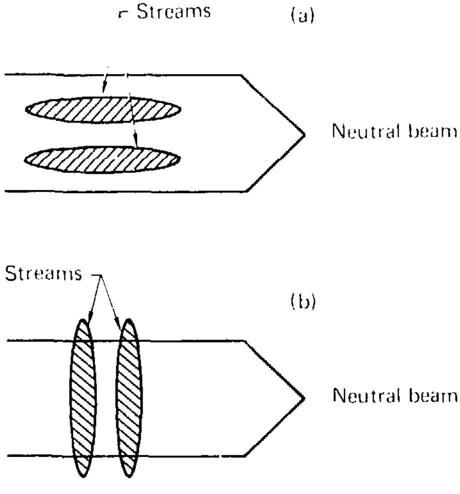

Fig. 6. Schematic of two measurements of streaming-plasma gun mapping: (a) spatial density profiles of horizontal streams (east guns) are measured with a vertical array of beam-attenuation detectors, and (b) spatial density profiles of vertical streams (west guns) are measured using horizontal H_α radiation from neutral-beam *atoms excited by the streaming* plasma.

using pairs of streaming-plasma guns at each end of 2XIIB. Beam-attenuation measurements made with 1.2-in.-diam reentrant streaming-plasma guns located at position D of Fig. 3 are shown in Fig. 7. Line density across the narrow dimension of the fan is ~1 × 10 [illegible] cm. The dc guide field was 0.2 T and the pulsed field was 0.47 T. The maximum stream *is located at −4 cm and +8 cm. More detailed Lyman-*α radiation scans [Fig. 6(b)] also show that the peaks were separated by 12 cm. Calculations shown in Fig. 5 indicate a peak separation of 15.5 cm. The plasma streams are centered 2 cm above axis. This is a consistent offset for which we have no explanation at the present time.

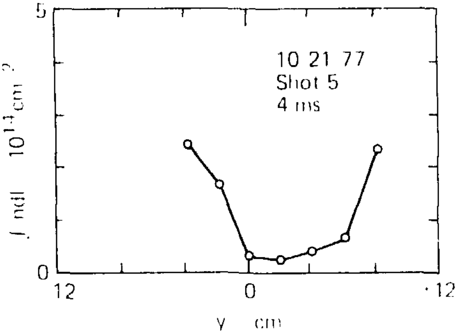

Fig. 7. Beam attenuation line density profile for 1.2-in.-diam reentrant streaming-plasma guns at one end of 2XIIB.

We thus conclude the following:

- Streaming plasma can be fed to the edge of the plasma along magnetic field lines.
- It does not flute inward to the minimum-|B| position, presumably because of line tying to the gun.

With four 2-in.-diam guns located in position C (Fig. 3), the radial beam attenuation line density profile is as shown in Fig. 8.

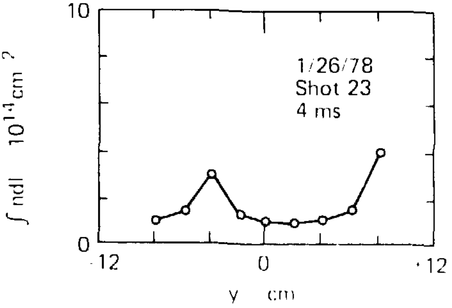

Fig. 8. Beam attenuation line density profile for 2-in.-diam streaming-plasma guns at both ends of 2XIIB.

The application [illegible] plug into the edge [illegible] field reversal quadrupole experiment discussed in the preceding article and will [illegible] large-diameter experiments [illegible] the next progress report.

Analysis of Data From Operation of 2XIIB Yin-Yang Magnet With a Flat-Top Electrolytic Power Supply

T. C. Simonen

By analyzing earlier experimental results, we found that 2XIIB operation with the slow-rising ([illegible] *10 ms*), *flat-top electrolytic power supply produces* plasmas having the same parameters as those produced with the faster-rising field. These results encourage us in our plans to operate the 2XIIB yin-yang coil with the slow-rising power supply in FY 1979.

During the past quarter, we analyzed data obtained from earlier operation of the 2XIIB yin-yang magnet set in which we used the 450-V electrolytic flat-top power supply rather than the 20-kV No. 6 capacitor bank. These data are of interest because we plan to operate 2XIIB in this mode after Bank 6 has been reassigned to energy storage for Tandem Mirror Experiment (TMX) and 2XIIB 20-kV neutral beams. Although we did not expect any difficulties, we were pleased that our analysis of these tests confirmed the insensitivity of plasma parameters to the magnet power supply.

A simplified schematic of the 2XIIB yin-yang magnet system is shown in Fig. 9. Energy storage in Bank 6 for each of the two magnets [illegible] MJ (with 12-kV operation) and [illegible] MJ for the electrolytic bank (with 450-V operation). The electrolytic bank for each coil consists of 48 drawers, each containing 18 1500-μF capacitors. At the present time, each drawer also contains six additional unconnected capacitors that represent a possible future 33% increase in stored energy.

After TMX is operational, we plan to power the 2XIIB yin-yang magnet with the electrolytic bank alone. Then, the magnetic field rise time is 10 ms rather than the present 0.8 ms as with Bank 6 (see time histories in Fig. 10). For the experiments discussed here, we operated Bank 6 at 6 kV (half its nominal level) and the electrolytic bank at 250 V. The solenoidal magnetic field was 0.2 T. As seen in Fig. 10(a), these comparisons were made at nearly the same magnetic field strength. The time the streaming-plasma gun was on is also shown in Fig. 10(a). The gas feed was at 100 Torr, and the apertures were 0.046 in. in diameter.

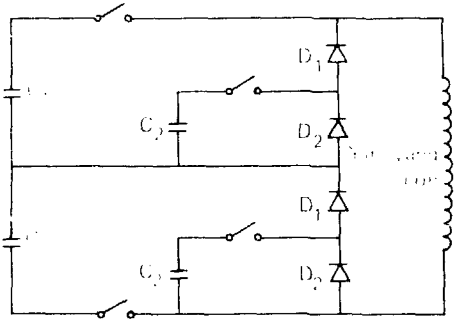

C_1 Bank 6 12 μF at 20 kV

C_2 Electrolytic bank 6.5 F at 450 V

D_1 19 2-kV silicon diodes in series

D_2 2-kV silicon diode

Fig. 9. Power Supply for the yin-yang magnet.

For making these comparisons, we used nearly equal beam currents, 380 A with the electrolytic bank and 340 A with Bank 6 [see Fig. 10(b)]. The microwave density was also nearly the same [Fig. 10(c)], the diamagnetic loop signal, the neutron production rate, and the charge-exchange analysis were also very similar [Figs. 10(d), (e), and (f), respectively]. Thus, we conclude that the plasmas produced by these magnet power supplies are nearly the same.

In the operation described here, the central pulsed magnetic field was 0.23 T with the electrolytic bank at 250 V. At 450 V, we expect 0.42 T. *Utilizing the* remaining capacitors could permit us to reach the present 0.47-T nominal magnetic-field level. Of course, the field would not be constant for 10 ms as in present operation, but would decay with a 25-ms L/R time constant.

Development of a Reliable 40-kV Neutral-Beam Module

R. H. Munger, D. L. Correll, A. B. Molvik, and F. H. Coensgen.

Completed tests of two zero-effort, 40-kV, neutral-beam modules have verified that the design meets *the* TMX *requirements.*

By October, a 40-kV grid set without electrostatic steering of ion beamlets in the direction perpendicular to the wires had operated for more than 1000 shots at 40 kV without signs of damage. To establish some confidence that these results could be repeated, we constructed and tested a second zero offset grid. The latter has been run for 1200 shots above 37 kV and 600 at 40 kV. Thus, we know that we have identified and eliminated design problems causing early failure of previous 40-kV grid sets.

Based on the measured output, neutral-beam modules using the 40-kV grid sets fulfill the TMX 40-kV *beam requirements.* We are continuing our effort to further improve the performance of the 40-kV modules by geometrically focusing the ion beamlets. The grids will be curved in two dimensions to provide both transverse and parallel focal properties.

Emergence of the Problem. Following the successful *40 kV* operation of a 7 × 35 cm three-grid extractor assembly at Lawrence Berkeley Laboratory (LBL), *five similar units were built at* Lawrence Livermore Laboratory (LLL) and installed in the 2XIIB experiment during January 1976. *Performance* of any one of these units never exceeded 34 kV, and typical operating potentials during 2XIIB runs ranged from 20 to 30 kV. To increase injected neutral-beam current into 2XIIB, four of the 40-kV units were replaced with 20-kV units in August 1976. The fifth 40-kV unit was retained on 2XIIB *to* continue development of both the 40-kV modulator and the 40-kV ion accelerating structure. Through minor modifications of the power supply, control circuits, and transmission lines, we obtained fairly routine *operation of the single 40-kV unit at* potentials between 30 and 33.8 kV. These modifications improved reliability of the protective *interrupt* and reduced problems caused by crosstalk with other neutral beams and with the 2XIIB machine.

By January 1977, the operating potential of this unit was limited by failures within the grid structure rather than by power supply problems. Because the problem was independent of the 2XIIB system, development of the 40-kV module was transferred to *the 2X test stand, where module modifications would be made without interrupting 2XIIB operation.*

Failure Mode Identification. Although 40-kV operation was achieved in May 1977, these grids quickly deteriorated, yielding only about 100 shots at 40 kV. The damage pattern was similar to that in modules used in 2XIIB; that is, the damage was *confined to wires in the end regions.* Frequently, we found burned-out arc chamber filaments at the position of the damaged wires. In all cases, the discoloration and warping of grid wires in the end regions was indicative of excessive heat loads on these elements.

Because of the nature and the location of the damage, we suspected that a fraction of the

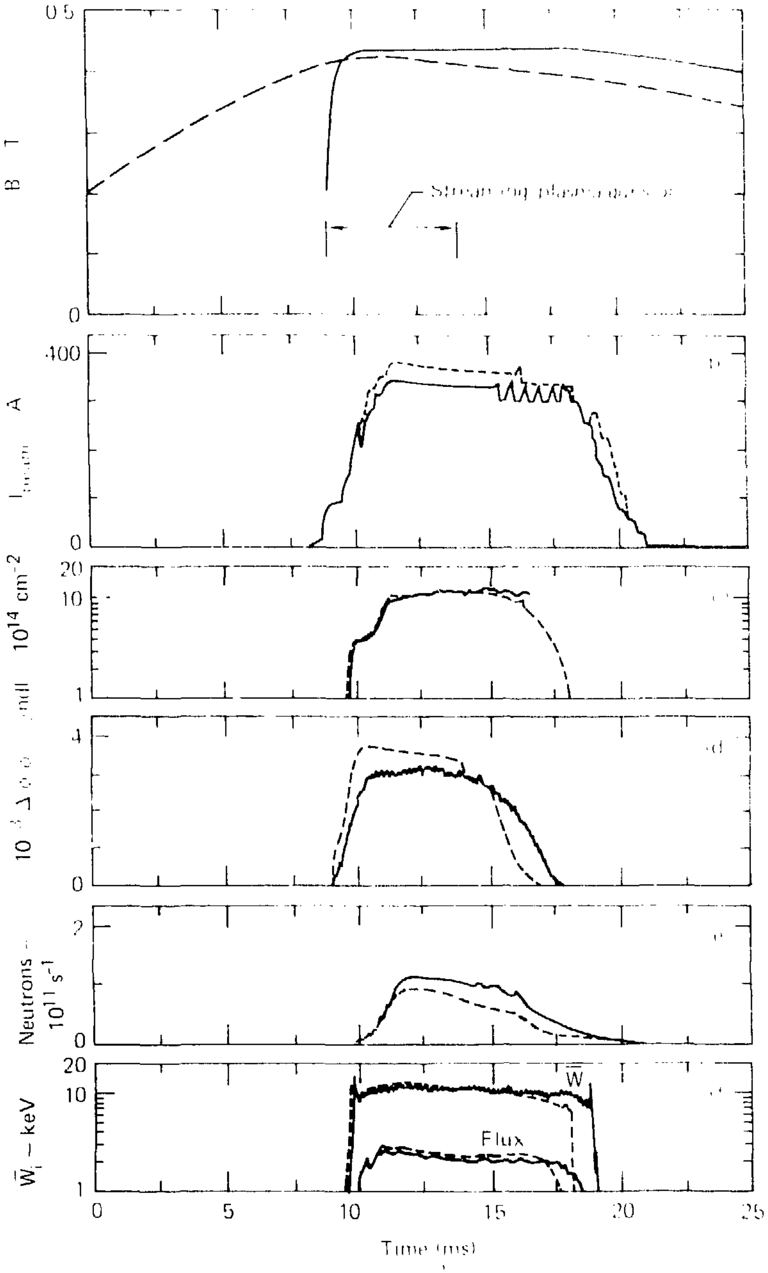

Fig. 10. Comparison of normal operation with Bank 6 (solid curves) with operation with electrolytic flat top bank (dashed curves). (a) magnetic field, (b) neutral-beam current, (c) microwave line density, (d) diamagnetic loop signal, (e) neutron production rate, and (f) charge-exchange flux and mean ion energy.

[illegible] beam intercepted by the suppressor and exit grid wires, thereby producing secondary electrons that were then accelerated back into entrance grid wires (and filament). The problem would be more severe for grid wires because the deflection of the beamlets in these regions is greatest (as large as [illegible]). Beamlet deflection is achieved by offsetting the entrance grid with respect to the second (suppressor) grid. The method of focusing the ion beamlets steers them close to the suppressor and exit grid wires. Figures 11 and 12 show computed beamlet paths without offset and estimated beamlet paths with offset for both the 20- and 40-keV grid sets. Similar analysis showed that grid wires must be placed within unusually close tolerances to avoid excess ion currents to the suppressor and exit grid. We also found that beamlets are less well focused, and consequently ion currents to the suppressor and exit grids are excessive, either if plasma density in the arc chamber is not optimal or if the radius of curvature of the sharp edges of the trapezoidal cross section entrance grid wires is not the minimum achievable.

Solution. To evaluate the effect of grid offset on operating reliability, we built and tested a zero-offset grid set at LBL. This module ran reliably at 40 kV for more than 1000 shots.

The performance characteristics of the zero-offset module represent the equivalent of 50 A of neutral atom current in a 10 × 33-cm area located 3.2 m from the first grid. Because TMX performance was predicted assuming 40 A of neutral atoms in 10 × 33 cm at 3.2 m, the zero-offset module is adequate for TMX.

In November 1977 we constructed and tested a second zero-offset grid set; only 500 shots were required to achieve 40-kV operation. This grid set has been operated for 1,200 shots above 37 kV and 600 at 40 kV. Calorimetry shows that the current into the TMX target area is down 10% from the first zero-offset grid but that it is still 5 A greater than the 40 A assumed necessary for TMX.

Conclusion. Longitudinal focus by grid offset is conceptually simple. However, the method is difficult to use for high current density, large area grid sets operated at high potentials because the required tolerances are difficult to achieve and maintain for long periods of operation.

We have shown that both the reliability and the current required for TMX can be achieved with a grid set using curved wires for focus in one direction, but without either offset between the grids or curvature to steer the beamlets in the direction transverse to the slots of the extractor grids.

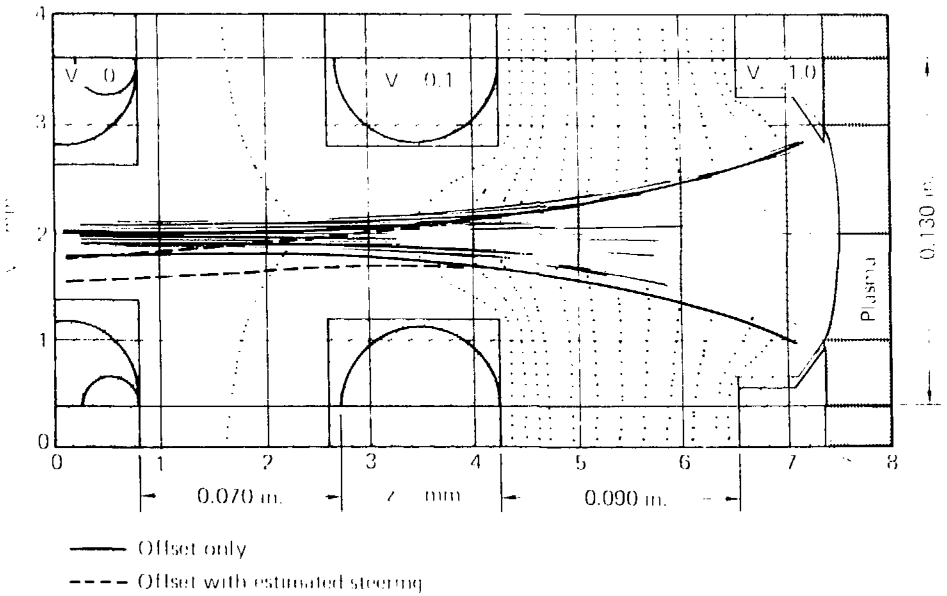

Fig. 11. 20-keV extractor with 0.0031-in. offset of entrance grid.

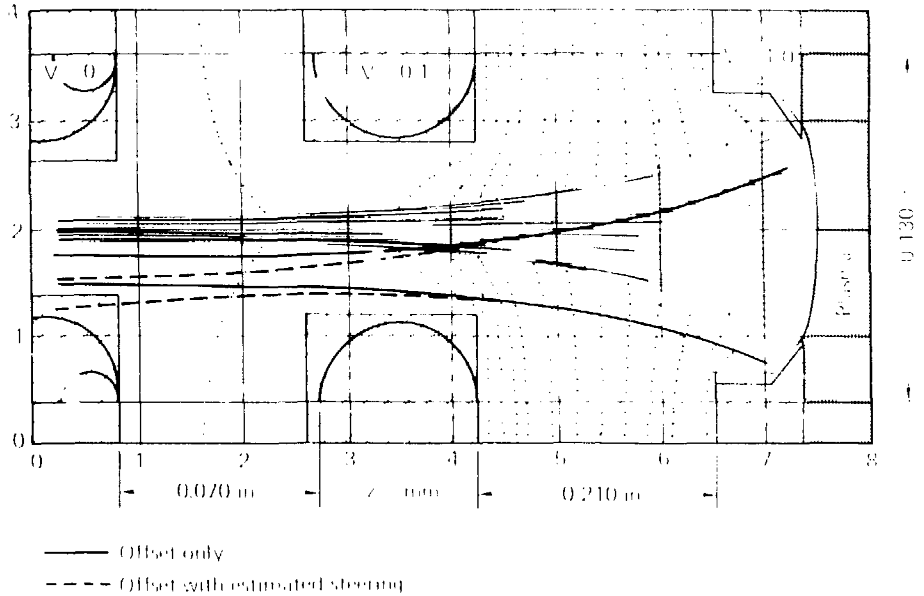

Fig. 12. 40 keV extractor with 0.015 m offset of entrance grid.

Final Operational Status Testing of the 2XIIB Neutral-Beam Computer Control and Monitoring System

G. Pollock

With the completion of a series of tests and demonstrations, we have officially established the fully operational status of the computer control and monitoring system used on the 12 2XIIB neutral beams.

The computer control and monitoring system used on the 12 2XIIB neutral beams has completed a series of tests and demonstrations to officially establish its fully operational status. Although the data collection and data reduction modes of operation had been in regular use for more than a year, active automatic control of the beams had been only by the design engineers and programmers and only in a closely controlled demonstration environment. Although a very successful demonstration of fully automatic injector conditioning of multiple beams was held in March 1977, problems in the manual control system and interface electronics prevented the simultaneous operation of all 12 beams. Subsequent exclusive use of the beams for physics research goals delayed the final testing until November.

The testing proceeded as expected. The first several days were spent finding and correcting the last hardware and software errors. Much of the hardware associated with some beams had not been fully exercised in the past and had a normal amount of wiring errors and component failures.

The objectives of the test sequence were all met and the results may be summarized as follows:

- An automatic conditioning which had been demonstrated in the Spring was shown to work well on all 12 beams simultaneously.
- The conditioning algorithm satisfactorily ran the beams at a fixed level, thereby eliminating what previously was an entirely separate operating mode and resulting in considerable simplification for the operator.
- The simultaneous operation of the 2XIIB magnets did not affect the computer control system. Although some electromagnetic interference effects could be seen on some instrumentation channels, the control system averaged them over the pulse duration and was unaffected.
- The system can be used by physics technicians with minimum training.

[illegible] was the last point above [illegible] the way in which the operator interacted with the computer control system. "Control by exception" has been a developmental goal of the system, and we have endeavored to avoid forcing the physics technician to become a computer operator. The beams are primarily operated from the manual control system, even if the computer is doing the controlling. The computer reads the control settings for sources being operated manually and observes the resulting currents. The control calculations are performed in reverse so that the various parameters and coefficients that mathematically describe beam operation are developed by observing manual operation. To place a beam under computer control, the operator throws one switch. The computer then conditions the beam automatically beginning with the last operating point used by the human operator and operates the beam along the line of best focus as defined by the human operator's control values. The operator may freely switch the beam back and forth between automatic and manual control. Each time manual control is used, the computer system observes the operation and adjusts its internal parameters. The effect is that the operator interacts through a familiar medium, the existing manual controls, and seldom has to approach the computer. We find this interface very easy to use and to learn, and operators accept it readily.

It is difficult to quantitatively assess the quality of the automatic conditioning. The beams on 2XIIB had seen considerable use and were well broken in. For the most part, therefore, they reached their conditioning objective in close to the minimum number of shots possible. For those beams that took longer, it was difficult to find instances where the human operator might have made different (and better) control decisions. The reaction of the conditioning algorithm to stubborn beams was as expected and satisfactory.

In conclusion, the computer control system is operational for automatic control as well as for monitoring. In the future, we hope to see it regularly used in this capacity and, through its archiving of operating data, to learn more about the behavior of neutral beams.

Status of Continuing Developments

Field-Reversal Experiments. *W. C. Turner, C. W. Hartman, J. F. Clauser, and B. W. Stallard.* Field-reversal experiments have been temporarily interrupted by the large-diameter plasma experiment. Interim results are being analyzed. We are documenting experimental results to date for distribution at the Mirror League Workshop.

Two new sources are being investigated; either might approximately double the energy content of the plasma. One is the intense pulsed ion neutral source (IPINS) being developed at LLL; the other is a plasma gun developed by Dah Yu Cheng of the University of Santa Clara.

The Santa Clara plasma gun has a 10-kV electrical supply. We are attempting to inject across the magnetic field and trap the gun plasma in 2XIIB. This gun could provide an amount of energy comparable to the 1-kJ characteristic of high beta 2XIIB plasmas. If successful, arrays of similar guns could be employed on 2XIIB to create a large-volume, high beta plasma for field reversal experiments. There are a number of questions to be answered next quarter about gun efficiency, injection across magnetic fields, and trapping efficiency.

The Zeeman diagnostic dye laser for measuring 2XIIB magnetic fields is now operating and we are ready to test tune-up methods. The detectors are built and ready to install on 2XIIB. The helium-beam parts are being assembled.

Installation of the hydrogen cyanide laser interferometer Faraday rotation diagnostic was completed this quarter. In initial tests, the mirror moved when the yin yang magnet was fired. To enable this diagnostic to work, we shall install a more massive mount for the reflecting mirror.

Electron-Temperature Scaling Experiments. *J. F. Clauser, R. K. Goodman, and G. M. Melin.* Analysis of electron-temperature scaling experiments has continued. For future experiments, we built two seven-segment (6 cm × 8 cm) end-loss calorimeters and installed them in each end of 2XIIB. The electronic readout circuitry is also ready for calibration. To investigate the axial density and electron temperature profiles ahead, within, and behind the gas box, we designed a five-tip Langmuir probe.

Stabilizing Plasma Sources. *W. E. Nexsen, B. G. Logan, D. P. Grubb, and J. E. Osher.* Experiments with our conventional stabilizing plasma guns were described earlier in this report. During this quarter, initial experiments were performed with gas-fed plasma guns. These as well as further results will be described next quarter. We experienced difficulties with [illegible]-in.-diam deuterium-loaded washer guns. Tests of improvements are underway and will also be reported next quarter. Following the encouraging MIT results using an E-beam to stabilize ion-cyclotron frequency fluctuations, we have designed an E-beam gun and power supply suitable for 2XIIB. These modules will be built next quarter and subsequently tested on 2XIIB.

One relatively efficient source of streaming plasma to stabilize the drift-cyclotron loss-cone (DCLC) mode would be a large-area, low-voltage ion source arranged to inject H⁺ ions of energy just over the ambipolar potential in and along field lines. For this purpose, we are developing a new type of test ion source with a 10 cm × 15 cm extractor area. Plasma densities of the needed 10[illegible] cm[illegible] range have been obtained over this area using a 200-A reflex arc discharge from a 18-cm-diam oxide-surface dc cathode and a mesh anode on a 0.1-T axial field. With a stretched molybdenum wire accel-decel low-voltage extraction geometry, we have obtained a total drain current of over 20 A for 10-ms pulses. Beam diagnostics, including an array of Faraday cups and a large calorimeter, indicate that at least 60% of the drain can be available as useful beam. The apparent high gas efficiency of the source results in performance being very sensitive to gas distribution and timing. For a report of preliminary work, see Ref. 3. Further work to optimize the gas distribution and low-voltage extraction geometry would be desirable. However, to speed up tests for possible application, this prototype source is being installed on 2XIIB to address possible other fundamental problems that might result from 2XIIB plasma counterstreaming into the extractor grids.

Measurements of Impurities in 2XIIB. *R. P. Drake.* An extreme ultraviolet monochromator from Johns Hopkins University was installed on 2XIIB and initial measurements have been taken. The instrument was installed and aligned, a spatial scan was used to locate the machine center. We have identified the emission lines of oxygen, nitrogen, carbon, and titanium.

Reaction Ion Analyzer. [illegible] performance of the [illegible] ing. We have detected [illegible] MeV [illegible] MeV tritons under the [illegible]. The present apparatus was designed [illegible]. From preliminary measurements there now exists the probability that the 0.8-MeV H[illegible] fusion reaction product can also be observed by using a [illegible] before the detector that is thin enough to allow the He ions through to be counted by the detector yet thick enough to attenuate adequately the background signal that earlier saturated the detector electronics system. Other improvements obtained as the detector position is optimized include higher counting rates for the H and T ions.

Engineering Developments. *G. G. [illegible]* After successful operation of the four streaming-plasma gun power supplies using 5-ms pulse-forming networks (PFNs) to supply the 5000 A per gun, we have fabricated and installed eight additional 5-ms PFNs and four additional charging and firing boards. With the above additions we can accommodate not only a combination of up to [illegible] streaming-plasma guns (4 each at 10 ms or at 4 each at 5 ms) but also other combinations that [illegible] in.-diam guns.

Following a brief period of shutdown in late November, our attempts at operating Bank 6 resulted in failure of 20% of the diodes in the flat-topper unit because of a short to ground near the east yin-yang compression magnet. To prevent similar future failures, we have installed and tested a Bank 6 ground-fault detector and a prefire chassis. In addition, to ensure more consistent operation of the Bank 6 series ignitrons, we are installing a 24-channel detector that will provide a routine method of detecting and remedying bank misfires.

Tandem Mirror Experiment

The Tandem Mirror Experiment (TMX)[4] will test a new principle for improved plasma confinement in mirror systems. The basic idea is to reduce the plasma loss rate by electrostatically plugging the ends of a solenoidal central confinement region using the high positive ambipolar potential generated in minimum-B end plugs. Each end plug will be driven by the injection of neutral beams from 12 source modules, in a manner similar to that used in the 2XIIB experiment.

The TMX has three fundamental objectives.

- To demonstrate the establishment and maintenance of a potential well between two mirror plasmas,
- To develop a scalable magnetic geometry, while keeping macroscopic stability at high beta, and
- To investigate the microstability of the plug-solenoid combination in order to maximize the plug-density injection-power ratio.

Possible secondary objectives that have important reactor implications include the study of enhanced radial transport in the solenoidal cell and the accumulation of thermalized alpha particles in the central plasma.

The key physics parameters projected for the TMX experiment are listed in Table 2.

Table 2. Key physics parameters for the TMX experiment.

Parameter	Value
Electron	
Temperature, T_e	0.20 keV
Confining potential, ϕ_e	1.1 keV
Plug	
Density (assumed uniform over V_p), n_p	5×10^{13} cm^{-3}
Average energy, E_p	26 keV
Radius of plasma half-maximum, r_p	7 cm
Central magnetic field, B_p	1.0 T
Confinement product, $(n\tau)_p$	3×10^{11} cm$^{-3}\cdot$s
Central cell	
Density (assumed uniform over V_c), n_c	1.2×10^{13} cm^{-3}
Ion temperature, T_c	0.080 keV
Confining ion potential, ϕ_c	0.29 keV
Length, L_c	5.5 m
Radius, r_c	31 cm
Magnetic field, B_c	0.05 T
Confinement product, $(n\tau)_c$	3.1×10^{11} cm$^{-3}\cdot$s

Magnetic Field Design

Optimization of the Solenoidal Section. *B. G. Logan, D. E. Baldwin, J. H. Foote, A. K. Chargin, R. E. Hinkle, R. O. Hussung, and C. C. Damm.*

An improved design for the transition coil between the solenoidal center cell and the end plugs provides for a field-line configuration that meets the physics objectives of the TMX.

Continuing field calculations for the TMX magnet have led to an improved transition coil design (Fig. 13). In this improved configuration, the quadrupole Ioffe-bar windings described in our conceptual design[1] are replaced by a pair of C-shaped coils in each transition region. Each C-coil pair is augmented by an octupole winding to smooth the ripple structure.

Optimization of the currents in this improved magnet set leads to a field-line configuration with a central solenoidal region that is uniform in field intensity to within 10% over a 2-m length.[2] This field design has sufficient flexibility to meet all three physics objectives of the TMX experiment.[1]

Plug Orientation and Single-Particle Adiabaticity. *B. G. Logan, D. E. Baldwin, and J. H. Foote.*

By orienting the TMX plugs at 90° with respect to one another, we obtain almost circular drift surfaces for the ions trapped in the solenoid and reduce their nonadiabatic scatter.

The multiple-element coil set for the TMX allows considerable flexibility in the details of the magnetic-field shape. Our effort to make the solenoidal portion as uniform as possible by proper choice of current elements[2] is motivated by our desire to clearly isolate the bad-curvature portions of the solenoid-plug transition regions. Because of the degree to which these regions can be isolated, the plugs can be joined to the solenoid with the plugs oriented at either 0° or 90° with respect to one another. We summarize here the considerations giving rise to our choice of a 90° orientation. (Note: the 0° orientation shown in Fig. 13 is from an earlier layout.) In brief, we find drift confinement in the solenoid to be the determining factor.

The choice of the 90° orientation preserves the $z \to -z$ and $\theta \to 90° - \theta$ symmetry familiar in minimum-B mirror machines. For this reason, one would expect this orientation to have the weaker line-averaged, bad-curvature drive for instability in the transition region. Although we find this to be the case, the differences are not significant, given the dominance of the good curvature of the plugs when pressure-weighted. Because ballooning modes are localized, β-limits due to these modes are even less sensitively dependent upon orientation.

Because of the relationship between the solenoid and the plugs — with the plugs stopping a portion of the magnetic loss cone and the solenoid supplying stabilizing low-energy ions to the plugs — both must occupy the same flux-tubes; i.e., they have similar drift-surfaces. The drift surfaces in the plugs are nearly circular, and the magnetic design has recircularized this flux-tube in the solenoid, independent of the 0° or 90° orientation of the plugs.

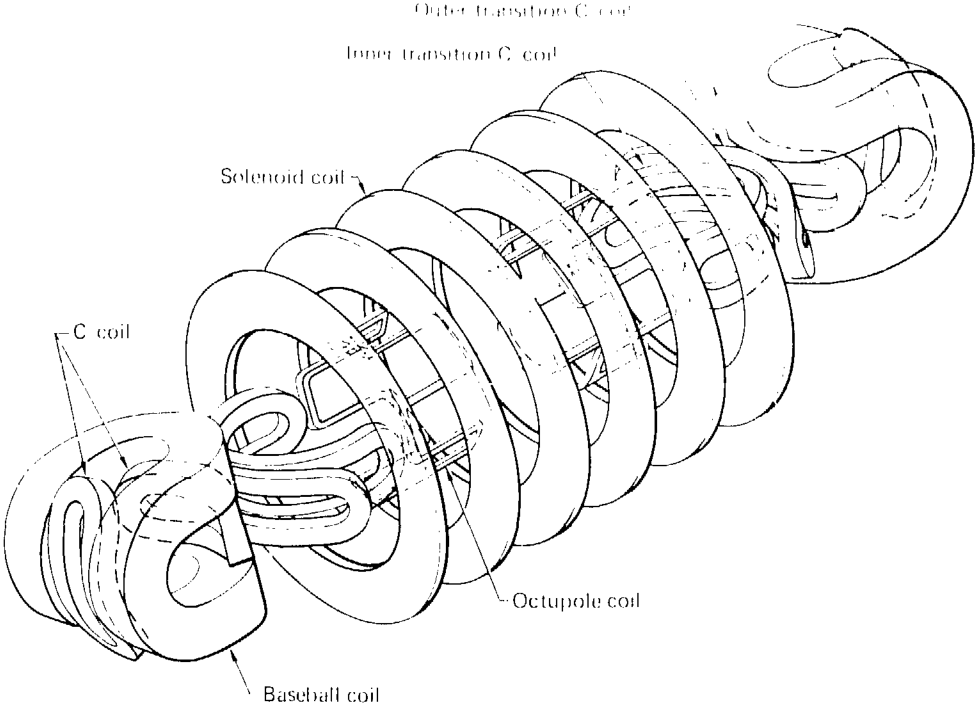

Fig. 13. TMX magnet set.

However, with the plugs in the 0° orientation, we find that the drift surfaces of ions trapped in the solenoid are ellipses of about 3:2 ellipticity. For some initial conditions, these surfaces can actually encounter the solenoidal magnets. With the plugs in the 90° orientation, the drift surfaces are almost circular, being only slightly "squared-off." Examples of the drift surfaces in the two orientations are shown in Fig. 14.

Finally, we have examined the question of adiabaticity of ions in the nominal field. (See App. A of Ref. 4 for a detailed discussion of the adiabaticity of ions in the plugs.) Because solenoidal ions having energies less than the plug-to-solenoid potential drop are electrostatically confined, adiabaticity is [illegible] consideration only for ions exceeding this energy [illegible] particular, in the magnetic optimization wherein the solenoid is made as uniform as possible [illegible] and the transition correspondingly short [illegible] magnetically confined 300-eV ions do experience a small-angle scatter on each reflection from the transition. However, the resulting 90° scattering time is longer than that due to Coulomb collisions, so that adiabaticity is not limiting the lifetime of the ions. Rounding the transitions by altering the currents in the solenoidal coils further reduces the scattering due to nonadiabatic effects. The 90° scattering times for various current settings, normalized to that resulting from classical scattering, are shown in Fig. 15.

Results from Calculations of Drift Surfaces and Detailed Particle Orbits in TMX. *J. H. Foote*

To help ensure that the complex magnetic-field configuration planned for TMX is compatible with the physics objectives of the experiment, we have carried out a series of calculations of drift surfaces and of detailed particle orbits.

A drift surface is the three-dimensional extent over which the guiding center of a particle confined in a magnetic field moves as the particle is reflected back and forth between mirror regions and as it precesses

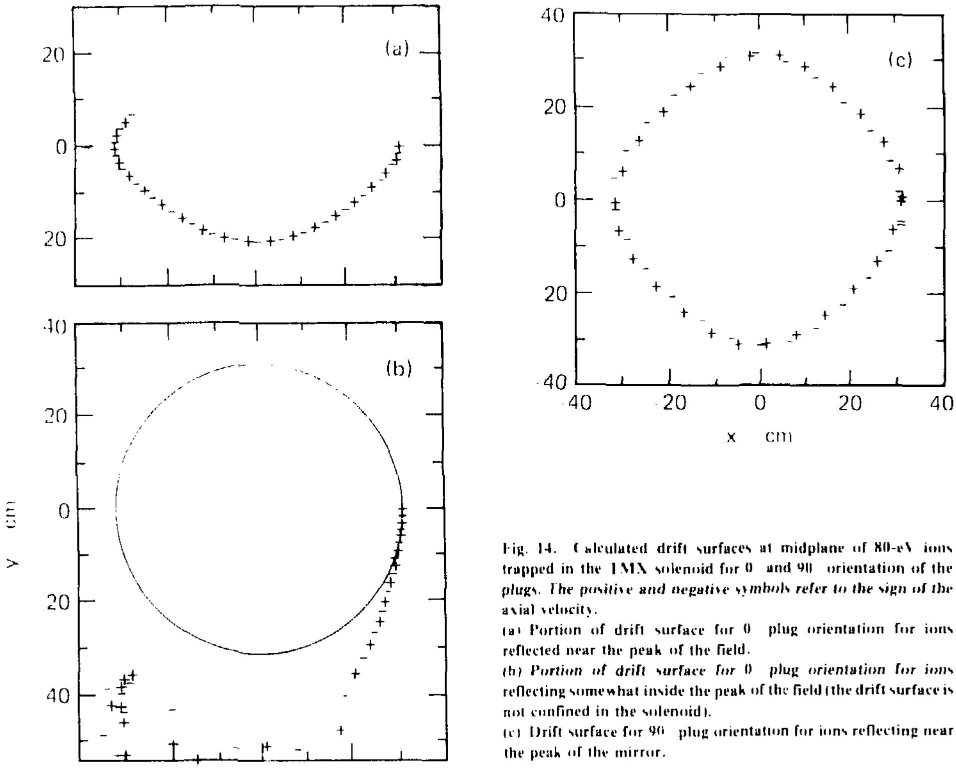

Fig. 14. Calculated drift surfaces at midplane of 80-eV ions trapped in the TMX solenoid for 0° and 90° orientation of the plugs. *The positive and negative symbols refer to the sign of the axial velocity.*

(a) Portion of drift surface for 0° plug orientation for ions reflected near the peak of the field.

(b) Portion of drift surface for 0° plug orientation for ions reflecting somewhat inside the peak of the field (the drift surface is not confined in the solenoid).

(c) Drift surface for 90° plug orientation for ions reflecting near the peak of the mirror.

around the magnetic axis. The characteristics of the drift surface not only depend on the magnetic-field configuration but also can vary with the radial position of the particle as it passes through the midplane and the value of its pitch angle there. The conclusions from our calculations of drift surfaces of particles in the solenoidal magnetic-field section of TMX are summarized as follows:

- The drift surfaces of particles confined in the solenoidal section appear to be closed and well-behaved. The quadrupole end-plug regions tend to cause the surfaces to have a squarish appearance [see Fig. 14(c)] and thus to deviate somewhat from an otherwise circular character.
- The drift-surface results were the determining factor in deciding to orient the end-plug magnetic-field regions at 90° with respect to each other rather than to align them (see preceding article).
- An ambient, few-Gauss magnetic field transverse to the solenoidal field, as might arise from magnetic materials surrounding the experiment, does not destroy the calculated drift surfaces. They become distorted but still nest and close on themselves.[5]

In calculating a detailed particle orbit, one follows the particle through its gyrations around magnetic-field lines as well as through the reflections and drifts of the drift-surface calculations. If the orbit gyroradius is large, this method provides a more accurate representation of the particle motion. (But, because of the more detailed information obtained, it requires considerably more computer time.) Also, nonadiabatic behavior can be detected with the detailed calculations but not with the drift-surface gyroperiod-averaging calculations. Nonadiabatic behavior is caused by too rapid a change in magnetic-field magnitude experienced by a particle over a gyroperiod, and is evidenced by jumps in the magnitude of the magnetic moment (W B). If these jumps are large and frequent enough, they can cause particles to be lost from the confining-magnetic-field region in a time comparable to or faster than other

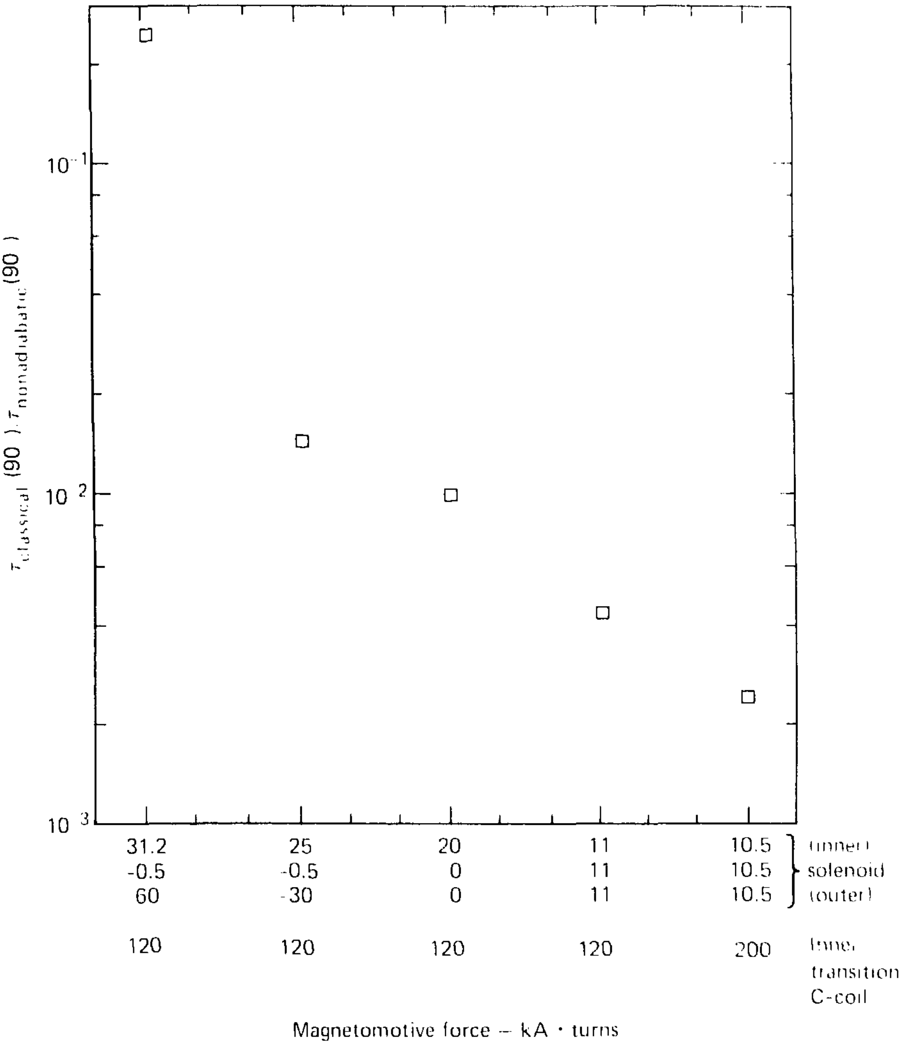

Fig. 15. Ion lifetimes for nonadiabatic scattering normalized to that resulting from classical scattering for various solenoidal-loop and inner transition C-coil current values.

particle loss times. This is to be avoided. Summarizing the results from the calculations of particle orbits in the TMX solenoidal section, we have:

- The magnetic-field configuration must be designed so as to avoid sharp dips and other abrupt spatial variations in the magnitude of the magnetic field. Otherwise, large magnetic-moment jumps can occur.
- For the coil configuration being constructed, nonadiabatic behavior does not appear to be a serious problem. We have investigated the orbits of D^+ ions in a 0.05-T solenoidal magnetic field, with energies up to 300 eV, and ions in a 0.2-T solenoidal magnetic field, up to 20 keV. Nonadiabatic effects are found, but apparently a proper choice of currents in the various coils can keep these losses under control for the ranges of parameters in the experiments now envisioned for TMX.

[illegible]

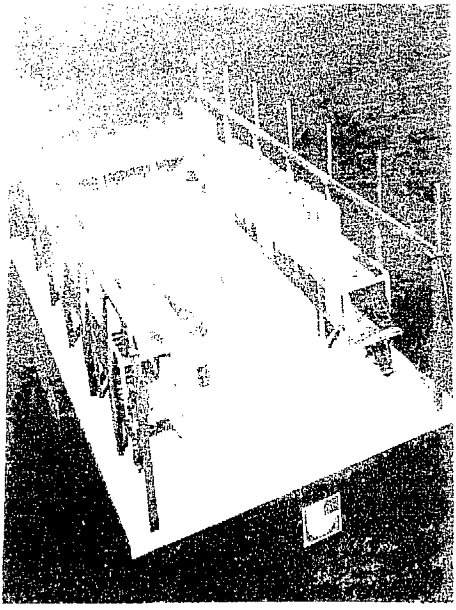

Fig. 16. A model of the completed TMX. The vacuum vessel is located within a neutron shield and is surrounded on three sides by [illegible] power supplies.

Vacuum System [illegible]

[illegible]

Injector System. [illegible]

[illegible] of the first 10-kV prototype [illegible] nearing completion. However, [illegible]

Ma[illegible]	[illegible]	[illegible]
[illegible] 1	[illegible]	[illegible]
[illegible] 2	[illegible]	[illegible]
[illegible] 3	[illegible]	[illegible]
[illegible] 4	[illegible]	[illegible]
90° [illegible]	[illegible]	[illegible]
90° trans 2	NA	[illegible]
180° trans 1	[illegible]	[illegible]
180° trans 2	[illegible]	[illegible]
Baseball 1	[illegible]	[illegible]
Baseball 2	in fab	[illegible]
Octupole 1	in fab	[illegible]
Octupole 2	in fab	[illegible]

[illegible]

Facilities [illegible] MFX [illegible] is nearing completion [illegible].

A contract for [illegible] structure has been placed with [illegible] and work has begun. The design for the [illegible] in the pit and [illegible] is complete and the [illegible] materials are [illegible] for grounding the power supplies [illegible] and handling [illegible] is being prepared.

Design is continuing [illegible] ways to [illegible] power to the [illegible]. [illegible] the following:

- High voltage power [illegible] between [illegible] power supplies and the [illegible]
- Primary power to the [illegible] power supplies
- Control and [illegible]
- General utility power and [illegible]
- Power to the pit area

Controls [illegible]

Diagnostics [illegible]

Mirror Fusion Test Facility

As a result of major experimental successes in the LLL mirror program on startup and stabilization of plasmas in minimum-B magnetic geometry, a Mirror Fusion Test Facility (MFTF) was proposed. The MFTF will be used to bridge the gap between present day small mirror experiments and future fusion reactor activity based on magnetic mirrors. The MFTF will investigate advanced engineering problems such as those associated with superconducting magnets, neutral-beam injectors, plasma-wall interactions, disposal of neutral particles and ions escaping from the plasma chamber, and high-speed vacuum pumping techniques.

Approval for the project has been given and both operating and line item funding has been authorized for the MFTF. Construction of the facility began on October 1, 1977, with completion scheduled for July 1981. The project is proceeding on schedule.

Technical Support

The objectives of the MFTF Technical Support Group are

- To monitor the MFTF design for consistency with the physics requirements.
- To provide research leading to improved performance of MFTF auxiliary components such as startup neutral-beam sources, plasma streaming sources, vacuum accessories, etc.
- To analyze the physics of MFTF to ensure that the completed facility will achieve the stated scientific goals.
- To keep the MFTF system requirements consistent with the current understanding of mirror fusion physics.

Streaming-Plasma Requirements

We have analyzed the streaming-plasma requirements for both the target plasma and the stabilizing plasma in MFTF. The target plasma will be generated with plasma guns as in 2XIIB. However, in MFTF these guns must be located far from the mirror throat in order to reduce the power density incident on them. If they are located on the end domes of MFTF, the plasma must climb a magnetic hill with a mirror ratio of 133. Results from Baseball II-T and 2XIIB indicate that these guns would be very inefficient when operated in this mode. We have made an initial design of a pulsed magnet that will increase the magnetic field at the gun during the buildup phase, thereby increasing the efficiency of the guns as well as providing a more uniform target plasma at the midplane. The stabilizing plasma for MFTF will be generated with a gas box. Scaling from the 2XIIB results indicates that a gas input rate of 1500 Torr-litre/s will be required. This gas must be pumped by the cryopanels in MFTF.

Target Plasma Production. *G. D. Porter.* Our experience with 2XIIB and Baseball II-T (BBII-T) has shown that streaming-plasma guns do not perform satisfactorily when the plasma must be injected over a large magnetic hill (i.e., where the mirror ratio is large). If located near the end domes of MFTF, the guns would have to overcome a mirror ratio of 133. The heat load from the escaping plasma precludes one alternate possibility of inserting the guns near the mirror throat. A second approach would be to increase the field near the gun during the plasma-buildup stage by installing a small, pulsed magnet. It is conceivable that this coil could be used as the inductor in the power supply and hence not represent any additional expense. During the quarter, we completed some simple early calculations of the field requirements and potential coil shapes.

The field at the 9-m spherical surface on the end of the MFTF tank is roughly uniform over the surface. Assuming the plasma flows adiabatically along flux lines, the area on the end tank A_w, which must be irradiated with plasma to cover a midplane plasma area A_0, is given by

$$A_w = \frac{B_0 A_0}{B_w} . \tag{1}$$

where B_0 and B_w are the magnetic fields at the midplane and wall, respectively. This area must be covered by N streaming-plasma guns. If the field generated by the coil surrounding the streaming-plasma gun is given by B_g, the radius of the streaming-plasma gun is given by

$$R_g = \left[\frac{B_0 \; R_p{}^2}{N\,(B_g + B_w)}\right]^{1/2} . \tag{2}$$

where R_p is the midplane plasma radius.

Consider the coil geometry shown in Fig. 18.

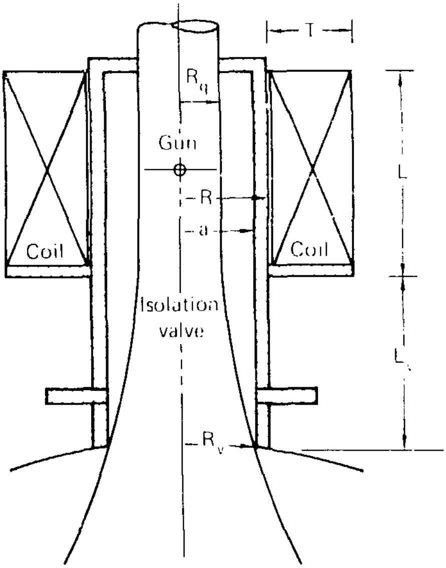

Fig. 18. A magnetic-field-enhanced, target-plasma gun. In this design, the coil is located outside the vacuum and the gun need not be inserted through the isolation valve.

The magnetic field on the axis of this coil is given by

$$B_z(0,z) = \frac{\mu_0 J R}{2} \left\{ (\zeta - \frac{\lambda}{2}) \ln \frac{(1+\tau) + \left[(1+\tau)^2 + (\zeta - \frac{\lambda}{2})^2\right]^{1/2}}{1 + \left[1 + (\zeta - \frac{\lambda}{2})^2\right]^{1/2}} - (\zeta + \frac{\lambda}{2}) \ln \frac{(1+\tau) + \left[(1+\tau)^2 + (\zeta + \frac{\lambda}{2})^2\right]^{1/2}}{1 + \left[1 + (\zeta + \frac{\lambda}{2})^2\right]^{1/2}} \right\} , \quad (3)$$

where J = current density (A/m²), $\zeta = z/R$, $\lambda = L/R$, and $\tau = T/R$.
The radius of the flux lines that intercept the gun is then

$$\frac{R(z)}{R_g} \approx \left[\frac{B_z(0,0) + B_w}{B_z(0,z) + B_w}\right]^{1/2} \quad (4)$$

Using Eq. 2, Eq. (4) reduces to

$$R(z) = \left[\frac{B_0 R_p^2}{N (B_z(0,z) + B_w)}\right]^{1/2} \quad (5)$$

Eq. (5) with

$$R(L_v) \le R_v$$

determines a minimum current density that allows all the flux lines from the streaming-plasma gun to enter the vacuum vessel without passing through the walls of the valve. Figure 19 shows a typical plot of the flux line vs distance from the center of the coil. We have assumed that R_v = 8.89 cm (7-in. valve) and L_v = 20 cm.

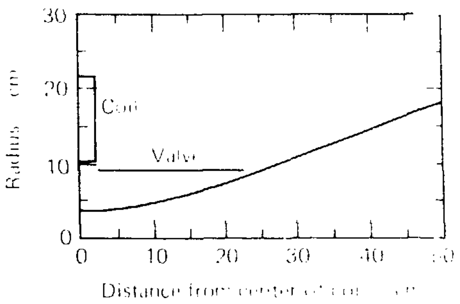

Fig. 19. Typical flux line for the field-enhanced target-plasma gun shown in Fig. 18. The MFTF fringe field is 0.03 T, the self field of the coil is 2.5 T; the plasma radius is 40 cm, and there are 100 streaming-plasma guns.

The temperature rise in the coil can be estimated while assuming no cooling. The power density is then $J^2\rho$, where ρ is the electrical resistivity. The temperature rise is approximately

$$\Delta T = \frac{J^2 \rho \tau}{x^2 \rho_M C_p} , \quad (6)$$

where ρ_M is the density of the conductor, τ is the pulse length, and x is the packing fraction of the conductor. We assume here that x = 0.75 and τ = 5 × 10[illegible] s.

Figure 20 is a summary graph of the temperature rise vs mass for various coil geometries. It is clear that longer coils tend to be more massive (and hence more expensive) for a given temperature rise ΔT. If we arbitrarily specify that an acceptable temperature rise is 0.5 K (this allows some room for longer pulse lengths), a reasonable coil shape is R = 10 cm, L = 5 cm, T = 11.5 cm. These are the dimensions of the coil used in Fig. 19. Note that the field at the gun is 2.5 T. The effective mirror ratio for the streaming plasma is thus only 1.6, a value comparable to that

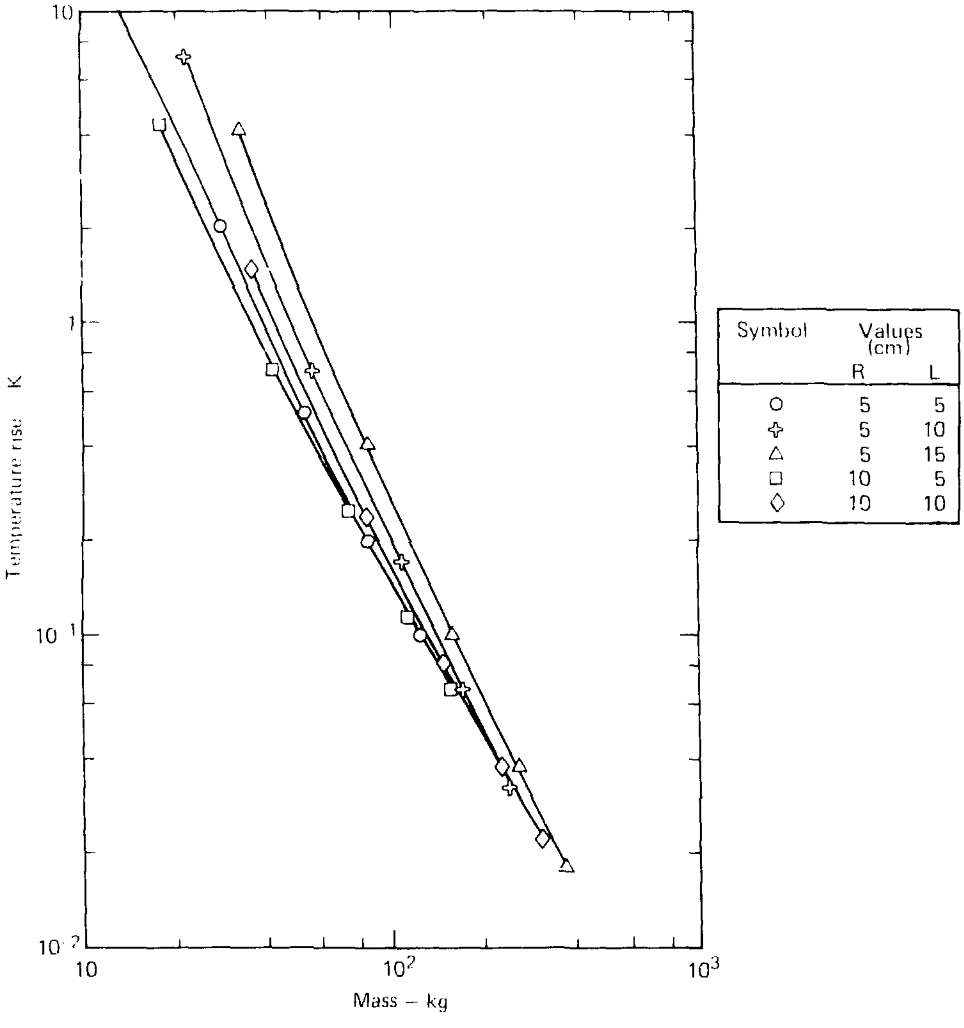

Fig. 20. The temperature rise in the field-enhancing coil as a function of the mass of the coil.

used most successfully in BBII-T. The inductance of this coil is approximately

$$L(\mu H) = 0.69\,N^2 .$$

where N is the number of turns (see Ref. 9, p. 110). Typically, the power supplies for the streaming-plasma guns produce about 2.5 kA; therefore, 10kA cm^{-1} implies 4 turns cm^{-1} or 230 turns total. Hence, the total inductance is about 36.5 mH. This is significantly higher than the inductance (1.2 mH) used in the power supply for the BBII-T streaming-plasma guns. Clearly, making this coil compatible with the inductor for the power supply requires further study.

One problem inherent to the coil geometry shown in Fig. 18 is the requirement that the field must penetrate the vacuum wall. If we treat this wall as an infinite, single-turn solenoid with resistivity ρ and thickness t, the L/R soak-through time is

$$\tau_s = \frac{\pi a^2 \mu_0 t}{\rho 2\pi a} = \frac{\mu_0 a t}{2\rho} . \qquad (7)$$

The resistivity of 304 stainless steel is 7.2×10 Ω-m, hence the soak-through time is

$$\tau_s \approx 0.87 a t .$$

From Fig. 19, it is clear that a = 0.05 m is possible within the coil, implying that a thickness t = 2.3 mm will have a soak-through time of 100 μs. This seems acceptable. Finite length effects will reduce this time further.

The existence of this conducting wall will put a restriction on the rise time of the current. If this rise time is too fast, the vacuum wall will exclude the flux from the interior, creating a pressure between the coil and the vacuum wall. To estimate this effect, we assume that the wall and coil can be treated as infinite solenoids and that the wall is a perfect conductor. Then, the field between the vacuum wall and the coil is given by

$$B = \frac{R^2 B_g(0,0)}{R^2 - a^2} ,$$

where $B_g(0,0)$ is the desired field at the gun. The pressure is then

$$P = \frac{B^2}{2\mu_0} = \frac{B_g^2(0,0)}{2\mu_0}\left(\frac{R^2}{R^2 - a^2}\right)^2 . \qquad (8)$$

Using the geometry in Fig. 19, we can calculate the pressure:

$$P = \frac{(2.5)^2}{2\mu_0}\left(\frac{(0.1)^2}{(0.1)^2 - (0.05)^2}\right)$$

$$= 4.4 \times 10^6 \text{ Pa (640 psi)} .$$

Clearly, this pressure is not acceptable; therefore, we must require that the rise time of the power supply be about equal (or greater than) the soak-through time of the vacuum wall.

The presence of this pulsed field will require other modifications of the present titanium washer-gun design. For example, the copper washers that are used to control the field gradients must be split to allow the field to penetrate. Prudence then suggests that we build a carefully designed gun system magnet, gun module, and power supply and test it thoroughly.

Stabilizing-Plasma Production. A. H. *Molvik*. To determine the gas load imposed on the MFTF pumping system by the gas-box stabilization, we start with a calculation of the required stabilizing current. The mirror-loss current density and therefore the required stabilizing-stream density are given by

$$J_0 = 1.3 \times 10^{-16} \frac{0.53 - 0.28\beta}{[R_{vac}(1-\beta)^{1/2}] - 1} \cdot \frac{n(\text{cm}^{-3})\, T_e^{3/2}(\text{eV})}{E_i(\text{keV})}$$

Note that this is the current density required on each end of the machine. We assume that the MFTF plasma has a flat profile and that it therefore requires stabilization only in the boundary (assumed to be 4 Larmor radii thick). The plasma parameters in this region are $T_e = 200$ eV, $n = 5 \times 10^{13}$ cm^{-3}, $E_i = 25$ keV, and $\beta = 0.12$. The total streaming-plasma current required is then

$$I_0 = 2\pi[(34)^2 - (28)^2] \cdot \frac{0.53 - (0.28)(0.12)}{[2(1-0.12)^{1/2}] - 1} \cdot 1.3 \times 10^{-16} \cdot \frac{5 \times 10^{13}(200)^{3/2}}{25}$$

or $I_0 \approx 753$ A.

Results of experiments on 2XIIB indicate that the gas box is approximately 10% efficient, i.e., a gas input rate of 650 A is required to produce a stabilizing-plasma stream of 64 A. Assuming the same efficiency for MFTF, we find the gas input rate must be about 7500 A or 150 Torr · litre/s.

Neutral-gas requirements

We have assessed the allowable gas densities in the MFTF beam lines and end region. We find that the allowable gas line density in the beam line is set primarily by engineering and economic considerations if the resulting beam loss is 10% or less (neutral-gas line density $n_0 L \lesssim 6 \times 10^{14}$ cm^{-2}) because the loss of this much beam has only minor impact on the physics of the experiment. Buildup-code calculations continue to indicate that the neutral-gas density in the plasma chamber must be less than 10^{11} cm^{-3}. Neutral gas in the region outside

the mirror throat will be ionized and heated by plasma losses from the mirror. We find that the neutral-gas line density in this region must be less than 6×10^{13} cm^{-2} to prevent significant power drain. These requirements define the cryopanel area required to pump the total gas load of 720 Torr-litre/s from the sustaining neutral-beam sources and 1500 Torr-litre/s from the gas box.

Beam line requirements. [illegible] *Metcalf*. Neutral [illegible] by injection on cold gas at rate

$$I = I_0 [1 - \exp(-\sigma_{ion} nL)]$$

where n is the neutral gas density in a tank of length L along the beam. The ionization cross section for ionization of a neutral 80-keV D beam by D$_2$ gas is [illegible] 1.8×10^{-16} cm^2 per molecule. A line density of $nL = 6 \times 10^{14}$ cm^{-2} will ionize 10% of the beam.

The allowable gas line density is set primarily by engineering and economic considerations since the loss of 10% of the beam has only a minor impact on the physics of the experiment. The major engineering considerations are:

- What surface does the ionized beam hit?
- How do we handle the energy deposited by the ionized beam?
- What can be done to reduce the gas line density if the other considerations prove troublesome?

There are at least two economic considerations:

- To maximize the neutral beam current per dollar delivered to the plasma. (Do pumps increase the beam current to the plasma more than the same investment in power supplies?)
- To stay within the budget.

End-Region Requirements. *G. D. Porter*. Ionization of gas in the end regions of MFTF produces a power drain that must be made up by neutral-beam power. To estimate this effect, we determine the ionization rate over the whole fan. This ionization produces a power drain by three routes. The ionization requires an average of 33 eV, the resulting electrons are heated to a temperature of T$_e$, and the ions are heated to (T$_i$). The resulting power drain is then given by

$$P_{loss} = 2e \int_0^L n_{loss}(s) A(s) n_0 (\sigma v)_{ion} ds (33 + T_e + T_i) ,$$

where L is the distance from the midplane to the end of the vessel. The product of the unconfined density and the flux tube area [$n_{loss}(s)A(s)$] is independent of axial position. Hence

$$P_I = 2e [33 + T_e + T_i] n_L (0) A(0) n_0 (\sigma v)_{ion} L .$$

The unconfined density at the midplane can be estimated by assuming that it is equal to $\Delta n(0)$, where Δ is the ratio of warm to hot plasma required for stability against the drift cyclotron loss cone (DCLC) mode. In the boundary of MFTF, $\Delta = 10$ [illegible]; this represents the worst case estimate. Assuming that the neutral gas penetrates the fan, i.e., that the power loss is over the whole plasma cross section, we find

$$P_I = 2e [33 + T_e + T_i] \pi \Delta R_p^2 (\sigma v)_{ion} n_0 n L .$$

We require $P_I \le P_{in}$. Hence

$$n_0 L \le \frac{P_{in}}{e(33 + T_e + T_i) n R_p^2 (\sigma v)_{ion}} .$$

Let $(T_i)_{cell} = T_e = 10^3$ eV

$\Delta = 10$ [illegible]

$n = 10^{14}$ cm^{-3}

$R_p = 33$ cm

$(\sigma v)_{ion} =$ [illegible] $\times 10^{-8}$ cm^3/s and

$P_{in} = 1 \times 10$ [illegible] W

Then

$$n_0 L \le 3.6 \times 10^{14} \text{ cm}^{-2} \qquad (9)$$

Since we have made only worst case assumptions, we consider this to be a rather conservative estimate of the tolerable limits. This estimate, however, ignores the gas breakdown phenomena postulated by Fowler.[13] That limit is given by

$$n_0 = \frac{1}{(\sigma v)_{ion} (\tau_{ii})} ,$$

where τ_{ii} is the transit time of the ions created by ionization of the background gas. If these ions have energy T$_i$,

$$n_0 = \frac{(T_i)^{1/2}}{10^{6} (\sigma v)_{ion} L} .$$

or, for the same assumptions as before,

$$n_0 L = 6 \times 10^{13}\ \mathrm{cm} \qquad (10)$$

Thus, these limits are nearly the same and indicate that the maximum tolerable gas density for the 15-m long vacuum vessel is given by

$$n_0 = \frac{4 \times 10^{13}}{400} = 1 \times 10^{11}\ \mathrm{m}^{-3} \qquad (11)$$

Neutron Flux in the MFTF Vault Area. *G. D. Porter*

Our early estimates of the neutron flux in the vault area surrounding the MFTF vessel indicate that the *neutron flux will be high enough to produce damage* in semiconductor devices located in the vault.

We have estimated the neutron flux in the vault assuming a point source at the center of the plasma. The source strength depends on operating conditions of the plasma. If we operate at B = 2 T, β = 0.5, T = 50 keV, and R = 30 cm, the source strength is 5 × 10 n/s. The neutron flux at distance R from the center is then

$$\phi = \frac{5 \times 10^{16}\tau}{4\pi R^2} \qquad (12)$$

where τ is the pulse length. This flux is plotted in Fig. 21 as a function of R with τ = 0.5. The neutron flux at the farthest wall is about 3 × 10 n/cm² pulse.

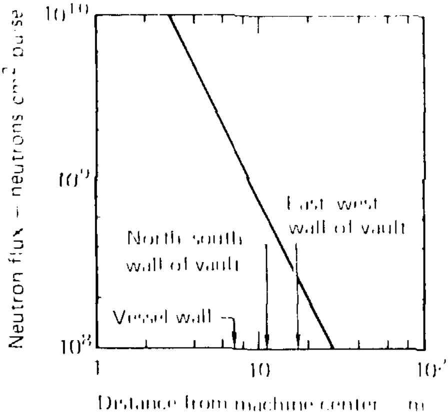

Fig. 21. The estimated neutron flux as a function of the distance from the center of MFTF. We assume that the neutron source is a point source with a strength of 10¹⁶ neutrons.

According to [illegible] R [illegible] operation [illegible] about 5 × 10 [illegible]. The damage [illegible] displacement defects [illegible] accumulative and relatively independent of neutron energy (above 100 keV). [illegible] neutron damage effect in SCR [illegible] most [illegible] *that* [illegible] *would* [illegible] transistors after only a few hundred shots.

Local shielding of sensitive components may reduce the neutron flux to an acceptable level. However, the thickness of the required shielding may be fairly large. For example, 10 cm of polyethylene (CH₂) would reduce the neutron flux by about an order of magnitude. It may therefore be *more reasonable to* [illegible] *and* place the majority of the sensitive devices outside the vault wall.

We have started a detailed Monte Carlo calculation to determine the neutron and gamma fluxes more precisely. This will account for neutron buildup by the magnet [illegible] and vault reflection off the vault walls. [illegible] we are investigating the damage thresholds of various materials.

Status of Continuing Developments

Plasma-Wall Interactions *(C. C. Damm and G. D. Porter)*. We have continued investigating the requirements of the plasma dump that absorbs the plasma lost in the mirror loss cone. Secondary electrons emitted from this dump may be a significant power drain on the confined plasma. Two secondary suppression techniques were studied.

The first, a grid structure on the dump, is discussed under Direct Conversion. The second, an array of fins oriented parallel to the field lines, is discussed in more detail elsewhere.

We found that the technique appears feasible and that it does not require extraordinary alignment precision. However, some questions remain about the effect of gas evolving off the surface of the fins.

Diagnostics

G. H. Leppelmeier

A tentative list of diagnostics has been prepared for use in estimating costs, schedules, and building *requirements*.

Diagnostics activities for this quarter were mostly related to planning, the main purpose being to identify what measurements should be made in the early experiments on MFTF and to determine what instruments and facilities are required for those measurements. We have prepared a tentative list of diagnostics for MFTF — some of which are well established (on 2XIIB and other magnetically confined plasma machines) and some of which are still undeveloped. The list has been the basis of a detailed estimate for costs and schedule.

The space and support requirements for the diagnostics system, along with the required coupling to the control system, have been used to make proposed layouts of control and diagnostics areas that designate the amount and nature of space required and how the various pieces should be related physically.

Design and Construction

V. N. Karpenko

The MFTF construction project is on schedule.

Magnet System. The magnet system is a major system on the project critical path. Vigorous steps were taken to initiate procurement of long-lead items as early as possible. An order for the superconductor core was placed ahead of schedule and within the planned cost envelope. Specifications for the manufacture of the stabilizing sheath have been completed, and an order has been placed with Airco for the design of the conductor assembly production line.

The coil winder, reel support, platforms, and safety rails were erected in Bldg. 431. Acceptance tests on the coil winder (see Fig. 22) were completed, and the machine is now functioning properly.

We have expended considerable effort in evaluating and choosing a simplified cross section for the magnet coil. Two different configurations were considered. A conventional, rectangular cross section was approved that satisfies magnetic-field and neutral-beam access requirements, avoids complex conic surfaces on the jacket and case (thereby simplifying the winding process and tooling requirements), and provides improved reliability at a lower cost.

A request for proposal (RFP) for analysis and detailed design drawings of the superconducting magnet system has been completed and is being prepared for release to qualified contractors.

Fusion Chamber System. A detailed preliminary draft specification was completed for the fusion chamber system, which includes vacuum vessel, external vacuum, and cryogenic systems, and was mailed to each company expressing an interest in the competitive procurement.

The final RFP for the fusion chamber system is scheduled for release by the end of January 1978.

We have located needed equipment at the Nevada Test Site (NTS). Purchase orders were prepared for early removal and transport to LLL of a compressor that would otherwise be one of the long-lead items in the cryogenic system. Sixty high-pressure storage bottles and an overhead crane were also located at NTS.

Power Supply System for the Sustaining Neutral Beams. We have prepared the preliminary draft performance specification of the power-supply system for the sustaining neutral beams. An invitation for expression of interest was sent out to 32 companies in November. The package included a questionnaire, system requirements, the preliminary draft specification, a list of available technical data, terms and conditions, and a work statement. The companies were asked to respond by mid-December and to comment on including as part of this contract the 230-kV/13.8-kV substation and the site preparation for the accel dc power supplies. Of the 17 companies that responded with interest, 6 are interested as prime contractor. All suggested a separate contract for the 230-kV/13.8-kV substation.

A site location for the 230-kV substation and 80kV rectifier subsystem was chosen and approved. This location satisfies both the LLL master plan and project requirements (including cost). Figure 23 shows a model of the 80-kV power supply.

Power factor correction and harmonic noise generation studies are underway.

A RFP for the power-supply system for the neutral beams is scheduled for release by the end of next quarter; considerable effort is yet to be expended.

Control and Diagnostics System. The specification for the local-control computer was completed and forwarded for approval. These approvals may take longer than the time we have allocated. However, with release of the RFP covering purchase of nine of these computers now expected by late January there should not be any detrimental effect on the delivery schedule.

Bldg. 431. The architect-engineer (A-E) selection process has been completed. The major difficulty in refining criteria prior to negotiations was in deciding on the location of the control room. The original location was discarded because of a hostile magnetic environment; the required shielding cost was considered excessive. The northeast corner of Bldg. 431, where the magnetic fringe field is within acceptable limits, is now a preferred location.

Demolition work in Bldg. 431 progressed on schedule, with the main activity centered in the vault area and the removal of existing roof trusses.

A three-dimensional analytical model of Bldg. 431 for structural dynamic analysis was completed using the proposed floor loadings for MFTF. The results will be used for guidance during design and modification efforts.

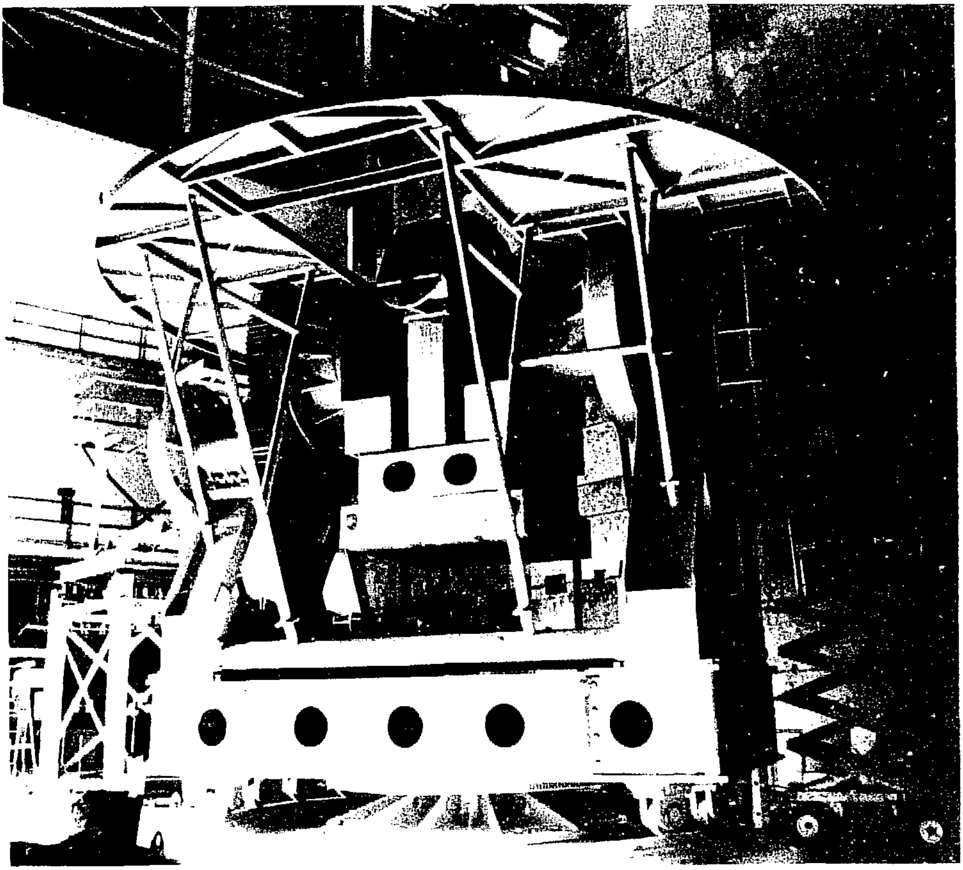

Fig. 22. MFTF coil winder (2 degrees of freedom).

Primary Electric Power. The Environmental Impact Statement was reviewed by LLL, returned to PG&E, and filed with the City of Livermore and Alameda County. In a second contract review meeting with PG&E, we discussed a schedule, power-factor correction, and harmonic current interference signals. PG&E has agreed to a lower power-factor correction requirement at reduced power levels.

PG&E provided the following schedule for the 230-kV power line work: contract signed 3/78, bid materials 2/80, start construction 8/80, and completion 11/80. Although the contract date reflects a 3-month slip in our scheduled milestone, the completion date is 4 months ahead of the completion date for the power-supply system for the sustaining neutral beams.

Building 441. Four firms were interviewed by the A-E selection committee. The design criteria were completed and delivered to the DOE San Francisco Project Office. Combining Bldg. 441 A-E and construction contracts with the "Core I" building should result in a considerable cost saving to the project.

Project Management. The LLL MFTF Project Office reached 90% of the planned project staff level in the first quarter of FY 1978.

Technical effort was concentrated on completing the specification of the requirements for the fusion chamber system, particularly on specifying the gas loads, the cryopanel area and location, and the added thermal loads for the cryostats. Increased pumping capability will probably result in the required helium

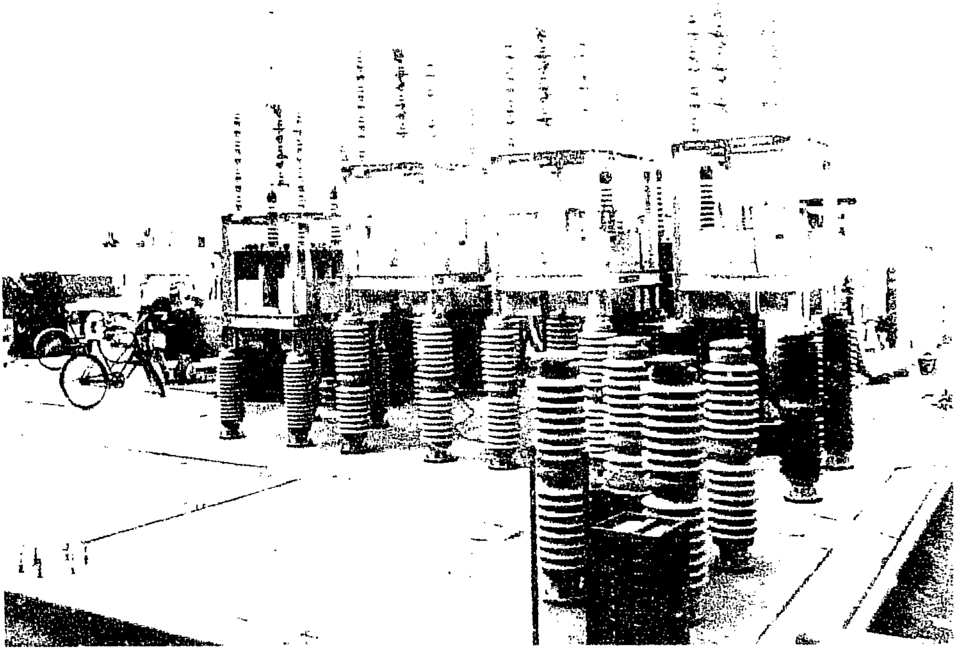

Fig. [illegible] Model of [illegible] kV power supply

[illegible]

- [illegible]
- R[illegible]
- Acceptance [illegible] SANTAS D[illegible] MHI [illegible]

- [illegible] MHI [illegible] M[illegible] R[illegible] A [illegible]

Magnet Systems

Superconducting Magnet Development

[illegible]

The technology of superconductors and superconducting magnets is of vital importance to the building of present-day plasma physics facilities and to the planning and study of future experimental mirror machines and reactors. We are developing a Nb-Ti conductor for the Mirror Fusion Test Facility (MFTF) winding and Nb_3Sn conductors for future mirror devices.

MFTF Conductor Development

[illegible]

solder bonding on each individual "land" on all four sides of the conductor and to call out any land failing to meet a predetermined limit of bonded surface. The 6,500 ft of conductor utilizing core material from Airco, Supercon, and IGC has now been satisfactorily stabilized and shipped to LLL for winding into the MFTF test coil.

The coil form and major insulation for the MFTF test coil have been fabricated and are assembled on the coil winder; winding began in late December.

We have developed a method of replacing the stabilizer around a cold welded joint in the conductor core. In this method, the stabilizer is applied in two right angled pieces, one approximately 8-in. long and the other 17-in. long, thus staggering the joint. Before the stabilizer is applied to the joint, the surface with cooling channels is suitably masked, and 5 mils of 90 Pb-10 Sn (wt%) solder is electroplated onto the lands. Clamps at frequent intervals secure the stabilizer to the core. Three sets of thermocouples attached to the stabilizer are used to control the temperature of the three sections of the soldering oven and to give a continuous record of the conductor temperature during the soldering process. The soldered joint is first ultrasonically tested for quality of bond and then ultrasonically cleaned in a weak-acid bath that is followed by clean-water rinses.

Radial and axial clamps have been fabricated to keep the winding tight during winding and while joints are being made. A controlled tensioning device added to the mechanism controlling the conductor supply drum will maintain tension during winding, while the system is stationary, and also during unwinding.

High-Field Test Facility

The Baseball II liquifier has been re-installed in the Cryogenics Laboratory, and since its re-commissioning, has filled the 10,000-litre storage Dewar.

The 2-m-diam cryostat for the High-Field Test Facility (HFTF) has been installed and cooled to 4.2 K, and several thousand litres of liquid He have been transferred into it. During this test, we checked the performance of the 5-kA vapor-cooled leads for the MFTF test coil.

We have received the new 2,000-A power supply for energizing the first two HFTF backing coils, required for use with the MFTF test coil. It is being installed; the remainder of the equipment, e.g., water-cooled dump resistors, high-current bus-bars, circuitbreakers, and all the electronic components for protection and coil diagnostics, is now being fabricated and installed. All this equipment is needed by the March 1978 start date for tests of the MFTF test coil.

Nb$_3$Sn Conductor Development

The attempts by Airco to establish a more reliable and economical method of incorporating Ta barriers in the Nb$_3$Sn conductors were not entirely satisfactory. Airco was also unable to overcome the basic problem of brittleness of the whole conductor by adding external copper; the "center-bursting" was probably caused by the significant difference in hardness of the bronze core and the surrounding copper. We believe that this difference can be overcome by increasing the number of anneals and changes to the dies. It was agreed that Airco should proceed with a prototype, fully stabilized, 5-kA, 12-T conductor as outlined in Ref. 14.

Critical-current measurements on samples of Supercon nominal 3.5-kA, 12-T Nb$_3$Sn conductors showed them to be resistive. We had expected this because examination at Supercon had shown the filaments to be severely broken. The unusually high reduction ratio used for the extrusion was probably the cause.

Preliminary work on Sn-infiltrated, sintered Nb continues at MCA. Results of this initial phase are not expected until 1978, but they are having some trouble obtaining a low-enough vacuum (~10[illegible] Torr) with available equipment. This problem apparently adversely affects the hardness of the conductor and the feasibility of drawing it.

Plasma Engineering

LLL/LBL Neutral-Beam Development

R. V. Pyle

The LLL/LBL Neutral-Beam Development Group has the responsibility for developing neutral-beam injection systems for mirror and tokamak experiments. Modules with beam energies of 20 to 40 keV have been used on the 2XIIB and Adiabatic Toroidal Compressor (ATC) devices. Current near-term development efforts are directed toward 80- to 120-kV injectors for the MFTF (80-kV), Doublet III (80-kV), and TFTR (120-kV) experiments. The total beam power from each accelerator module will be 6 to 7 MW, in 0.5-s pulses. The users want to place orders for production models in about 1 year. Development goals for the longer term are near steady-state operation, higher energy, and better efficiency; this part of the program is centered on negative-ion production, acceleration, and neutralization. We hope to have 200- to 400-kV injectors based on negative ions developed in time for application in the mid- to late-1980's.

The design and construction of test facilities have been the pacing items in our program. At the end of this quarter, suitable facilities for carrying out the near-term part of our program had been completed (except for delivery of a high-voltage switch modulator tube for the LLL High Voltage Test Stand (HVTS)). One of these test stands (TSIIA, 120 kV, 20 A, 0.5 s) has been operating for about 1 year testing fractional-area (80- to 120-kV) modules and beam-line components. TSIIB (120 kV, 80 A, 30 ms) has been operating for a few months with a full-scale TFTR source, and is still undergoing minor modifications to match the various supplies to the plasma-beam loads.

Our positive-ion based work during the quarter may be summarized as follows:

- 80-kV fractional-area modules have not yet been optimized, but have operated with beams suitable for MFTF and Doublet III (except for total current) at 80 kV, 14 A, and 0.5 s.
- The first full-size, 120-kV, TFTR module tests were started on TSIIB. Operation was at 60 kV at the end of the quarter. No ion source problems were observed, but we are deliberately raising the voltage slowly, while studying power supply-beam module interactions, adjusting time constants, etc.
- 40-kV, 70-A, 10-ms module lifetime reliability tests were carried out on TSIIB to demonstrate operation for 1000 pulses.
- A "MacKenzie bucket" (an arc chamber with magnetic multipole fields on the surfaces) was built and installed on TSIIA.
- A U.S.-USSR neutral-beam development workshop was held at LBL.
- Optical studies were started to investigate possible beam-plasma interactions in neutralizers; these might increase the angular divergence of a neutral beam.
- We completed phase I of a program to "industrialize" the fabrication of ion-source modules. The purpose of this program is to help prepare manufacturers to bid in a realistic way on neutral-beam systems. Phase I was a study of techniques, schedules, and approximate cost estimates. Phase II will be the construction of one or two 120-kV, 65-A, 0.5-s sources with hard seals and ceramic insulators.

Our negative-ion based work during the quarter may be summarized as follows:

- A new, low-energy, accelerator structure was designed and built to make better low-energy (~1-keV) D^+ beams for double charge exchange to D ions in the Cs vapor jet.
- A new source of low-energy D ions for the double charge-exchange experiment was built and tests were started. This is the magnetoplasma-[illegible]

[illegible]

- [illegible]
- [illegible] target experiment [illegible] model.

Direct Conversion

Suppression of Heat Conductivity and Direct Energy Conversion for the Ends of TMX and MFTF. *G. W. H[illegible], W. L. B[illegible], R. W. M[illegible]*

Electrostatic grids being designed for TMX and MFTF will not only suppress heat conductivity but also may extend the lifetime of low-energy, streaming-plasma ions, serve as a diagnostic device, and provide direct energy conversion.

In an open-ended [illegible] temperature [illegible] and other effects. The [illegible] is in the form of cold [illegible] from gas ionization [illegible] from the end wall that are [illegible] ion impact, and [illegible] the production rate of these [illegible] reduced to a negligible [illegible] at the end that will [illegible] Production rates can be suppressed [illegible]

- Gas ionization. The gas [illegible] low enough by pumps [illegible] to make this source of cold [illegible]
- Secondary electrons. R[illegible] netic multipoles, and electrostatic grids [illegible] proposed to provide the required [illegible] sion. Grids can be highly transp[illegible] to pass on to direct conversion [illegible] virtually all mirror reactor designs.
- Thermionic electrons. When [illegible] density is greater than about 100 W[illegible] case in MFTF, grids could [illegible] emission is important. Grids [illegible] designed with sufficient therm[illegible] remain below emission temperature [illegible] pulse.

We are designing grids for use on TMX and MFTF. Besides suppressing [illegible] these grids can serve three purposes:

- The grids may be used to reflect the low-energy streaming plasma required for stabilization, and thereby extend the lifetime of these low-energy ions to more than one transit.
- The grids may be used as a diagnostic device to measure the spatially-resolved flux density and energy of the streaming particles.

- The grids can operate in the energy-recovery mode, thus reducing the heat load and at the same time proving out direct energy conversion.

Vacuum Technology

Cryopump and Getter Pump Development. *T. H. Batzer*

The LLL cryopump test stand with which we are studying new techniques for handling large gas loads has been used to determine the following:

- **The baffle transmissivity,**
- **The cryotrapping rate for He and how it varies with the Ar/He ratio,**
- **The relative effectiveness of CO_2 compared to Ar for He trapping, and**
- **The heat load placed on the cryopanel because of Ar (cryotrapping gas) flow.**

A bulk Ti getter was successfully bench tested.

Cryopumping. The cryopump test stand being used to evaluate pumping techniques for large gas load applications is shown schematically in Fig. 24. The instrumentation (not shown) includes

- Two nude ion gages within the liquid-nitrogen-cooled (LN_2-cooled) enclosure, and one ion gage in the elbow of the room-temperature isolation valve that leads to a turbomolecular pump.
- Two quadrupole analyzers for measuring residual gas, one within the LN_2-cooled enclosure and *one in the elbow of the isolation valve*
- A number of carbon resister thermometers on the liquid-helium-cooled (LHe-cooled) panel and on the chevron that is cooled by LHe boiloff.
- An external gas-handling system for feeding measured flows of gases to the chamber and to the cryotrap manifold

The system can be used in either the cryocondensation mode, in the cryotrapping mode, or as both (as a compound pump)

- We made four separate runs in this configuration. In run #1, we measured the baffle transmissivity. The pumping speed for deuterium was measured at flow rates up to 5 Torr·litres/s (2.8 × 10 Torr·litres/s·cm) (See Fig. 25). The average speed is 51,000 litres/s (6.6 Torr·litres/s·cm). This would indicate a baffle transmissivity of 0.21 for the 120-degree chevron. However, since we don't know the deuterium temperature, and have no practical way to measure it, we plan to repeat run #1 on a bare LHe-cooled panel of known area to determine the transmissivity and (indirectly) the D_2 temperature.

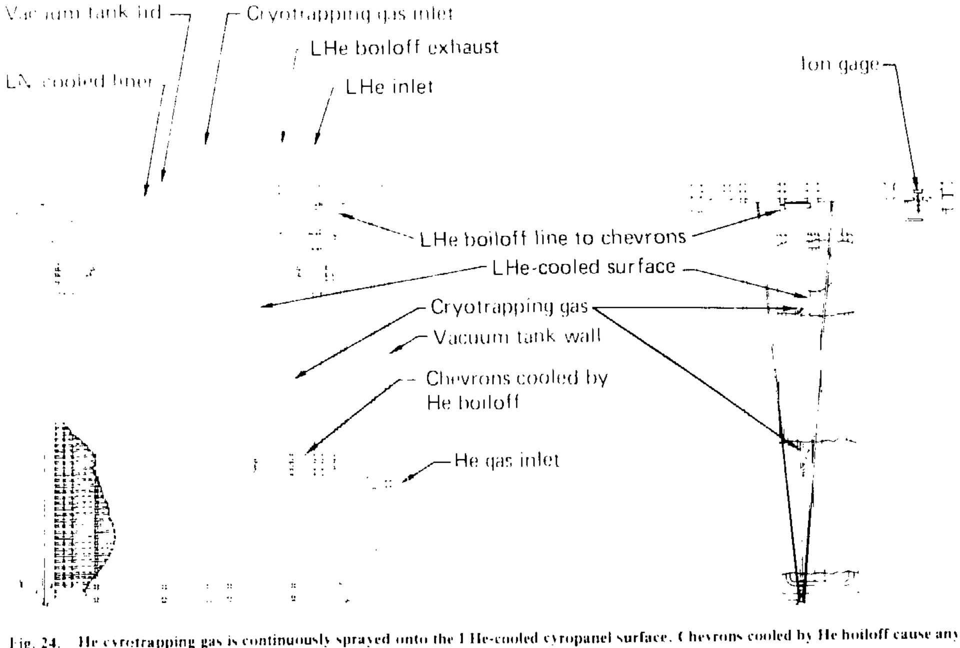

Fig. 24. He cyrotrapping gas is continuously sprayed onto the LHe-cooled cyropanel surface. Chevrons cooled by He boiloff cause any cyrotrapping gas that does not adhere to the LHe-cooled surface to condense. He gas atoms enter the system and diffuse to the cyrotrapping, gas-coated surface, where they adhere and are thus pumped out of the system.

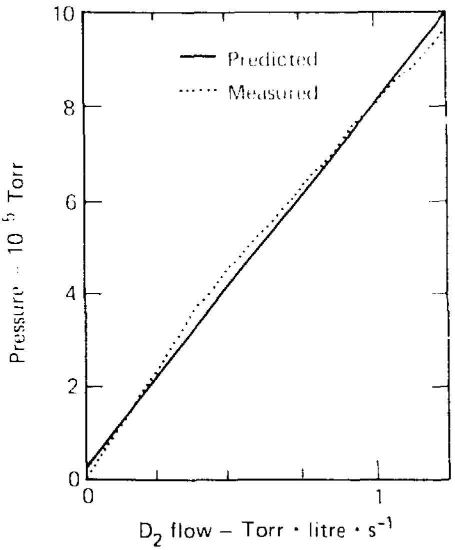

Fig. 25. Pressure vs flow for deuterium.

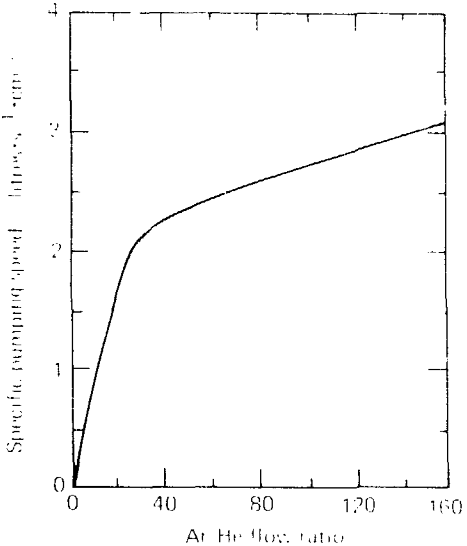

Fig. 26. Variation in the pumping speed of He trapped with Ar with the Ar/He ratio, where maximum He flow = 0.13 Torr·litre·s^{-1}, and maximum Ar flow = 12.3 Torr·litre·s

In run #2, we measured the pumping speed of He cryotrapped with Ar, and determined how it varied with the Ar/He ratio. The resulting curve (see Fig. 26) suggests the following:

- The pumping speed up to the highest point measured (3.04 litre·s^{-1}·cm^{-2}) appears to be limited by the sticking probability of the LHe-cooled panel and not by the chevron transmissivity.
- The two distinct slopes to the curve intersect at an Ar to He ratio of 30:1.
- The slope is always positive.

All three observations appear to be related to the geometry of the cryotrapping arrangement, that is, to the Ar impingement area on the cryopanel. We observe that the He sticking probability on the cryopanel is small and dominates the pumping speed; however, it increases with the Ar/He ratio. At low Ar/He ratios (less than 30:1), the helium sticking probability (for a given Ar impingement area) is a steep function of the Ar/He ratio. A ratio of 30:1 appears to be optimum. This accounts for the initially steep slope. The second shallower (but still positive) slope reflects the diminishing effect of the increasing Ar/He ratio and the concommitant increasing Ar impingement area on the cryopanel that results from gas scattering at the higher Ar flow rates.

As shown in Fig. 24, there are now four tubes with nine holes each blowing Ar on the LHe-cooled cryopanel. Increased coverage of the cryopanel with argon should shift the curve upward so that it asymptotically approaches the curve of baffle transmissivity. We intend to test this by doubling the number of Ar tubes and holes.

Run #3 was our second attempt to test the effectiveness of CO as a cryotrapping gas for He pumping. Our first attempt had failed when the CO quickly froze and plugged the distribution manifold. By superinsulating the manifold for run #3 we obtained five data points before it again froze. Initial indications are that the CO is about twice as effective as Ar for cryotrapping He. We are now putting nichrome heater wires in each distribution tube. If this technique protects the manifold so that further tests substantiate the effectiveness of CO, we shall significantly reduce the refrigeration cost of cryotrapping.

The refrigeration cost of cryotrapping with Ar was measured in run #4. We determined the base heat load (radiation and conduction) to the 1.5 m^2 cryopanel by measuring the LHe boiloff rate with a wet-test meter at the base pressure of the system (p = 6 × 10 Torr). The base heat load was 1.26 W (0.84 W/m^2). The incremental heat load due to flowing Ar on the panel at 180 K (as indicated by a thermocouple on the manifold) was measured at flow rates from 0.2 to 20 Torr·litre/s. The average heat load caused by the Ar flow over this range was 0.523 W/Torr·litre·s, with a standard deviation of 0.038 W/Torr·litre·s.

Figure 27 shows the beam-line cryopump designed for the direct conversion experiments on the Lawrence Berkeley Laboratory (LBL) test stand. It was designed to allow refronting for cryotrapping He. The parts are being fabricated and the cryotrap system is being designed.

Getter Pumping. The bulk Ti getter pump shown in Fig. 28 has been successfully bench-tested. It will be installed in a vacuum test chamber that is being built to test its pumping speed. We anticipate [illegible] the characteristics of the [illegible] system.

Reactor Materials

RTNS-II

[illegible]

The RTNS-II facility will provide the neutrons required to determine the response of potential fusion reactor materials to 14-MeV neutron irradiation. Areas of research to be explored with this machine include radiation effects on superconductors, damage-rate studies, changes in observable microstructure, and changes in physical properties. A major emphasis of this work will be to develop the knowledge and methods required to relate data from other radiation sources to the fusion-neutron environment. We anticipate some effort in measuring neutron and gas production cross sections.

During the first quarter of FY 1978, our effort on the RTNS-II project was concentrated in two areas:

- To bring to approximately 99% completion the physical plant of the new facility, and
- To complete the assembly of one of the two deuteron accelerators that will be used for full-scale proof-of-design tests.

The physical plant of the new facility is now complete in all respects with the exception of minor exterior paving and landscaping. Assembly of the prototype accelerator was completed during this quarter and operational tests of all major subsystems were begun. Mechanical systems such as vacuum and cooling for the high-voltage terminal and the beam-transport system were tested successfully, as were electrical systems such as the 400-kV high-voltage power supply, the ion-source power supplies, and ground-to-terminal and terminal-to-ground controls and telemetry.

Programming of the calculator-controlled data recorder that will serve both the neutron sources and the experiments was begun during this period. All terminal systems were operated, and the multiple-aperture source (MATS) reflex-arc ion source successfully delivered 100 to 200 mA of both atomic and molecular hydrogen beams to the position of the acceleration column. Testing of the acceleration column in the next quarter will terminate activities of the prototype accelerator.

During this quarter, we also began initial tests of the 50-cm, 5000-rpm rotating target. Inadequacies in the original bearing design for this target were noted and modifications to that bearing begun. Construction of target loading facilities for this project at Oak Ridge National Laboratory (ORNL) were approximately 50% complete by the end of this quarter.

Construction of the physical plant and the neutron sources themselves remains well within the original schedule and cost estimates for the project. We expect initial operation of the neutron sources in June of 1978, with full-scale experimental activities beginning in October of 1978.

14-MeV Neutron Irradiation Studies

Correlation of Neutron Damage with Neutron Sources. *J. B. Mitchell, R. R. Van[illegible], and [illegible]*

The high-energy neutron sources* planned for the radiation effects program are the Rotating Target Neutron Source (RTNS-II) currently under construction at LLL and a Li(d,n) stripping source, which is in the design stage. These sources are expected to provide a neutron flux of from 10[illegible] to 10[illegible] n/m^2·s.

At the present time, we are using low-flux prototypes of these sources:

- **RTNS-I at LLL has a maximum flux of 10^{16} n/m^2·s.**
- **Be(d,n) stripping sources — one of these is at the University of California at Davis and has a flux of 7×10^{16} n/m^2·s.**

Although radiation damage experiments on these low-flux prototype sources cannot produce the high neutron fluence ($\sim 10^{26}$ n/m^2) for evaluating the structural integrity of materials for the first wall of a fusion reactor, they can provide a basic understanding of the nature and magnitude of high-energy neutron damage effects. They also allow direct comparison and correlation of high-energy neutron damage effects with ion and fission-reactor neutron damage effects.

This quarter we report the results of some exploratory studies on the nature and magnitude of radiation damage effects produced by high-energy neutrons from the RTNS and Be(d,n) sources.

Vanadium and Nb-1wt% Zr. Tensile specimens of vanadium and Nb-1 wt% Zr† were irradiated with

---

*The convention used here is that neutron sources which produce a spectrum with neutron energies of 14 MeV are high-energy neutron sources.

†Designated Nb-1Zr.

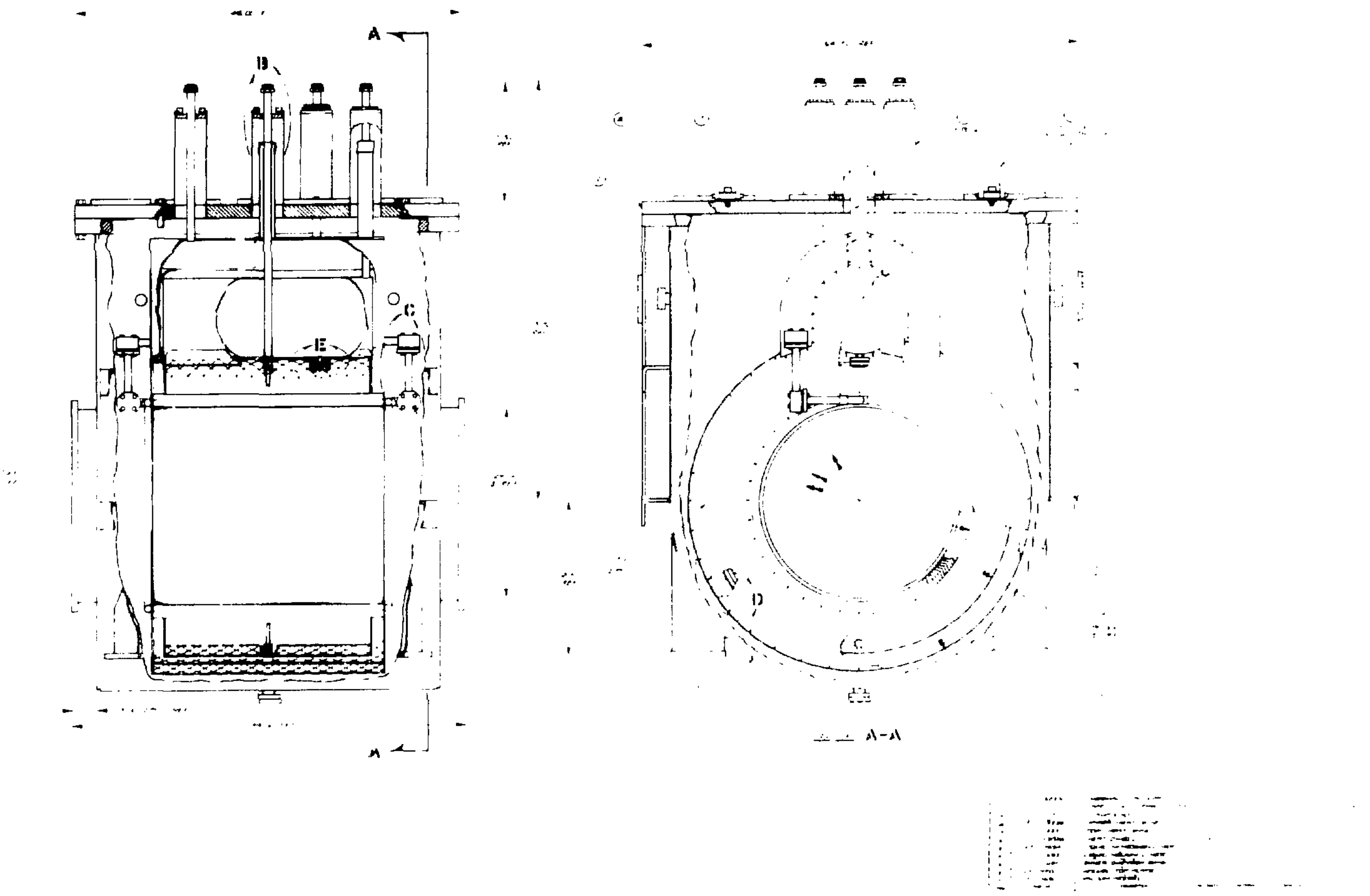

Fig. 27 Beam line cryopump designed for direct conversion experiments

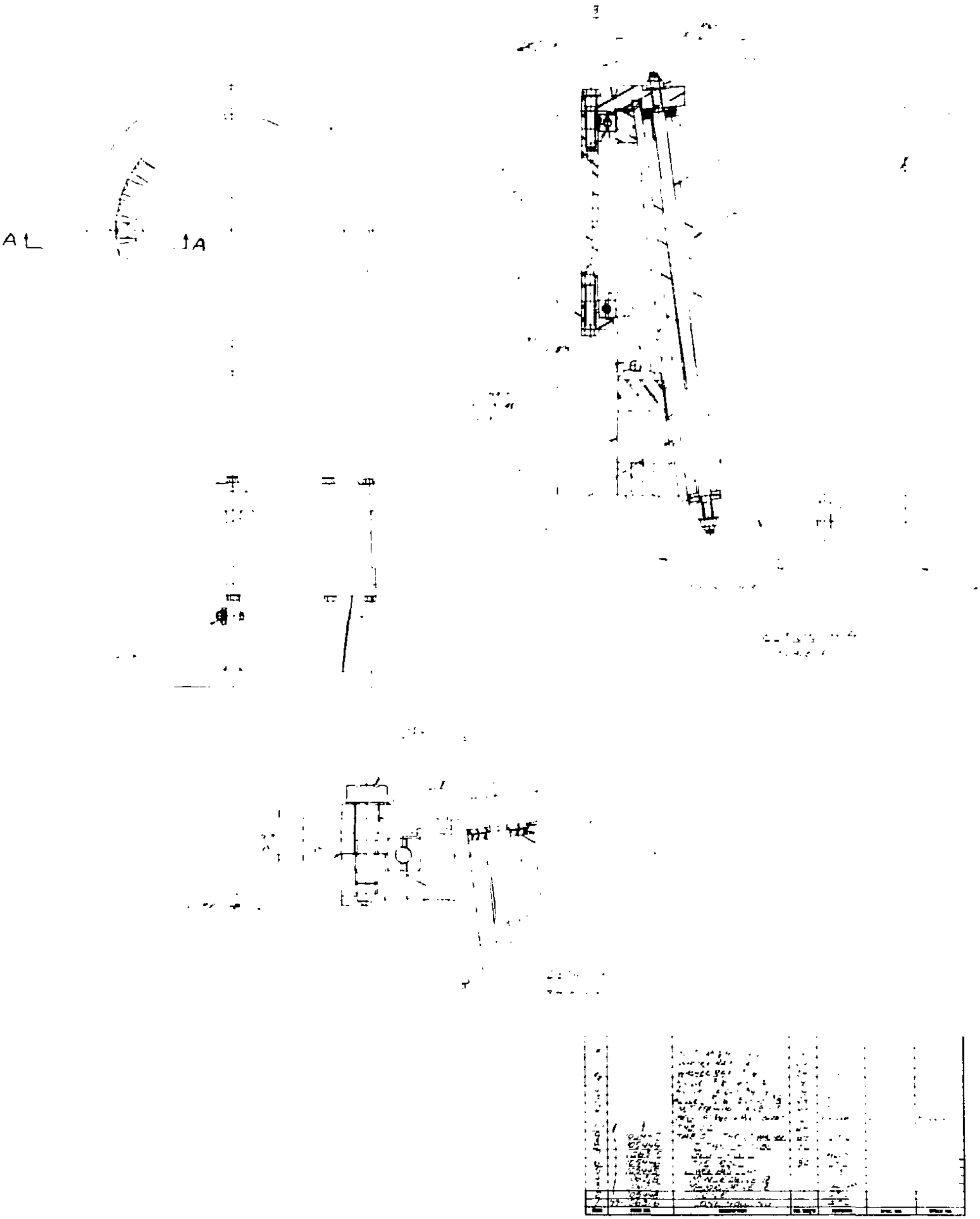

Fig. 28. Bulk Ti getter pump.

neutrons from RTNS and the Liquid Pool Type Reactor (LPTR). The yield strength versus neutron fluence is plotted in Fig. 29 along with previously obtained data for niobium. These results continue to support strengthening trends previously reported for RTNS and LPTR irradiations of niobium. That is, yield strengths increase as a function of neutron fluence, and high-energy neutrons from the RTNS are considerably more effective than fission-reactor neutrons in strengthening these materials.

Type-316 Stainless Steel. The Department of Energy Breeder Reactor Development Program has provided considerable data on the behavior of stainless steels in a radiation environment. Consequently, stainless steels have been proposed as candidates for fusion reactor first walls. The behavior of stainless steel in a fusion-reactor environment is being investigated.

Specimens of annealed and cold-worked type 316 stainless steel will be irradiated at room temperature and elevated temperature at the RTNS and the Be(d,n) source. We will relate fluence and damage energy to changes in tensile properties and use electron microscopy to analyze the size, density, distribution, and morphology of radiation-induced defects. Strengthening mechanisms governing deformation behavior will be determined and the results interpreted in terms of the damage microstructure. Data from tensile tests and electron microscope studies of specimens irradiated with high energy neutrons will be compared with similar data from fission-neutron irradiation experiments. We will then compare the relative damage effectiveness of neutrons from different radiation sources.

Two type 316 stainless steel specimens (one annealed and one cold-worked) were irradiated[8] at the Be(d,n) neutron source. The chemistry and history of these specimens has been reported. The beryllium target was bombarded with 30 MeV deuterons with an average beam current of 23 μA. The deuteron beam was rastered on the beryllium target so as to produce a nearly uniform neutron flux on the gage section of the stainless-steel tensile specimens. The neutron spectra under these conditions have been determined by foil activation analyses (see "Characterization of a Be(d,n) Neutron Source" and Ref. 17). The irradiation was carried out at room temperature, and the experimental set up is shown in Fig. 30. Fluence for the annealed specimen was 2.1 × 10[illegible] n/m², and that for the specimen cold rolled 3[illegible] was 1.8 × 10[illegible] n/m². Average flux was about 8 × 10[illegible] n/m²·s.

After irradiation, the specimens were tensile tested and the data were compared with the results of tensile tests on type-316 stainless steel specimens irradiated with 14-MeV neutrons at the RTNS. The stress-strain curves are shown in Fig. 31. Irradiation of the cold-worked specimen with Be(d,n) neutrons caused

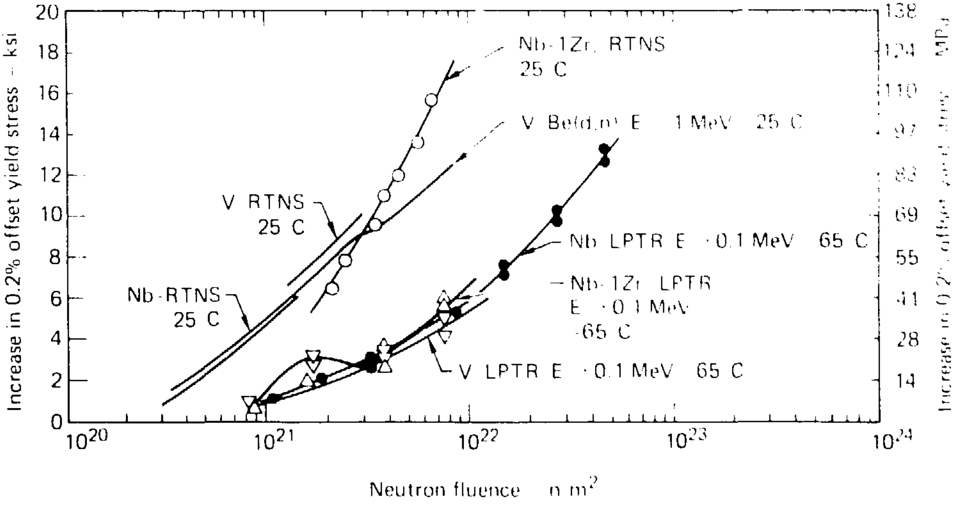

Fig. 29. Comparison of the increase in 0.2% offset yield stress for niobium, vanadium, and Nb-1Zr versus neutron fluence for the Rotating Target Neutron Source (RTNS), Liquid Pool Type Reactor (LPTR), and Be(d,n) neutron sources. These new results for vanadium and Nb-1Zr are consistent with the radiation strengthening trends previously reported for niobium.

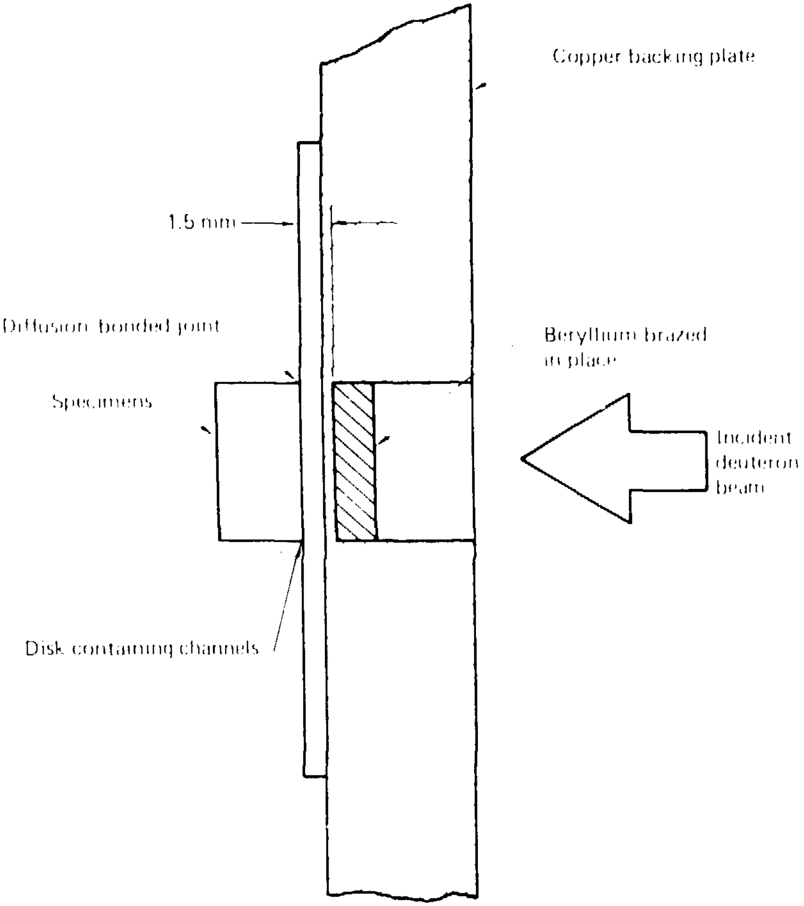

Fig. 30. Specimen-target arrangement for neutron irradiations at the U. C. Davis cyclotron. The beryllium target is cooled by water passing through cooling channels in the copper. A 30-MeV deuteron beam incident on the beryllium target produced a neutron spectrum with a large component of neutrons of $E_n > 4$ MeV and is being utilized in our MFE radiation-damage program.

a slight increase in yield and ultimate stength and a slight decrease in elongation. The changes in tensile properties were similar to those in specimens irradiated with 14-MeV neutrons. The changes in tensile properties of the annealed specimen irradiated with Be(d,n) neutrons were not as large as those produced by 14-MeV neutrons at nearly equivalent fluences, but there was a 30% increase in yield strength and a decrease in elongation from 70% to 62% with respect to the unirradiated specimen. However, the radiation strengthening and loss of ductility after irradiation with 14-MeV of Be(d,n) neutrons are significantly greater than those produced by fission-reactor neutrons.[18]

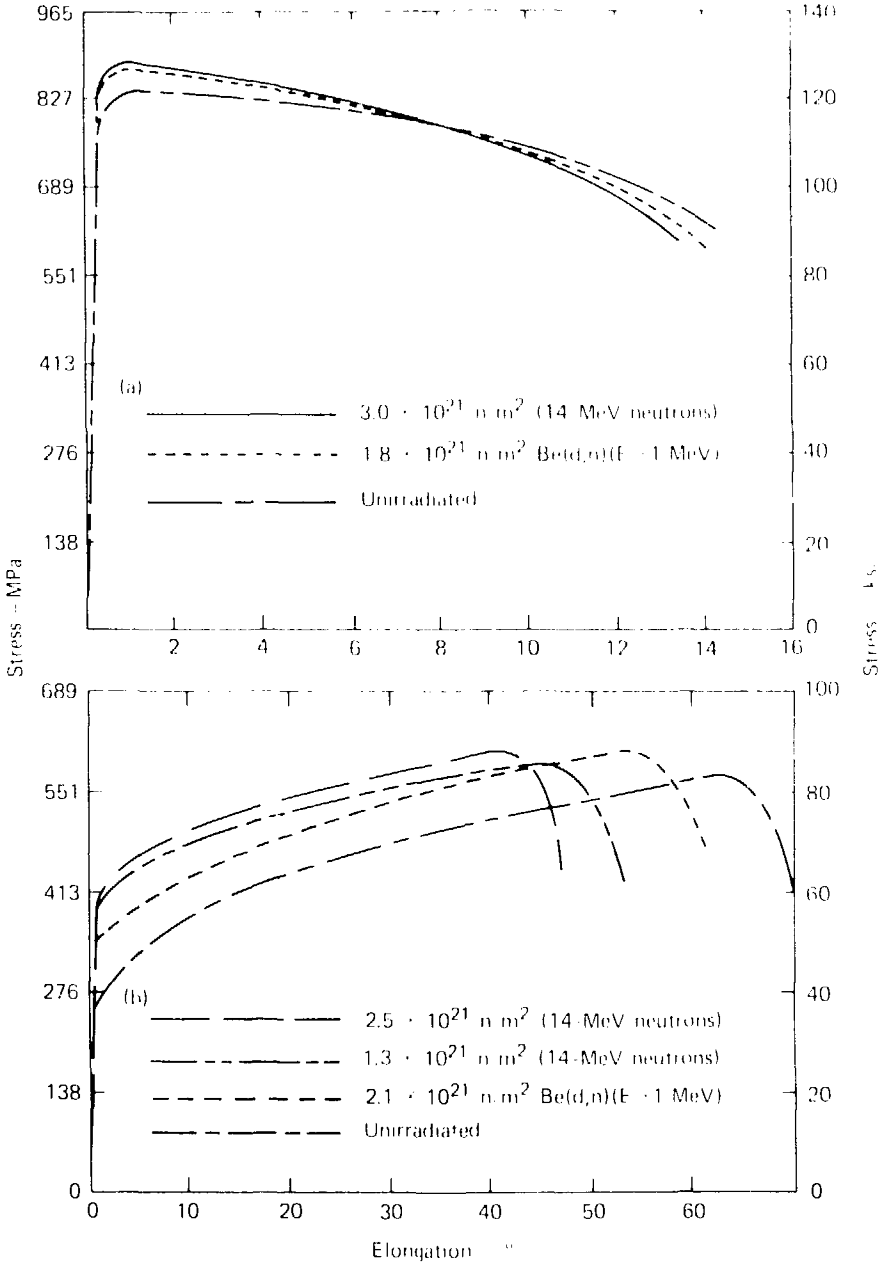

Fig. 31. Changes in properties of 316 stainless steel after neutron irradiation. The yield strength of the cold-worked sample (a) increased by 5%. Elongation was reduced 15%. For annealed 316 stainless steel (b), the yield stress increased by 60%, and elongation decreased 33% with respect to the unirradiated sample.

In Situ Creep Testing. (*W. L. Barmore* [illegible] *R. R.* [illegible])

We are studying the effects of **14-MeV neutron irradiation on the elevated temperature creep of niobium and Nb-1Zr at the Rotating Target Neutron Source (RTNS). The relationships between creep rate, stress, temperature, and microstructure are being examined as a function of 14-MeV flux and fluence. To maximize radiation effects, we have designed and built testing equipment that can be placed close to the RTNS.**

A [illegible] adapted to [illegible] RTNS beam. [illegible] at temperatures to 850°C, applied [illegible] stresses [illegible] MPa (30,000 psi), and maintain [illegible] than 7 mPa [illegible]. Specimens [illegible] in a cylindrical stainless steel tube with copper [illegible] seals. Tensile loads are applied [illegible] a pulley system through a flexible metal bellows. The specimens are heated from one side by thermal radiation from a 127-μm thick tantalum foil heater while temperatures are determined from three thermocouples welded along the gage section of the specimen. Specimen temperature can be controlled to ±3°C. Creep experiments are controlled remotely with control and recording instruments located about 20 m from the creep frame and RTNS head.

Tensile creep was measured on annealed niobium at stresses of 55 MPa (8000 psi) and 86 MPa (12,500 psi) at 800°C and 700°C, respectively. Constant stress was obtained during the experiment by remotely dropping incremental weights from the load column. Elongation was determined from a transducer attached across the bellows in the load column. With this device and associated electronics, the length of the specimen could be monitored to ±3 μm.

Creep tests were run with the beam off until a steady-state secondary creep rate was obtained. The RTNS beam was then turned on while temperature and loads were held constant and deformation rates were recorded. Under these conditions, the radiation-induced vacancies augment the thermally-produced vacancies and could cause a change in the creep rate, provided plastic deformation is vacancy controlled in this tempertture region.

Creep tests were run continuously while the beam was turned on and off alternately about every 30 minutes. At 700°C, the creep rate appeared to increase slightly. At 800°C, no enhancement of creep rate was observed. During this experiment, the 14-MeV flux was 4.4 × 10[illegible] n/m²·s at the center of the specimen. The total 14-MeV fluence at the center of the specimen was 3.2 × 10[illegible] n/m² during irradiation creep testing.

Helium Effects on Mechanical Properties. (*W. L. Barmore, R. M. Scanlan, and R. R. Vandervoort*)

High-energy neutrons not only cause displacement damage, but also produce helium atoms in metal matrices by interacting with metal atoms via the (n,α) reaction. Helium gas bubbles trapped in the microstructure can alter the mechanical properties and lead to embrittlement as helium accumulates. To separate and study helium effects on mechanical properties, we have doped niobium and Nb-1Zr tensile and creep specimens with various concentrations of ³He.

We have completed the series of tensile tests on annealed Nb-1Zr specimens and Nb-1Zr specimens doped with 25 atomic ppm ³He. Results are given in Table 4 along with data reported last quarter. The influence of 25 atomic ppm ³He on the mechanical behavior of Nb-1Zr tensile specimens is small. At 200 and 400°C, the helium apparently lowers the yield

Table 4. High-vacuum tensile tests on Nb-1Zr.

³He, atomic ppm	Temperature, °C	Yield stress, MPa (ksi)	Ultimate stress, MPa (ksi)	Strain, %
0	23	150 (21.7)	260 (37.7)	50.8
25	23	165 (24.0)	279 (40.5)	46.4
0	200	106 (15.4)	202 (29.4)	42.6
25	200	92 (13.3)	194 (28.2)	45.0
0	400	84 (12.2)	188 (27.2)	26.3
25	400	82 (11.9)	190 (27.6)	31.0
0	600	68 (9.8)	217 (31.3)	35.2
25	600	85 (12.3)	208 (30.2)	32.8
0	800	60 (9.0)	199 (29)	32.0
25	800	78 (11.0)	221 (32)	27.0

strength, but produces little change in the ultimate stress and the fracture strain. For tests on doped specimens at 23, 600, and 800°C, yield strength is increased and elongation decreased slightly. We conclude that the effects on the tensile properties of the addition of 25 atomic ppm ^3He in the microstructure of the Nb-1Zr alloy specimens are not deleterious.

Radiation Damage in Superconductors. *R. M. Scanlan*

To design the magnet shielding for magnetic fusion reactors now in the planning stages, we must know the effects of radiation on candidate superconducting materials as a function of fluence. Calculations for a tokamak reactor predict a total neutron flux of between 4×10^{12} and 4×10^{13} n/m²·s at the superconductor. These flux calculations are based on perfect shielding, and as more refined calculations are made that incorporate neutral-beam injection ports, etc., the flux values at localized areas of the magnet will increase. The magnets must be used for many years; their radiation tolerance may become the controlling factor.

The work in progress has the following three objectives:

- **To determine the effects of neutron irradiation (from about 4 MeV to 14 MeV) on the critical current of Nb_3Sn, Nb-Ti, and other superconductors at liquid-He temperatures and in the presence of magnetic fields up to 12 T.**
- **To correlate the electrical properties of these materials with both initial microstructure and radiation-induced changes in microstructure.**
- **To measure the recovery of the changes in the critical current during annealing at temperatures up to room temperature.**

The goal of the present series of experiments is to find the fluence at which a decrease in I_c occurs for Nb_3Sn irradiated with 14-MeV neutrons and to compare this fluence with the fission-neutron results.

During the quarter we completed baseline measurements of the superconducting properties (I_c and T_c) for two Nb_3Sn superconductors (monofilament wire obtained from Brookhaven National Laboratory and multifilament wire supplied by Airco, Inc.) in preparation for an irradiation experiment on the RTNS. One sample of each material was then irradiated for 2 weeks at 4.2 K. At selected intervals, we measured the superconducting properties; we observed an increase of 25% in critical current at a fluence of 8×10^{20} n/m². The behavior is similar to that found for Nb_3Sn irradiated at low temperature with fission-reactor neutrons. That is, the critical current increased with fission-neutron fluence to around 5 × 10 [illegible] n/m [illegible] MeV [illegible] decreasing.

To complete the comparison defined in the experiment goal, we must extend our irradiations to higher fluences.

Characterization of the Davis Be(d,n) Neutron Source. *M. W. Guinan and S. C. MacLean*

The (d,n) reaction on beryllium provides a source of neutrons that may be useful in studying the effects of intense fast-neutron irradiation on materials that might be used in future fusion reactors. We examined the spectrum and intensity of the neutrons available at the University of California, Davis, cyclotron.

We have measured the neutron spectra produced by bombarding thick beryllium targets with 30-MeV deuterons at the Davis cyclotron. The spectra were inferred from the activation of two sets of detector foils placed at an angle $\theta = 0°$ to the deuteron beam, one immediately behind the beryllium target block and one 40 mm to the rear. We used the SAND II program to analyze the foil activation data to obtain the fluence in each of 100 energy groups. The results are shown for both detector foils in Fig. 32. The neutron spectrum (fluence/MeV) close to the target decreases continuously with energy in the range 2 to 30 MeV, while the spectrum 40 mm back has a minimum at about 8 MeV and a peak at about 14 MeV. The contribution from neutrons of energies less than 10 MeV is much greater than that found in previous spectral measurements made at large distances from the target. We attribute this difference to the neutrons that are emitted at large angles from the deuteron beam. These observations show the importance of evaluating the neutron spectrum near the target if samples of materials are to be irradiated in this location.

Fusion Systems Engineering

Tritium Control and Handling

Tritium Processing and Control Systems. [illegible] *Sherwood*

Proposed fusion reactors will have a large tritium inventory. Containment and cleanup systems will be needed to limit personnel exposures and population dose. Also, fusion research facilities presently being designed will require tritium cleanup systems. Tritium can be removed from effluent air by catalytic oxidation followed by water adsorption. However, available performance characteristics and basic data for the design of tritium/air cleanup systems are inadequate. Our program has the following objectives:

- **To develop mathematical models for engineering design of tritium cleanup systems.**

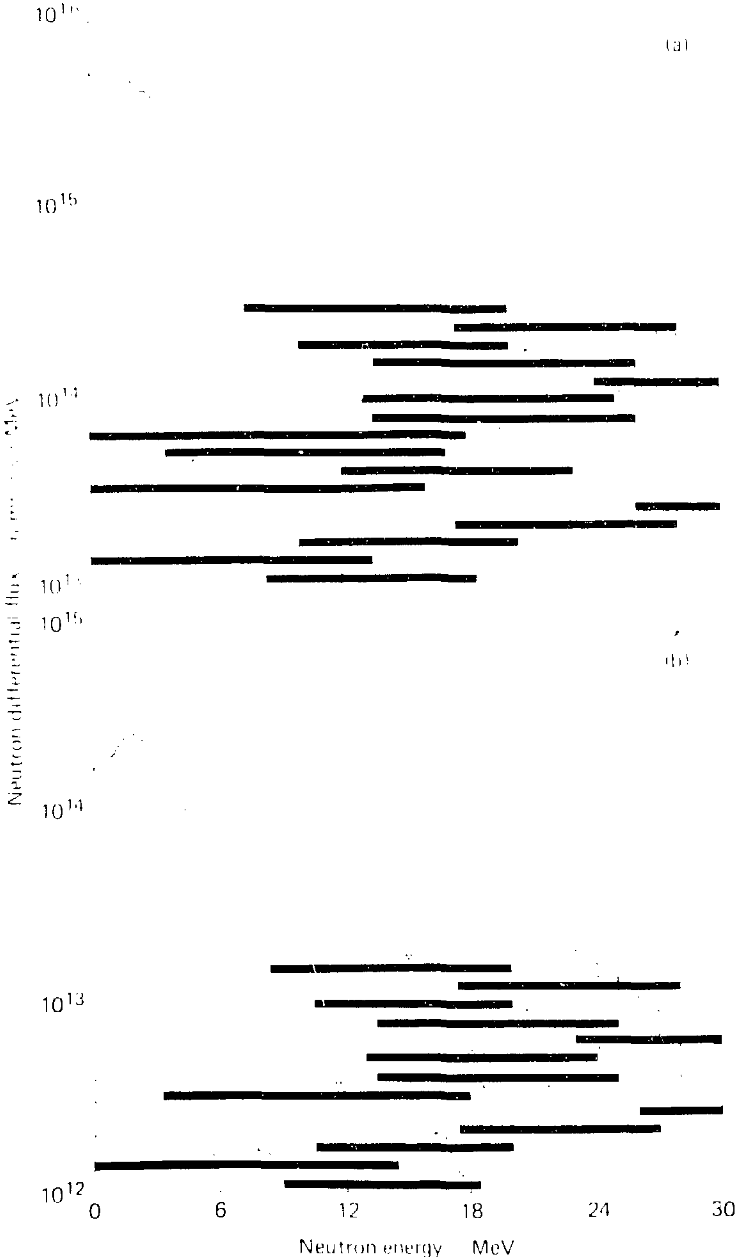

Fig. 32. The neutron spectrum has been determined for 30-MeV deuterons incident on a beryllium target (a) immediately behind the target and (b) at 40 mm from the target. The horizontal bars indicate the range of neutron energies over which a given detector was used and the nuclear reaction that is involved.

- **To obtain data on the kinetics of oxidation and adsorption bed dynamics.**
- **To develop the instrumentation for real-time discrimination of tritium gas and tritiated water vapor.**

A new maintenance enclosure (7 m[illegible]) was built with a catalytic oxidation tritiated-water-adsorption cleanup train. This system is currently undergoing start-up check-out testing. The room-temperature catalyst functioned satisfactorily for a short time and then become ineffective; we believe it was poisoned by mercury vapor introduced when the contaminated transfer pump was disassembled.

To reduce the tritium level in the enclosure, we set up a small drag-stream recycle loop at [illegible] 1 × 10[illegible] m[illegible]/min, using a palladium catalyst/molecular sieve. Ion chamber readings downstream from the catalyst/adsorbent are shown in Fig. 33. The conversion factor to tritium concentration is ~7 × 10[illegible] μCi/m[illegible] per ampere.

Two features are of interest in the figure. The first is the steady exponential decline of concentration for about a day. This translates to ~50% conversion per-pass through the catalyst. The catalyst is either unaffected by the poison or, more likely, the poison has all been adsorbed on the built-in catalyst/adsorbent. The second feature of interest is the break-through of tritiated water at ~2 days. This break-through is consistent with calculations based on the known behavior of ordinary water on this type of adsorbent.

Tritium Processing and Control Using Active Metal Getters, *M. E. Singleton*

Our investigation is directed toward selecting and characterizing the hydriding behavior of suitable "getter" materials. There is a vast array of metals, intermetallic compounds, and alloys that form hydrides. Their dissociation hydrogen pressures and hydrogen capacities vary widely. We are interested in selecting and studying the behavior of the hydride formers that would best fulfill MFE requirements for tritium cleanup. The hydride should have a low dissociation pressure (< 0.3 mPa) at hydriding temperatures and (for easy recovery of the tritium) a high dissociation pressure (> 100 kPa) at a moderately elevated temperature.

Previously [illegible] reported [illegible] certain traps [illegible] inversely proportional [illegible] deuterium [illegible] metal reacted [illegible] rate [illegible] experiments were carried [illegible] tions of deuterium [illegible] have been analyzed [illegible] Reynolds number [illegible] expression [illegible] to the equation

$$[illegible] \quad PF = K [illegible]$$

where K′ [illegible] bed [illegible]

P = pressure (kPa)

G = flow rate [illegible]

PF = purification factor [illegible] into trap [illegible]

Purification factors up to [illegible] were [illegible] for both uranium and cerium at deuterium [illegible] ratios less than 1. In this region, the model [illegible] seem to hold (Fig. 34). Many of the data points were limiting values, because the outlet [illegible] deuterium was below [illegible] same [illegible] region [illegible] concentrations of [illegible] argon, purification factors ranged from [illegible] appeared to be independent of flow rates [illegible] litre/min), hydriding material (cerium or uranium) and temperature (25 to 200°C). The only difference in the two materials studied appeared [illegible] of the purification factor on heating the traps above 200°C. The efficiency of the uranium trap decreased rapidly and the cerium increased to a maximum at about 550°C (Fig. 35).

The results indicate we should continue to characterize different hydriding materials and vary the parameters such as bed length and trap design. Also, work is needed on different models for analyzing the data.

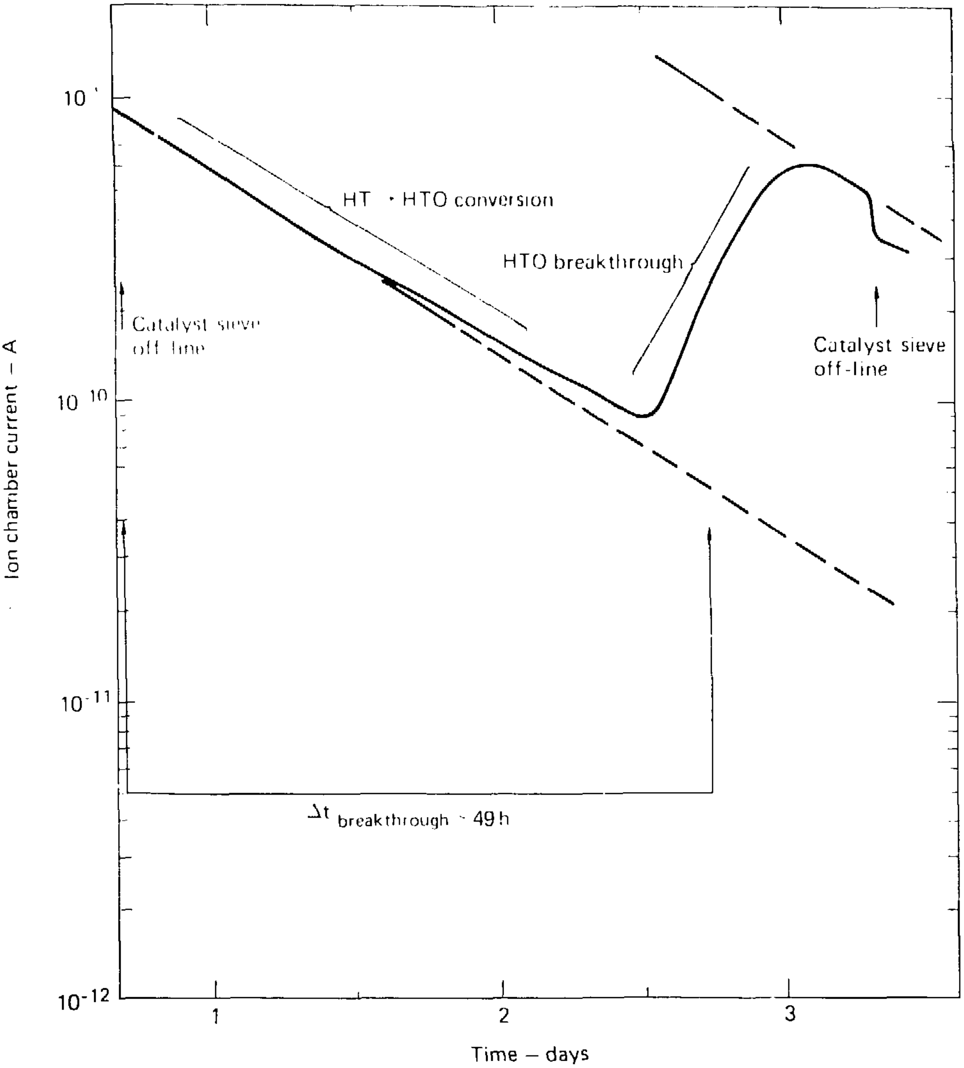

Fig. 33. Tritium adsorption on palladium catalyst molecular sieve adsorbent. Tritiated-water breaks through after about 2 days.

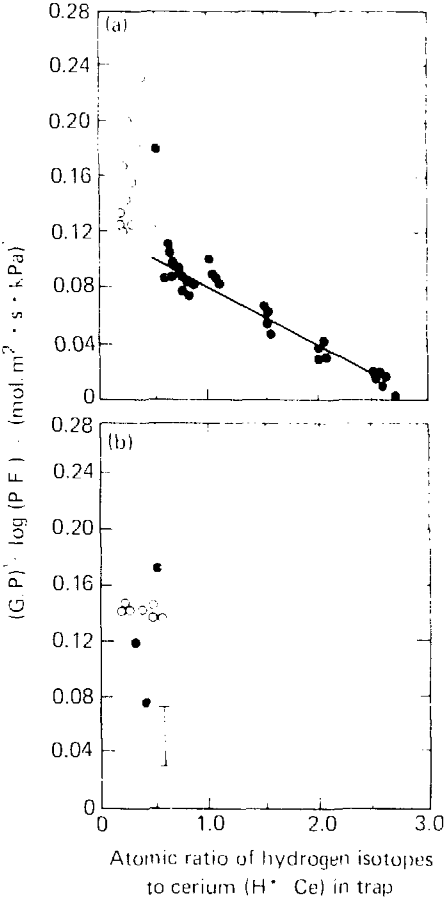

Fig. 34. Comparison of experimentally measured uranium (a) and cerium (b) trap efficiencies with theory based on flow through a packed bed at low Reynolds number (straight line). The data fit this model at deuterium metal ratios greater than 1, but not for ratios less than 1. The range of value measured for tritium for tritium metal ratios less than 1 are indicated by the vertical bars. The open circles indicate data which was at background level for our instrumentation, and the purification factors may be higher.

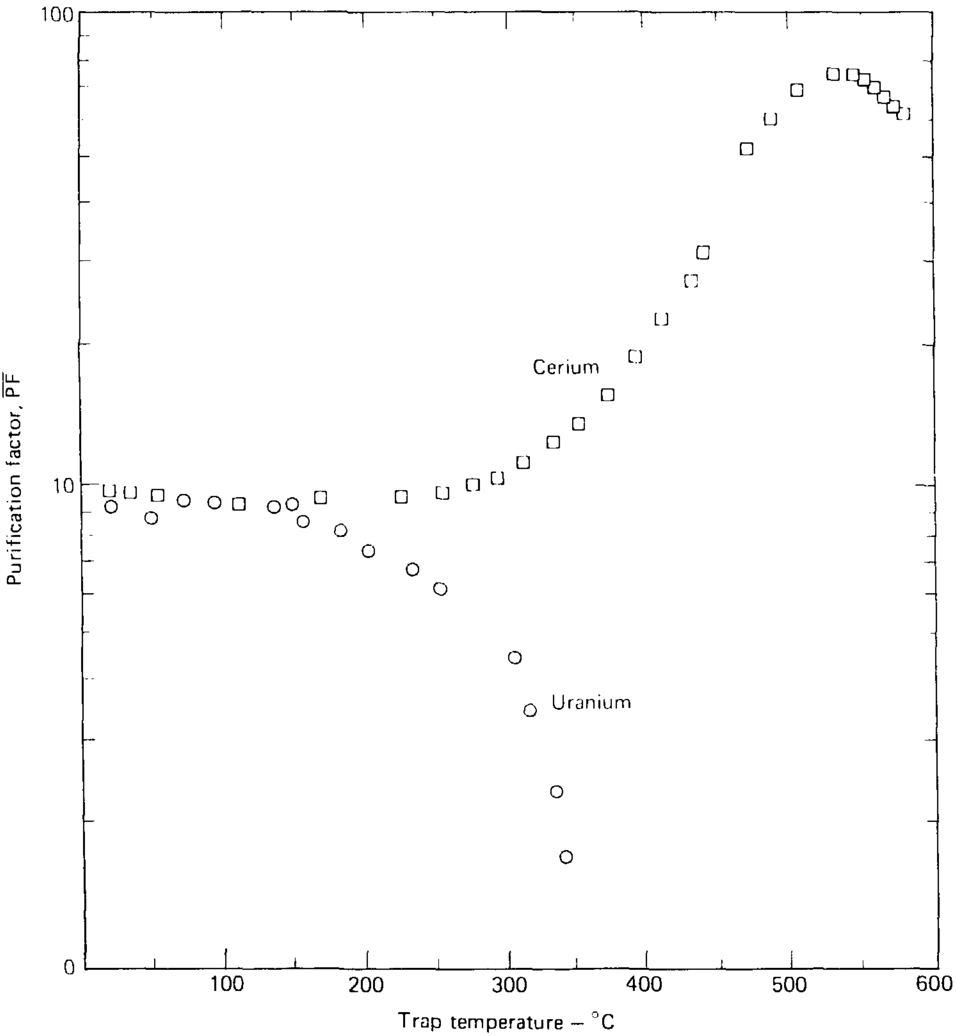

Fig. 35. Effect of temperature on the hydriding efficiency of uranium and cerium. The efficiency of cerium increases to about 550 °C, while the efficiency of uranium starts dropping rapidly at 200 °C. These curves are for low concentrations of tritium in argon.

3. APPLIED PLASMA PHYSICS

Applied Plasma Physics is a major sub-organizational unit of the MFE Program. It includes Fusion Plasma Theory and Experimental Plasma Research.

Fusion Plasma Theory has the responsibility for developing theoretical-computational models in the general areas of plasma properties, equilibrium, stability, transport, and atomic physics. This group has responsibility for giving guidance to the mirror experimental program. There is a formal division of the group into theory and computational; however, in this report the efforts of the two areas are not separated since many projects have contributions from members of both.

Under Experimental Plasma Research, we are developing the intense, pulsed ion-neutral source (IPINS) for the generation of a reversed-field configuration on 2XIIB. We are also studying the feasibility of utilizing certain neutron-detection techniques as plasma diagnostics in the next generation of thermonuclear experiments.

Fusion Plasma Theory

Quasi-linear Codes for Ion Transport in Mirrors

H. L. Berk, L. A. Cutler, Y. Matsuda, T. D. Rognlien, and J. J. Stewart

Work continues on comparing the results from quasi-linear codes that include empirical damping terms with experimental results from 2XIIB.

Our work with the quasi-linear codes for the drift-cyclotron loss-cone (DCLC) instability has focused on testing several empirical models for additional damping, which we find is needed to produce a reasonable saturation level for the instability in the presence of a density gradient. In one scheme, we assumed that the electrons were responsible for the additional dissipation. The power extracted from the waves by the damping term was therefore used as input to the electron energy equation. This resulted in large periodic pulses of rf and electron temperature. The magnitudes of the pulses were too large in comparison with the 2XIIB experimental data, indicating that the additional dissipation does not come from the electrons.

We have done some comparison with time-dependent results from 2XIIB. When a constant damping factor is used, we find that we can obtain reasonable results for one portion of the experiment, e.g., after the stream is turned off. However, this same damping factor does not yield good comparison with the time when the stream is on, the damping then being too large. To compare well with the experiment, the damping must change with time when the rf amplitude changes; we therefore conclude that the damping may be nonlinear in origin. We are also investigating the work of Aamodt et al.,[18] which considers non-linear frequency shifts.

We have also progressed towards modifying the one-dimensional (v^2) code to make the neutral-beam absorption valid for both the thick- and thin-plasma cases. We have checked out the version of this code that considers the first generation of neutrals; the effect of multiple generations will be implemented in the future.

Monte Carlo Neutral Transport Code

T. B. Kaiser

The Monte Carlo neutral-transport code briefly described in Ref. 1 continues to be developed as an interpretative tool for the understanding of experimental data. Toward this end, a version of the code is being readied for incorporation as a standard diagnostic in SUPERLAYER.

An illustration of the kind of information available from the Monte Carlo code in its present form is presented in the accompanying figures. The SUPERLAYER steady-state particle distribution from run RF 17, which simulates the 2XIIB shot of 4/14/77, was used as a target plasma into which neutral beams were injected with the boundary conditions

$$\frac{dJ}{dE}\,(\mathrm{A/cm^2\cdot keV}) = \frac{I_0\,[\delta(E-E_b)+\delta(E-\frac{1}{2}E_b)]}{8\pi(\Delta x)_b(\Delta Z)_b}\,\exp\left[-\frac{Z^2}{2(\Delta Z)_b^2}\right]\cdot\left\{\begin{array}{ll}\hat{e}_x\exp\left[-\dfrac{(x-x_b)^2}{2(\Delta x)_b^2}\right], & x=-16\ \mathrm{cm}\\[2ex] -\hat{e}_x\exp\left[-\dfrac{(x+x_b)^2}{2(\Delta x)_b^2}\right], & x=16\ \mathrm{cm}\end{array}\right.$$

with I_0 = 400 A, E_b = 18 keV, $(\Delta x)_b$ = 1.62 cm, $(\Delta Z)_b$ = 6.23 cm, and x_b = 3.5 cm. The geometry of the simulation is given in Fig. 36.

In Fig. 37, the flux of neutral particles into the detector is plotted as a function of detector scan position, x. The code results are plotted as plus signs, with one-standard-deviation statistical uncertainties due to finite sampling indicated. The circled data points are from the 4/14/77 2XIIB shot, normalized to the total flux computed by the code. The mean position of the charge-exchange event responsible

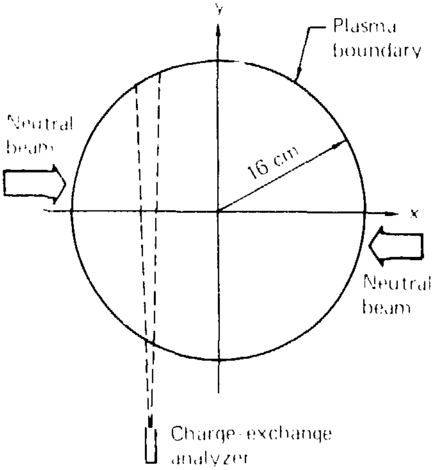

Fig. 36. Geometry of the simulation.

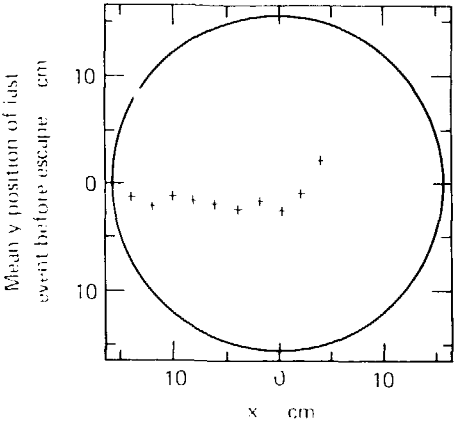

Fig. 38. Mean position of charge-exchange events generating the detected neutral-particle flux.

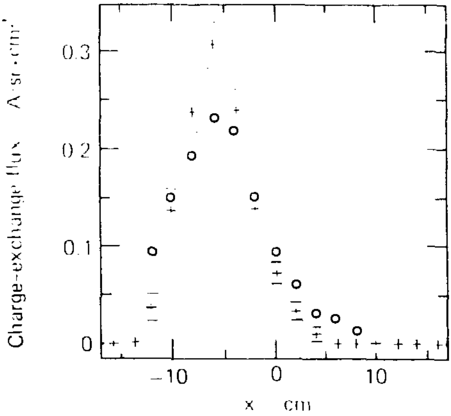

Fig. 37. Neutral-particle flux as a function of charge-exchange analyzer scan position.

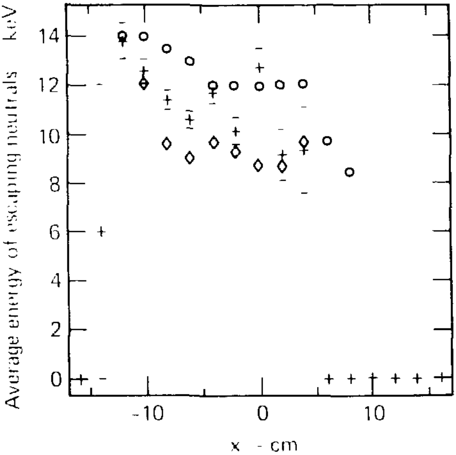

Fig. 39. Average energy of the neutral-particle flux and mean plasma energy at the mean charge-exchange source point.

for the detected flux is plotted in Fig. 38, which clearly shows that at the density used, the charge-exchange analyzers are probing the central region of the plasma.

Figure 39 gives the average energy in the observed flux as a function of scan position, with the 4/14/77 data again superimposed for comparison. Also shown is the mean plasma energy at the mean charge-exchange "source" points of Fig. 39, plotted as open diamonds.

Energy spectra are plotted in Fig. 40 for two scan positions. The solid curve is the observed spectrum of the charge-exchange flux at the indicated scan position. The dashed curve gives 2XIIB data from 4/14/77, normalized to the same total flux as seen in the code, and the dotted curve is the perpendicular energy distribution function of the target plasma at the mean position of Fig. 38. It is clear from the figures that the charge-exchange energy spectrum provides a fairly accurate characterization of the plasma distribution function at the mean interaction position.

Attenuation of the neutral beams and the fraction of beam power deposited in the plasma are given in

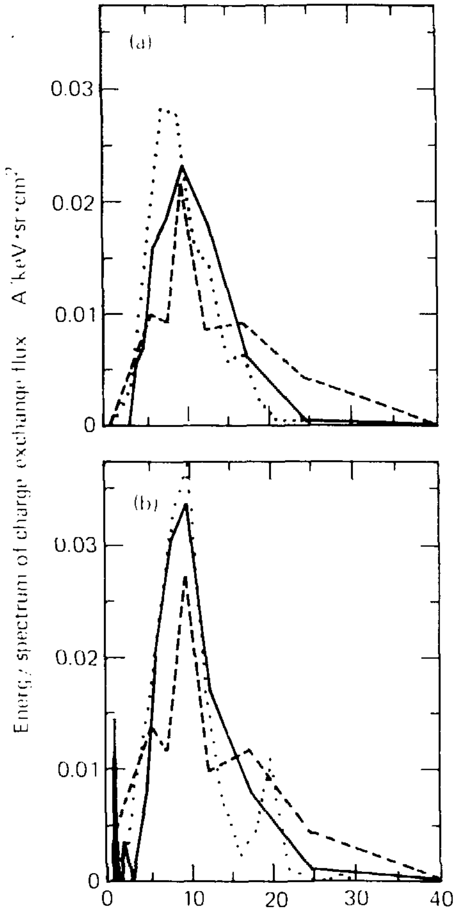

Fig. 40. Energy spectrum of neutral-particle flux and plasma perpendicular energy distribution function at mean charge-exchange source point (a) for charge-exchange analyzer scan position x = 8 cm.

Fig. 41 as a function of the plasma line density at y = z = 0. The SUPERLAYER REF17 data are indicated by the dots, the complete curves having been obtained from a series of code runs with artificially varying particle weights.

Information on the distribution of neutral particles in the plasma is presented in Figs. 42 and 43. Figure 42(a) and (b) show the azimuthally averaged line densities parallel and perpendicular to the z-axis,

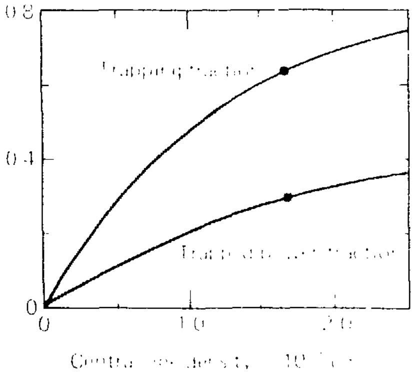

Fig. 41. Neutral-beam attenuation and fraction of beam power trapped as a function of central plasma line density.

respectively. The [illegible] Fig. 42(a) results from the [illegible] collimated incident beams. In Fig. 43 [illegible] neutral-particle energy is shown as a [illegible] radius, with the average incident energy [illegible] a dashed line.

There are two areas in which [illegible] improvement. The simpler of these [illegible] azimuthal grid to resolve θ variations in properties of the neutral-particle distribution [illegible] implemented. Methods for dealing with [illegible] increased computational efficiency are [illegible] plored. Particularly promising in this regard are the variance-reduction techniques of particle splitting and the use of control variates.

The techniques developed and used in this code have other applications as well, some of which are currently being investigated. These include:

- A neutral deposition model for SUPERLAYER.
- A neutral deposition model in the one-dimensional code being developed for reactor studies, and
- A model of wall reflux as a source of neutral particles.

Stability Studies

J. A. Byers

Application of a linearized code technique to a slab model with with strong density and field gradients in a high-β plasma has clearly shown growth in the Alvén ion cyclotron mode despite large fluctuations in the equilibrium.

The motivation here is to develop particle-simulation techniques that are applicable to a wide

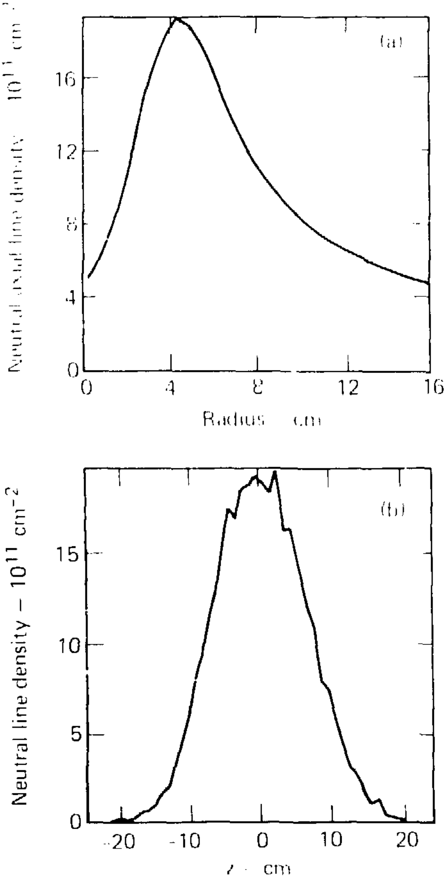

Fig. 42. **Azimuthally averaged neutral-particle line density (a) parallel to the z-axis, and (b) perpendicular to.**

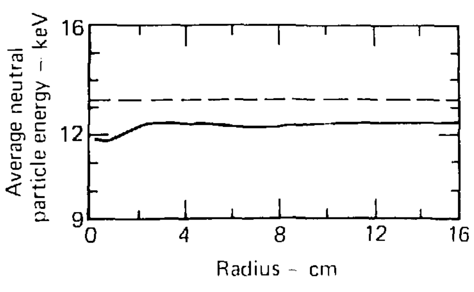

Fig. 43. **Mean neutral-particle energy as a function of radius.**

range of low-frequency ([illegible]) phenomena, including the following

- Stability of a field reversed mirror to kink modes and other gross magnetohydrodynamic (MHD) modes.
- Stability of the drift-cyclotron loss-cone (DCLC) and *Alfvén ion cyclotron (AIC) modes for high-β* plasmas with arbitrary density and temperature gradients, and fraction of cold (warm) plasma. This has application to the Mirror Fusion Test Facility (MFTF) and the Tandem Mirror Experiment (TMX).

The model is a quasi-neutral Darwin model with particle ions and fluid electrons.[illegible] In Ref. 20, we have shown that this model accurately reproduces the linear theory predictions for Alfvén waves, DCLC *modes, and AIC modes.*

$$\nabla \cdot \left(J^{i}_{\text{particle}} + J^{e}_{\text{fluid}} \right) = 0, \quad J \cdot \hat{n}_{\text{boundary}} = 0$$

$$\nabla \times \underline{B} = \frac{4\pi}{c} J \qquad \nabla \times E = -\frac{1}{c} \frac{\partial \underline{B}}{\partial t}$$

$$\text{electron fluid} \quad \underline{E} + \frac{\underline{V}^{e}}{c} \times \underline{B} = 0$$

We employ linearization to enable use of Fourier analysis and the examination of a single mode

$$\begin{aligned}
\underline{E} &= E^{0} + E^{1}, \\
\underline{B} &= B^{0} + \underline{B}^{1}, \\
J &= \underline{J}^{0} + \underline{J}^{1}, \\[6pt]
\underline{X}_{\text{ion}} &= \underline{X}^{0} + \underline{X}^{1}, \\
\underline{V}_{\text{ion}} &= \underline{V}^{0} + \underline{V}^{1}.
\end{aligned}$$

We *have previously* used this linearized code technique to demonstrate that the AIC mode in a finite-length model shows stabilization by short plasma length.[21] We have new results for the AIC mode (linear polarization – no electron effects) in a *slab model with strong density* and field gradients perpendicular to B_0. AIC growth is clearly observed despite large fluctuations in the equilibrium. We find (Figs. 44 through 46) that higher β reduces the growth rate in contrast to the infinite-medium theory, where increasing β is destabilizing. The equilibrium is typified by a sharp density gradient, where the density falls to zero over a distance $\sim 2\rho_i$. In the high-β case, the magnetic field increases by a factor of 3 from inside the plasma to outside, again over a very short scale length, $\sim 2\rho_i$. We also see an increase in the perpendicular wave number as we

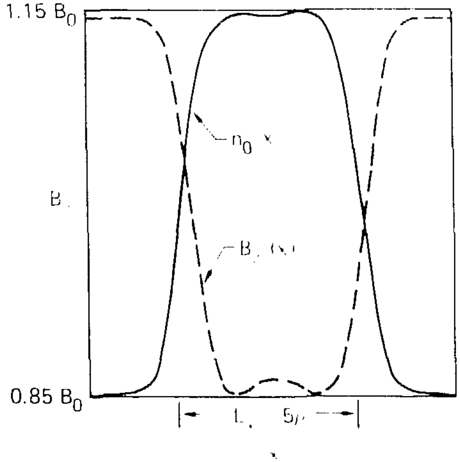

Fig. 44. Equilibrium density and magnetic field profiles, where β_{max} 0.6 and L [illegible].

increase β. The high-β case has $k_y\rho_i \sim 1$ with the mode amplitude peaking on either side in the region of the peak gradients of density and magnetic field. This result is a strong departure from the infinite-medium theory, which indicates only weak stabilizing effects from finite $k_y\rho_i$.

External Quadrupole Field in SUPERLAYER

B. I. Cohen and W. C. Condit

In a continuing effort to resolve discrepancies between results from 2XIIB experiments and SUPERLAYER II particle simulations, we have included the applied quadrupole magnetic field in SUPERLAYER II; new results are qualitatively encouraging though quantitatively inconclusive.

We are continuing the effort to resolve discrepancies between 2XIIB experimental results and those obtained in SUPERLAYER II particle simulations. One of the principal discrepancies concerns the plasma length in high-β, unreversed configurations ($\Delta B/B_0 \lesssim 1$), which SUPERLAYER apparently underestimates. For reasons outlined below, the externally applied quadrupole magnetic field in the experiment (previously omitted in the computer simulations) may be the physical mechanism that accounts for part of this discrepancy and may also be responsible for a number of other significant features. We have included the applied quadrupole magnetic field in SUPERLAYER and so far have found qualitative confirmation of a number of interesting effects, including elongation of the plasma. However, at present these simulations are quantitatively inconclusive, due primarily to the artificial acceleration of drag and rf turbulent diffusion. The latter precludes the occurrence of certain very important resonances in the particle orbits associated with the quadrupole magnetic field (see the immediately following article).

Our inclusion of an external quadrupole magnetic field in the SUPERLAYER II was motivated by the several known effects that an externally applied

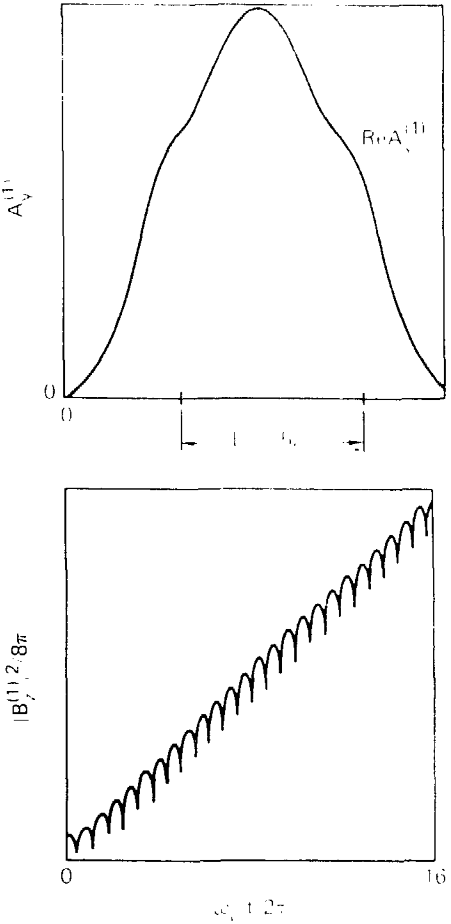

Fig. 45. Linear eigenfunction and linear rate of growth for the equilibrium case of Fig. 44, β_{max} 0.6, L_x/L = ∞. For a mode with $k_y\rho_i$ = 1, we measure a linear growth rate γ/ω_{ci} 0.24 [γ/ω_{ci} ($L_x \to \infty$) = 0.3].

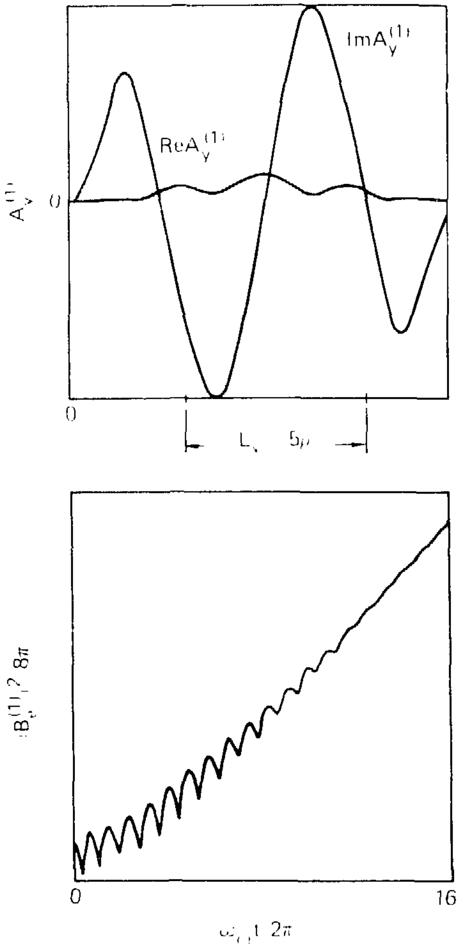

Fig. 46. Linear eigenfunction and linear rate of growth for an equilibrium with $\beta_{max} = 3$. For a mode with $k_y\rho_i = 1$, we measure a linear growth rate $\gamma/\omega_{ci} = 0.1$ [$\gamma/\omega_{ci}(L_x/\rho_i) = 0.6$].

magnetic quadrupole field has on a high-β mirror plasma:

- Quadrupole magnetic fields are necessary to stabilize the dissipative precessional mode in energetic ring-plasmas.
- Multipole components of the vacuum magnetic field in a mirror machine are necessary to provide the closed, nested |B|-surfaces required for confinement.
- Recent experiments on strong electron rings have demonstrated anomalous particle losses in the presence of an external quadrupole magnetic field.

SUPERLAYER II is now a six-dimensional phase-space description of particle ions ($r,\theta,z,v_r,v_\theta,v_z$) and charge-neutralizing electrons. To lowest order in the quadrupole magnetic field component over the mirror field component, the plasma self-fields are axisymmetric, i.e., we ignore the self-consistent quadrupole perturbation

$$\nabla^2 A_\theta = -\frac{4\pi}{c} J_\theta$$

$$A_r = A_z = J_r = J_z = 0$$

$$E_\theta = -\partial A_\theta/c\partial t, \quad E_r = E_z = 0,$$

$$dv_e/dt = e/m\,(E + v \times B/c) + \text{drag on electrons}$$

$$B = \nabla \times A + B_0^{\text{mirror}} + B_{\text{quad}},$$

$$\left\langle A_\theta J_\theta \right\rangle = \frac{1}{2\pi}\int_0^{2\pi} d\theta \left(A_\theta J_\theta\right),$$

$$B_{\text{quad}} = r\,\frac{dB_{\text{quad}}}{dr}\,(\cos 2\theta\,\hat{r} - \sin 2\theta\,\hat{\theta})$$

$$\frac{d}{dt}\left[r\left(mv_\theta + \frac{e}{c}A_\theta\right)\right] = \frac{ev_z}{c}\,r^2\,\frac{dB_{\text{quad}}}{dr}\cos 2\theta$$

$$+ \text{drag}.$$

We have carried out the following computer experiments using SUPERLAYER II with an applied quadrupole magnetic field:

- Single-particle orbits to (a) check the SUPERLAYER implementation of a quadrupole field component against TIBRO, a single-particle orbit code, and (b) to study particle orbits in three-dimensional, minimum-|B| configuration.
- Quadrupole effects on ring-like plasmas formed by neutral-beam injection: (a) the $V_\theta \times B_{\text{quad}}$ force elongates the plasma axially (in $\hat{z}$); (b) the plasma is spatially more diffuse, and axial and radial loss is aggravated; and (c) shallower self-magnetic well results.
- For neutral-beam injection studies with 2XIIB plasma parameters ($B_0 \approx 0.7$ T, $dB_{\text{quad}}/dr \approx 0.0175$ T/cm, mirror ratio = 1.2), quadrupole effects were not as significant as for ring-like cases. Elongation is less pronounced; quadrupole effects on the ion orbits and on the plasma loss are somewhat masked by artificially accelerated drag and rf turbulence. However, the self-magnetic field is shallower with the applied quadrupole field on.

Orbital Resonances and Anomalous Losses from Rings in Quadrupole-Stabilized Mirror Fields

R. H. Cohen

A quadrupole field in a mirror machine can couple the radial, axial, and azimuthal motions of single

particles to produce orbital resonances. Using a model Hamiltonian, we have demonstrated this coupling, derived expressions for resonance positions and widths in action space, and have indicated how these resonances may account for bursts and additional anomalous losses observed in the Cornell RECE-Berta experiment.

Experiments on electron rings trapped in a magnetic field in the relativistic electron compression experiment (RECE-Berta) at Cornell indicate anomalous losses when an external quadrupole Ioffe field B is added to the basic axisymmetric field B. The losses include both bursts at two particular field-reversal levels and enhanced steady state losses between and above those levels. The experimenters have suggested that these losses might be due to orbital resonance effects and that such resonances could affect one's ability to attain field reversal in 2XIIB. We have used model Hamiltonians to demonstrate that the quadrupole field is effective in coupling harmonics of the radial, axial, and azimuthal motions of particles, and that the resulting resonance structure can account qualitatively for the phenomena observed in RECE-Berta.

We assume that the charged-particle Hamiltonian can be linearized in the quadrupole field strength in the form $H \approx H_0(p, r, z) + H_1$, with $H_1 = -(q/mc)\,p_r A_r$. We take $A_r = B_q(r - r_0)\sin 2\theta$, where B_q is the quadrupole field strength at $r = r_0$. As our first model, we expand H_0 about a circular orbit $r = r_0(p_\theta), z = 0$:

$$H_0 = \frac{1}{2m}\left\{ p_z^2 + p_r^2 + \frac{(p_\theta - \frac{q}{c}\Psi_0)^2}{r_0^2} + \frac{q^2}{c^2} B \left[\Psi_{rr}(r - r_0)^2 + \Psi_{zz} z^2\right]\right\} \tag{13}$$

where $\Psi(r,z)$ is the flux function for the axisymmetric mirror field, $\Psi_0(p_\theta) = \Psi(r_0, z = 0)$, and $r_0(p_\theta)$ is determined by the relation $p_\theta + (q/c)(\Psi_0 + r_0 \Psi_{r_0}) = 0$. Subscripts r and z on Ψ denote partial derivatives. The fully nonlinear Hamiltonian H_0 can itself couple radial and axial oscillations (this gives rise to magnetic moment nonconservation in axisymmetric mirrors). The model Eq. (13) is useful in that it isolates the effect of the quadrupole field.

We determine the resonance structure of the Hamiltonian following Chirikov. We first make a canonical transformation to the action-angle variables of H_0, $(I_r, I_z, I_\theta = p_\theta, \phi_r, \phi_z, \phi_\theta)$. The transformation from θ to the canonical angle ϕ_θ introduces even harmonics of ϕ_r and ϕ_z in H_1; the transformation of r introduces s ϕ_r and $2\phi_z$ terms; the transformation of p_r introduces an odd harmonic of ϕ_r. Consequently, H_1 is a sum of terms proportional to $\cos(2\phi_\theta + m\phi_r + n\phi_z)$, where n takes on all integer values and m must be odd. Resonance occurs when one of the phases is slowly varying, i.e., when:

$$\dot{\Phi} = 2\dot{\phi}_\theta - M\dot{\phi}_r - N\dot{\phi}_z \approx 0 \tag{14}$$

The width of the resonance layer may be found by making another canonical transformation to explicitly include the slowly varying phase Φ as an angle variable, and then dropping all rapidly varying terms from H_1. The new "resonance Hamiltonian" H has the property that the new momenta $I_r' = I_r + Np_\theta/2$, $I_z' = I_z + Mp_\theta/2$ are constants. H is effectively one-dimensional. A plot of p_θ vs Φ for a range of initial conditions would exhibit fixed points at resonance, closed contours around the fixed points, open curves unbounded in the Φ direction further away, and a separatrix in between. The width of the separatrix and hence of the resonant layer may be found approximately by expanding H in the nontrivial momentum variable about its resonant value. In terms of p_θ, we find

$$\Delta p_\theta = 2\left\{ \frac{q B_q m v_{z0} I_r^{1/2} R_{MN}}{2 - \frac{q r}{2 q B^{1/2} \psi_{rr}}\left[\frac{N \partial_r(B\psi_{zz})}{\psi_{zz}^{1/2}} + \frac{M \partial_r(B\psi_{rr})}{\psi_{rr}^{1/2}}\right]} \right\}^{1/2} \tag{15}$$

where $B = B_z(z = 0, r_0)$, and $v_{z0} = v_z(z = 0)$ and where

$$R_{MN} = \sum_{lmn} \cdots (2m \ldots M \; 2l \ldots N)\, J_m(X_r) J_l(X_z) C_n ,$$

with $X_r = [cI_r/(2qrB\Psi_{rr})]^{1/2}/(B\Psi_{zz})$, and $C_1 = 1$, $C_{-1} = 2cI_r/(qrB\Psi_{rr})$, $C_{\pm 3} = 2C_{\pm 1}$, $C_n = 0$ for other values of n. Here $\omega_r, \omega_z = 1$, and I_r, I_z are the radial and longitudinal actions for the Hamiltonian [Eq. (13)]. The most important features of Eq. (15) are that Δp_θ depends on B_q and decreases fairly quickly with M and N because of the behavior of R_{MN}.

The anomalous losses in RECE-Berta are present for all nonzero quadrupole field strengths; there is apparently no threshold. This rules out explanations based on gross stochasticity of much of phase space caused by resonance overlap, since the resonance widths shrink to zero with B_q. Instead, we may seek an explanation in terms of the location of the resonant layers.

The resonance condition [Eq. (14)] may be cast in the form

$$[illegible] \qquad (16)$$

If we assume the plasma is monoenergetic (a reasonable first approximation for RECE-Berta) and ignore the [illegible] term, the resonances and constant energy curve may be plotted on the coordinates ([illegible]) and ($B_{[illegible]}$/B [illegible]), where B[illegible] = B(r[illegible]) and r[illegible] satisfies [illegible]. In these coordinates, the constant energy curve (along which a particle moves under the influence of H_1) is a constant independent of changes in the field.

Resonance plots are shown in Fig. 47 using a model field in which Ψ = const × r² × [1 − δ exp(−z²/L² − r²/a²)] and parameters appropriate to RECE-Berta, for two values of the field reversal parameter. As δ is lowered (i.e., as time in the Cornell experiment is advanced), resonances, and also the plasma "border" ([illegible] vs μ for particles bouncing at z = L), move to the left. (We refer always to positions along the constant energy surface.) Most resonances move to the left faster than the border of the plasma moves, and hence move from outside to inside the plasma region. An exception is the M = 1, N = 2 resonance, which slowly drifts to the right relative to the plasma border. Because of their finite width [Eq. (15)], resonance lines are really resonance layers. Therefore, we expect a burst when a resonance crosses the plasma border, as particles near the edge of the plasma suddenly have an easy path away from the confinement region. At δ = 0.6 [Fig. 47(a)], the closely spaced pair of resonances M = 3, N = 1, and M = 5, N = 0 have just crossed the border. Furthermore, they have also just crossed the M = 1, N = 2 resonance, so that some local stochasticity due to resonance overlap is assured, even for small B_q. As δ is lowered, the next border crossing for a low order resonance (low M,N) occurs at δ = 0.3 [Fig. 47(b)], again a multiple coincidence because the M = 7, N = 0 resonance is near crossing both the plasma border and the M = 1, N = 2 resonance. For lower values of δ, other resonances intersect the plasma edge, but the resonance widths are smaller, and there are no further simultaneous intersections with low order resonances. As δ is increased beyond the value at which the (M,N) = (3,1) resonance crosses the plasma border, there are no further crossings; the (3,0), (1,0), and (1,1) resonances enter the diagram from the left and then remain inside the plasma past the value of δ where the field is reversed at r = r[illegible]. Hence only two sizable bursts would be expected in RECE-Berta.

As δ is decreased below a burst value, the resonance or resonances that had just crossed into the plasma move inward and eventually reach [illegible] = 0 with zero width and disappear. While a resonance is in the interior of the plasma, it acts to slightly enhance the loss rate by reducing the distance in velocity space through which an electron must classically diffuse. This effect would tend to enhance the electron loss rate over classical by an amount proportional to B_q (proportional to the resonance width). An additional effect is that nonresonant electrons experience small oscillations in p_z with amplitude proportional to B_q. There are higher order resonances whose contribution to the loss rate enhancement would vary as B[illegible]. It is not yet clear to us what the net scaling should be, and hence we do not know whether the resonance picture is consistent with the between-burst scaling in RECE-Berta, which appears to be roughly linear.

The model given by Eq. (13) underestimates the size of J = 1 resonances because the variation of r during an axial bounce is ignored. This has been verified by the consideration of a second model Hamiltonian $H = p_z^2/2m + \mu B(z)$, where μ is magnetic moment (here, in evaluating H, it is assumed that r(z) is on a flux surface). This model does not contain radial oscillations, and so is restricted to N = 0 resonances.

Because H is completely integrable, the model Eq. (13) does not allow for nonadiabatic behavior in the axisymmetric field. For large orbits that are not nearly concentric with the axis, coupling of radial and z motion may result in stochastic behavior for μ, limited only by constraints of p_θ conservation. When a quadrupole perturbation is added, p_θ jumps by an amount proportional to B[illegible] with each jump in μ. The resulting collisionless diffusion would vary as B_q and would be independent of the collision frequency (in contradiction with RECE-Berta results).

Resonances might have a measurable affect in 2XIIB, but only at significantly higher values of the field reversal parameter (perhaps [illegible] 1) owing to the increased ratio of plasma length to radius. Resonance would not manifest itself in bursts, because of the nonmonoenergetic nature of the distribution. We shall explore this application further.

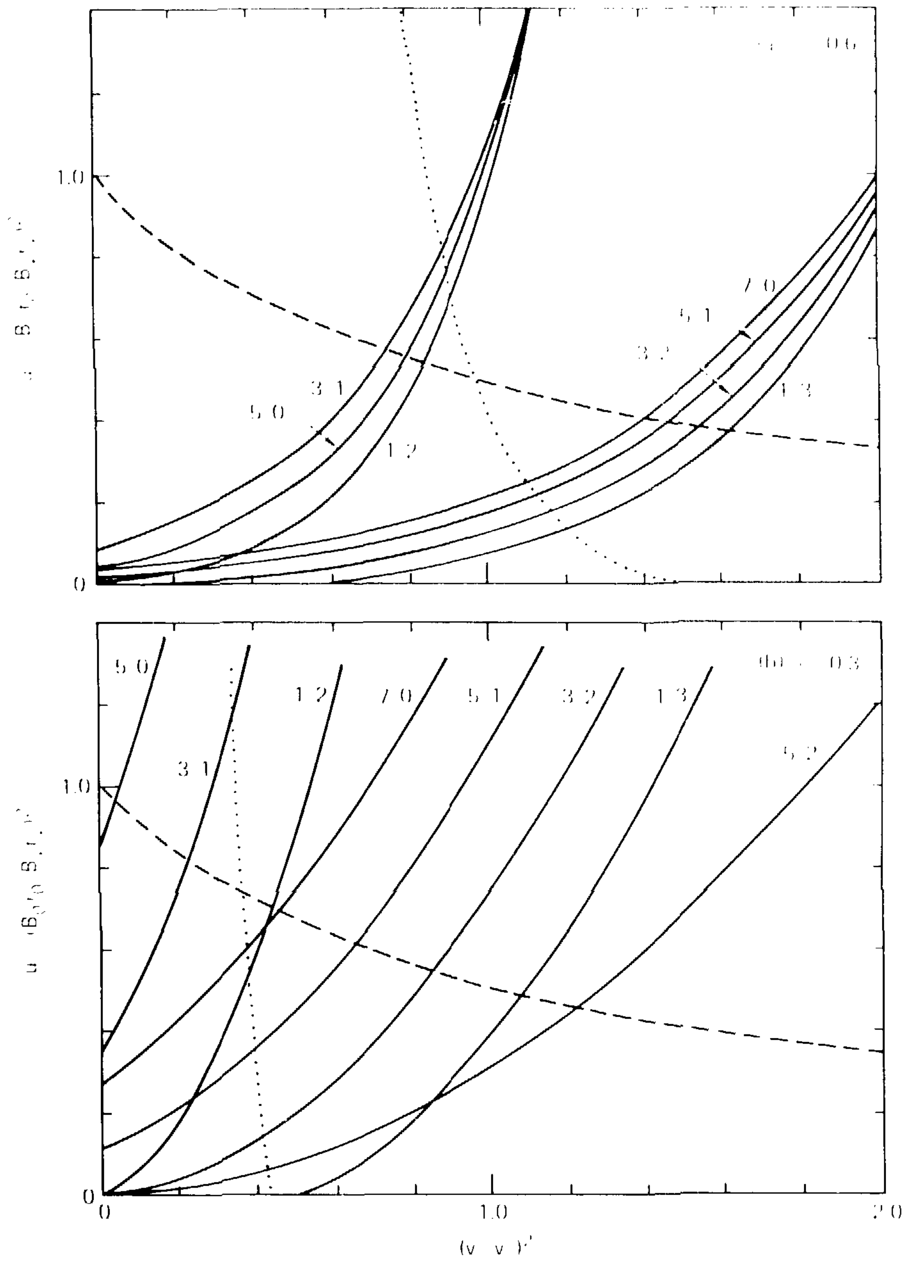

Fig. 47. Resonance diagrams for Ψ = $(B_0 r^2/2)[1 - \varepsilon\exp(-z^2/L_z^2 - r^2/L_r^2)]$, with L_z = 11 cm, L_r = 16 cm, and r_w = 9 cm. Solid curves are resonance lines; the dashed curve is the constant-energy line; and the dotted line is the "plasma border," which is defined as the locus of u, $(v_\parallel/v_\perp)^2$ values for particles turning at $z = L_p$. Resonance curves are labelled by M − N.

Our plans for future work are aimed at making the theory quantitative: numerically evaluating resonance widths from Eq. (15), estimating the fraction of phase space occupied by resonances and the resulting diffusion (Arnold and enhanced collisional), and using more realistic field models and a better approximation to the axisymmetric Hamiltonian H. We shall also explore loss due to resonances in the near the types of loss boundaries (for example, that are due to a radial limit r).

Code for Warm Plasma Flow through Mirrors

T. D. Rognlien

A new version of the axial-flow code PHLOW[6] is *about four times faster than the old code.*

We have rewritten the axial-flow code PHLOW using a first order implicit numerical algorithm. The new version is now working, and it is about four times faster than the former explicit version of the code using the same time step. Since the implicit version of the code should not be limited by the Courant time-step restriction, we are investigating the larger time-step regime for an even greater increase in code speed.

While developing the implicit algorithm, we did *encounter numerical instability.* This difficulty was traced back to the equation for the velocity, whose advective part is

$$\frac{\partial u}{\partial t} + u\frac{\partial u}{\partial z} = \text{other terms}$$

The straight-forward differencing

$$\frac{u_i^{n+1} - u_i^n}{\Delta t} + u_i^n \frac{u_{i+1}^{n+1} - u_{i-1}^{n+1}}{2\Delta z}$$

leads to grid-dependent oscillations in u. Using a Lax-type differencing of the first term gives a stable scheme; i.e.,

$$\frac{\partial u}{\partial t} \approx \frac{u_i^{n+1} - 0.5\left(u_{i+1}^n + u_{i-1}^n\right)}{\Delta t} .$$

This scheme is known to produce diffusion, which is the reason for its stable properties. An attempt was made to "upwind" difference the nonlinear convective term in the first scheme, but this did not seem to improve stability.

Startup in TMX

R. H. Cohen

The tandem mirror rate code TAMRAC has been used to evaluate startup schemes for the Tandem Mirror Experiment: the best appears to be one in which the gas feed in the solenoid is programmed to *allow a few ms of injection at several times the* steady-state value.

We have explored startup schemes for TMX using the tandem mirror rate code (now named TAMRAC).[5] To this end, the code has been modified to *include externally supplied streaming plasma in the* plugs and to correctly calculate electron end losses when the center cell is empty.

The goal is to start the TMX machine so as to arrive at nearly steady-state parameters during the 25 ms that the 40-keV beams can be on. We assume the following:

- The plugs must be built up before the solenoid in order to provide MHD stability for the solenoid,
- Streaming plasma is available to provide DCLC stability for the plugs during this process (but only *for about 8 ms), and*
- The steady-state values should be approximately those of Table 1 in the TMX proposal.[5]

The basic strategy is to build up the plugs with 20-keV beams and stream on, then build up the center until end losses (losses from the center cell and a marginal stability loss rate from plugs) can provide the DCLC stabilizing flux, and then switch to 40-keV beams and turn the stream off. The code is run in its "DCLC option," where the plug loss rate is enhanced to make up the difference between end losses (and stream, *if on) and the flux required for* DCLC marginal stability. When the stream is on, it is assumed for purposes of determining Γ that the stream penetrates only in the amount necessary to provide for DCLC stability, and that each penetrating stream electron causes energy $(3/2)T_e + 2\phi$ to be lost from the plug electrons.

The principal conclusion of the study is that a near-steady state can be achieved within the allowed time scales, but only if the gas feed in the solenoid is programmed to allow a few ms of injection at several (5 to 10) times the steady-state value. A *suitable* scheme is shown in Table 5 and Figs. 48 and 49.

The problem with a single-level gas feed is that the solenoid builds up too slowly to allow the stream to be shut off after 8 ms. If, with single-level gas feed, the stream is shut off after 8 ms (Figs. 50 and 51), much of the plug density is lost due to DCLC instability, endangering the MHD stability of the solenoid. TAMRAC ignores MHD instability and so indicates that the system recovers after another 25 ms.

An alternative to programmed gas feed is to run the plugs with 20-keV beams and an externally supplied stabilizing flux for a lengthly period of time

Table 5. Parameters and Results for Programmed Gas-Feed Run (Figs. 48 and 49)

Machine parameters (p plug, c central cell, solenoid)

L_p 400 cm L_s 5.5 m B_p/B_s 20 B_{throat}/B_s 40 (πr^2) 0.307 m²

Sources (all currents are for ions, not neutrals)

Plugs 16 A (both plugs) at 40 keV (26 keV mean) or 40 A at 20 keV (13 keV mean)

Solenoid current J_s given below E_{inj} 1 eV

Stream current adjusts to minimum needed for DCLC E_{inj} 1 eV

Electrons E_{inj} 1 eV

Charge-exchange cross section/ionization cross section 2 in plugs, 1 in solenoid

t(ms)	n_p(10^{13}cm^{-3})	n_s(10^{13}cm^{-3})	$E_\perp$(keV)	T_s(eV)	T_e(eV)
0	10^{-4}	10^{-4}	10^{-3}	1	1
Stream on, 20-keV beams, J_s = 0					
4	4.92	10^{-4}	13.6	1	155
Stream on, 20-keV beams, J_s = 800 A					
8	4.75	1.20	14.3	25.9	111
Stream off, 40-keV beams, J_s = 137 A					
23	4.95	1.24	28.4	55.8	231
34	5.06	1.27	28.2	87.8	233
∞	5.22	1.29	28.0	90.7	235

(26 ms, in our example) after the solenoid gas feed is turned on (Figs. 52 and 53). The stabilizing flux could be supplied initially by stream and later by gas feed boxes mounted in the plugs or in the ends of the machine, as in 2XIIB. This scheme has the disadvantages of requiring that power be supplied to the 20-keV beams for a long period of time, and of requiring a separate gas feed for the plugs. It has the advantage of a simpler gas feed in the solenoid.

The scheme in Figs. 54 and 55 is similar to that of Figs. 48 and 49, except that the plugs are switched from 20- to 40-keV beams at the same time that the solenoid gas feed is turned on, rather than waiting until the solenoid has built up. The scheme of Figs. 48 and 49 appears to be slightly preferable in terms of the time the 40-keV beams must be on before steady state is approached.

Negative-Ion Charge-Exchange Cross Sections

J. R. Hiskes and Karo

New calculations are providing an accurate model for charge exchange suited to both alkali and alkaline-earth targets for negative-ion formation.

The conversion of positive deuterium ions to negative ions by deuterium collisions in cesium vapor has been demonstrated to give large yields for energies down to 200 eV, and with no indication of falling yields at lower energies. Current theoretical cross sections would indicate lower yields at these lower energies, and extrapolation downward in energy is uncertain. As a basis for providing new and accurate cross sections, we have initiated calculations based upon the perturbed stationary-state method taken together with the impact parameter formulae. This method relies upon an expansion of the total wave function in a set of molecular states and a reduction of the problem to a set of coupled equations, with the coupling coefficients determined by matrix elements of certain operators between electronic states. Determination of accurate cross sections will require both precise energy levels and molecular functions. The ground-state functions already calculated provide an initial basis for improving earlier calculations. The set of coupled equations leading to charge-exchange capture cross sections has been derived in a form suitable for numerical integration.

Some time earlier, we noted that the alkaline-earths may also be suitable targets for negative-ion formation. These equations will provide for an accurate model suited to both alkali and alkaline-earth targets.

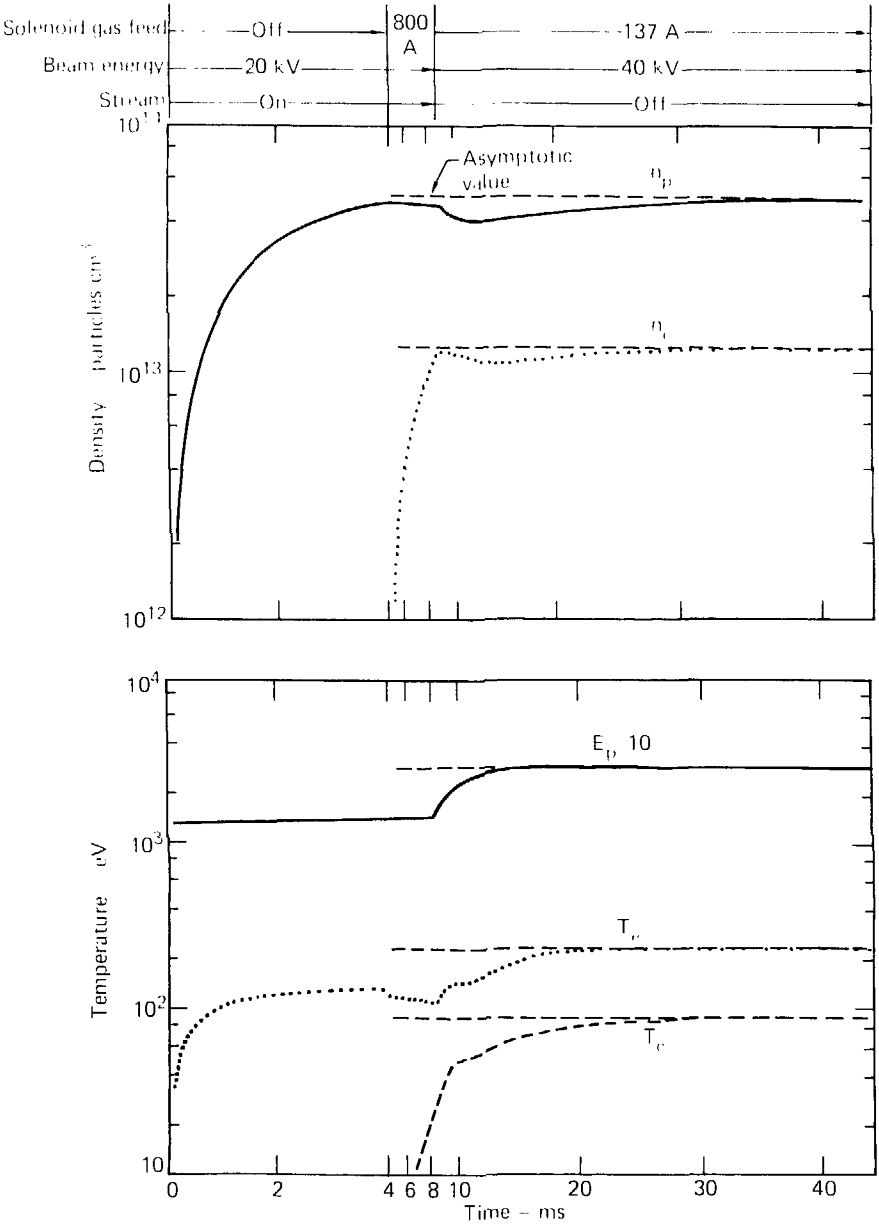

Fig. 48. Densities, mean plug energy, and electron and solenoid ion temperatures for a run with a 4-ms period of 800-A gas feed.

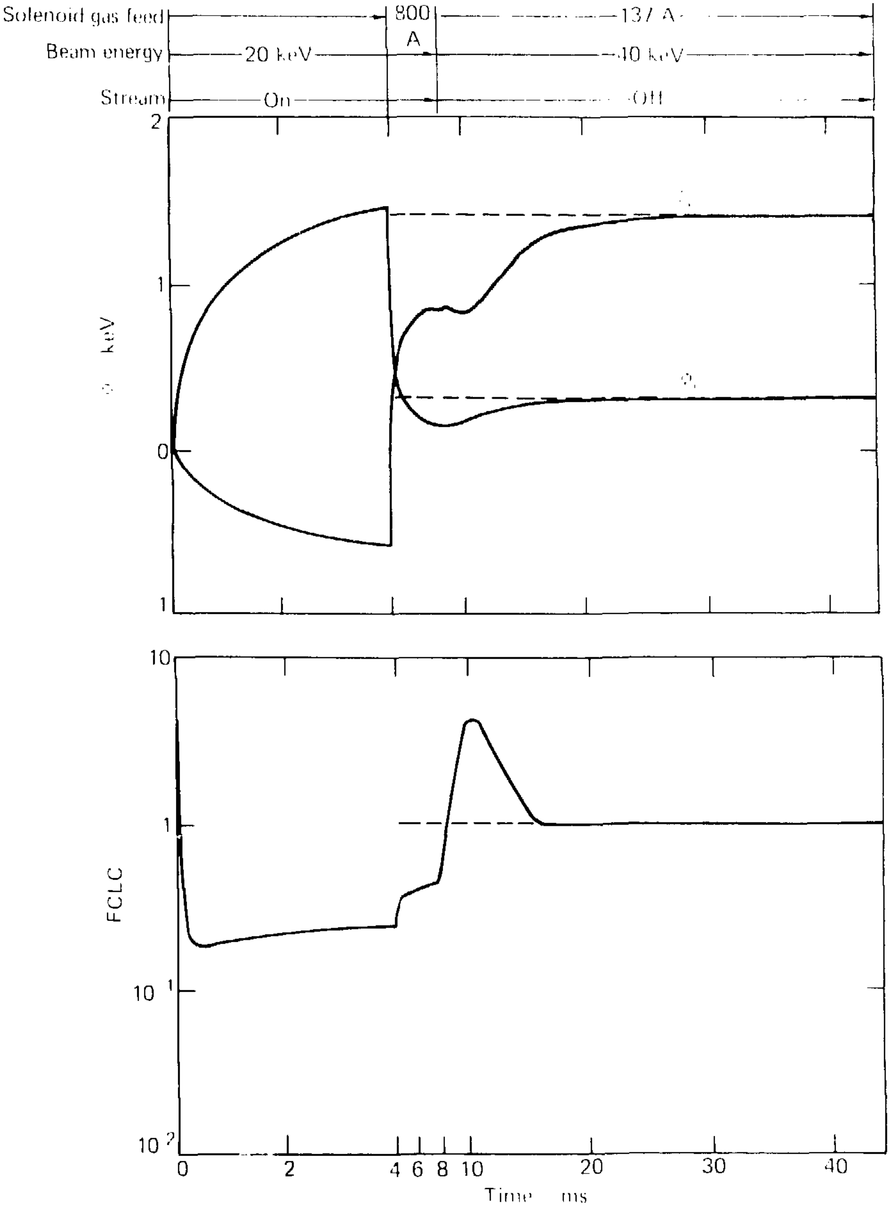

Fig. 49. Potentials and FCLC for same run as Fig. 48, where ϕ_t is the potential difference between plugs and the solenoid; ϕ_e is the potential difference between the solenoid and ground. FCLC is the fraction of DCLC stabilizing flux supplied by solenoid end loss plus quiescent plug loss.

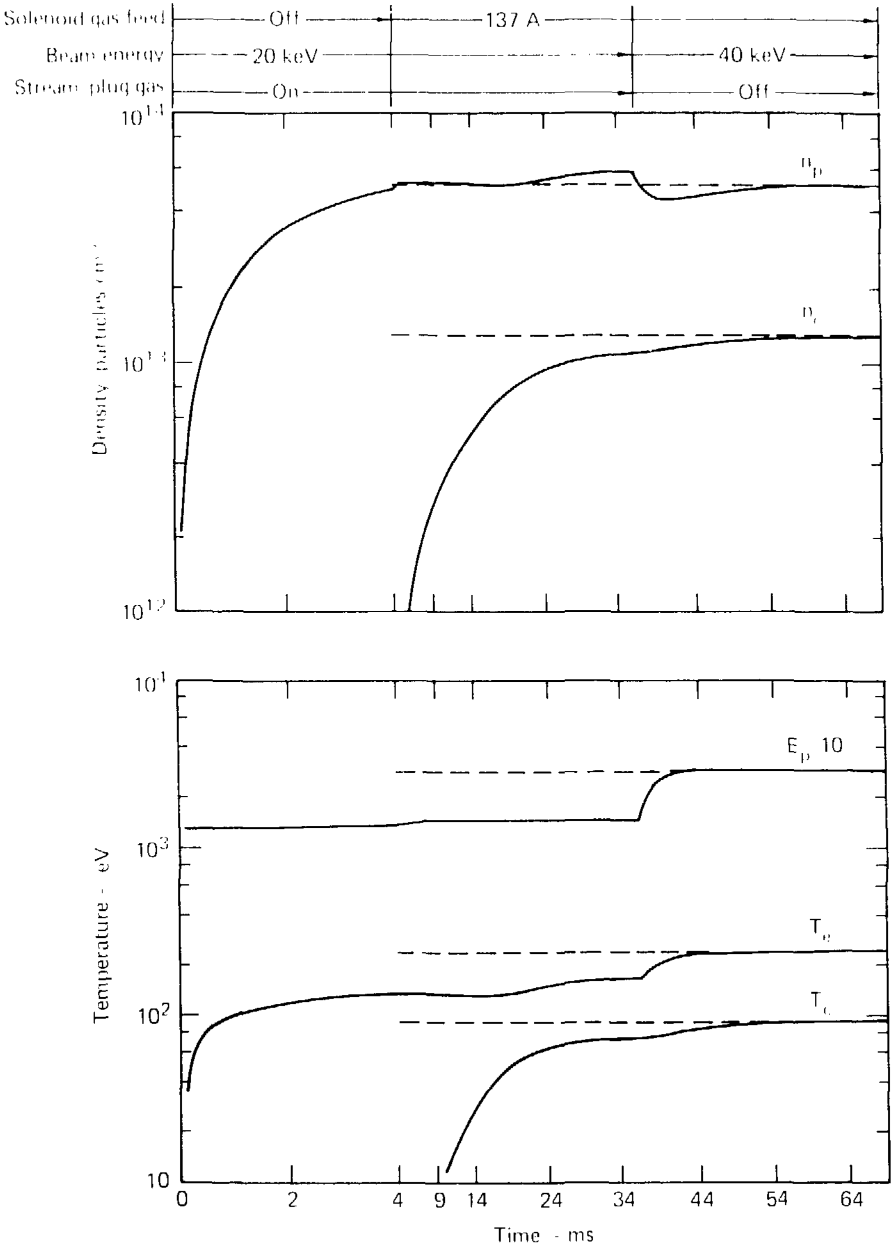

Fig. 50. Densities, mean plug energy, and temperatures for a run with only a single level of gas feed and no stream after 8 ms.

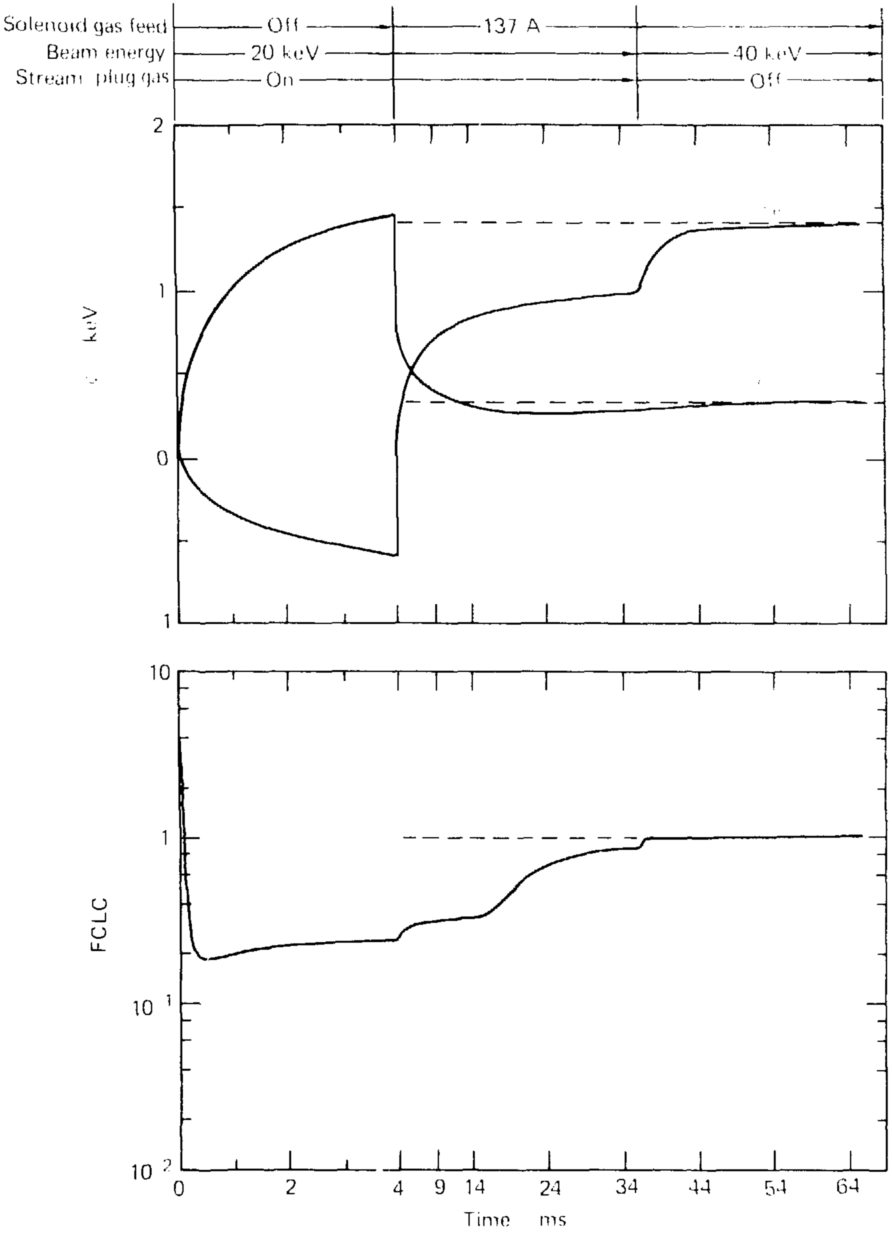

Fig. 51. Potentials and FCLC for run of Fig. 50.

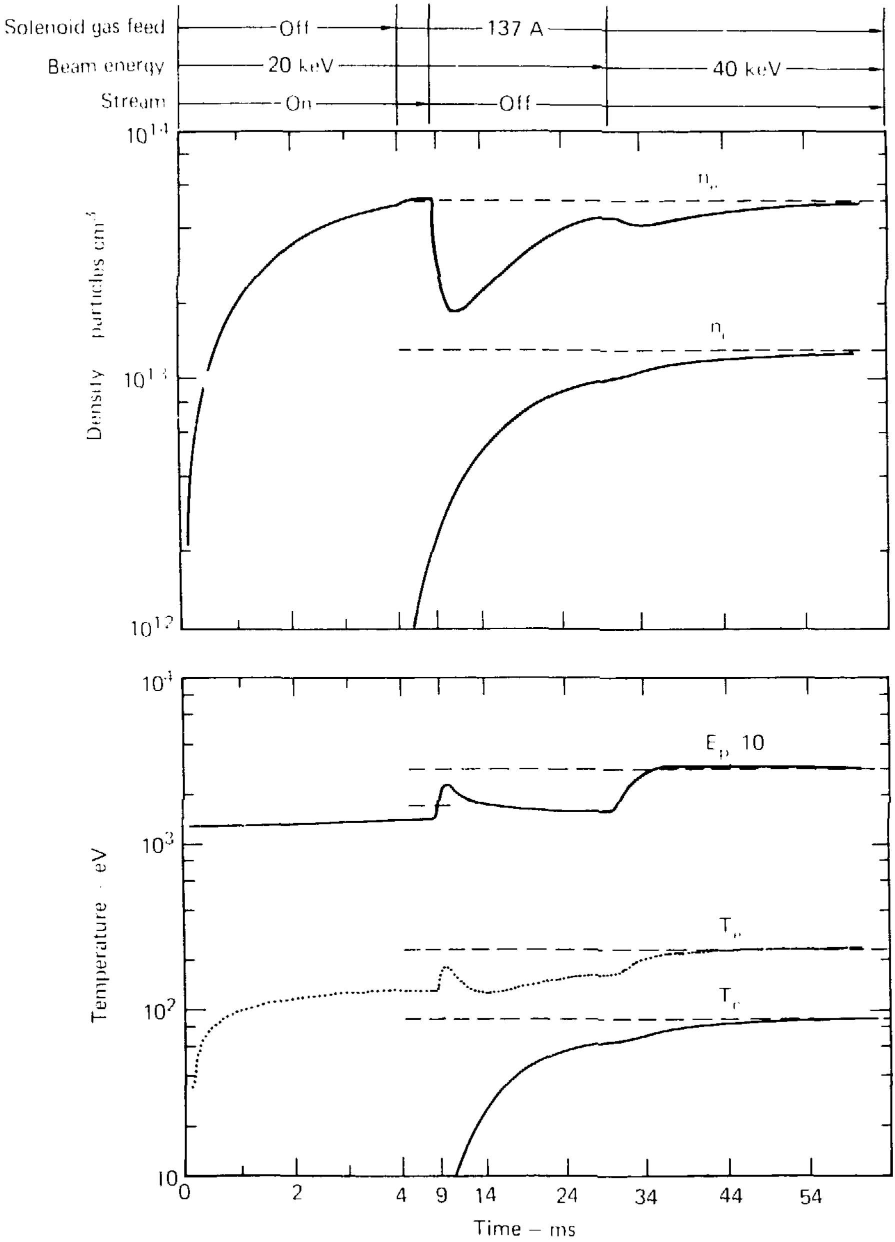

Fig. 52. Densities, mean plug energy, and temperatures for a run with a single level of gas feed and solenoid stream (or gas feed) present for 32 ms.

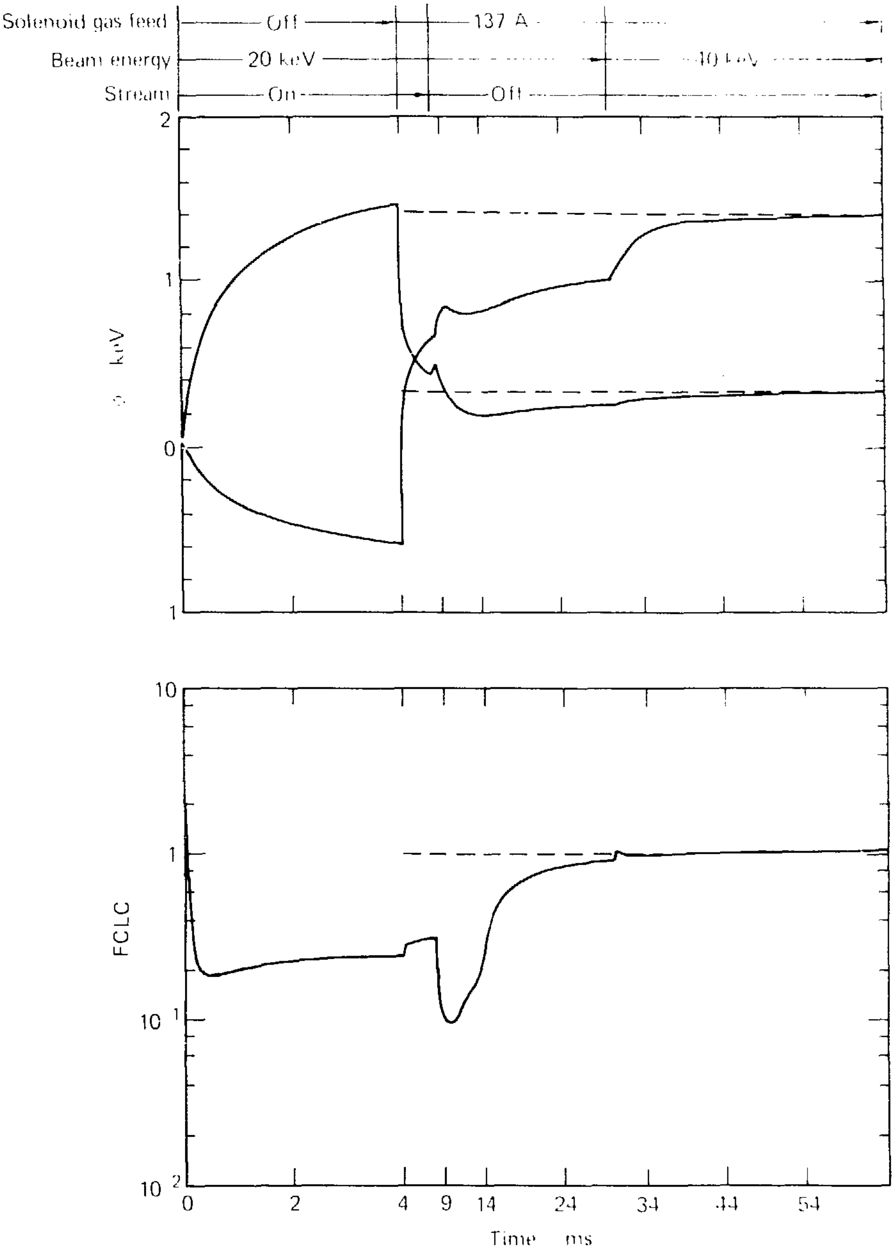

Fig. 53. Potentials and FCLC for run of Fig. 52.

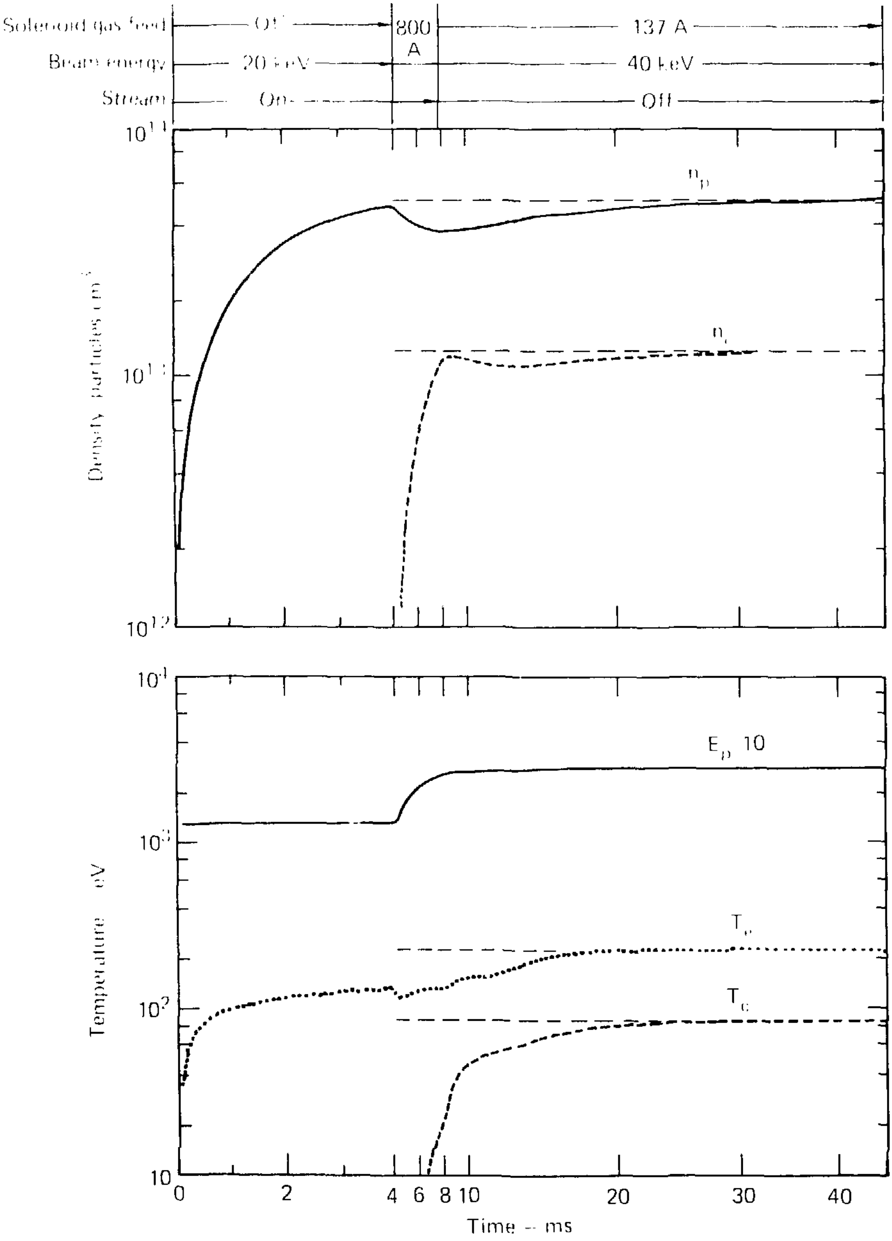

Fig. 54. Densities, mean plug energy and temperatures for a run in which the beams are switched from 20 to 40 keV when the gas feed is turned on.

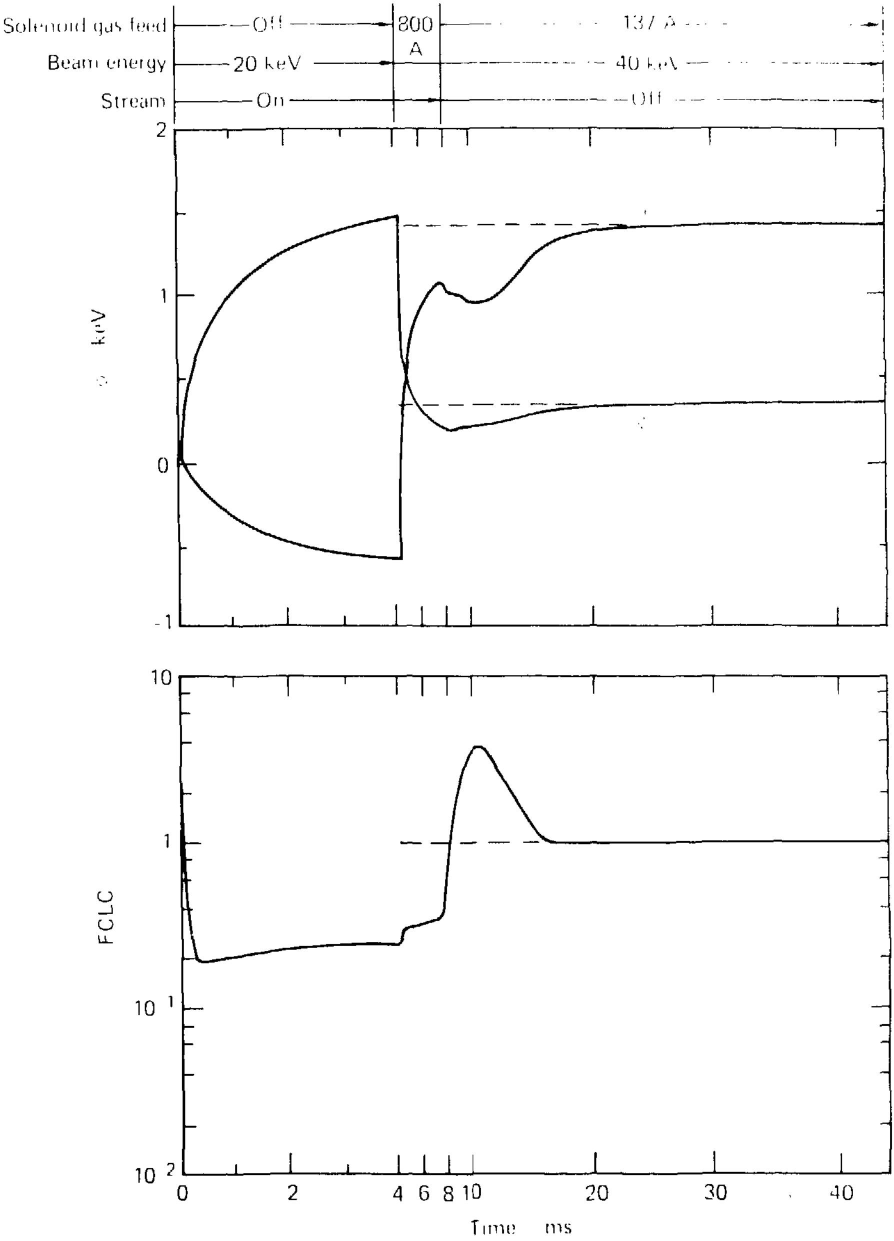

Fig. 55. Potentials and FCLC for run of Fig. 54.

Experimental Plasma Research

The Intense, Pulsed Ion-Neutral Source (IPINS)

D. S. Prono

Our principle goal is to develop intense, pulsed, neutral-beam sources (IPINS) for the mirror program. The generation of a reversed-field configuration in a 2XIIB-scale experiment with rapid (microsecond time scale) buildup times would be the main near-term application of this technology, and *the current research is focused on the achievement of* the performance levels required by this application.

During the first 3 months of FY 1978, we have concentrated on attaining an operational status for the IPINS major experimental facility. This effort has included both debugging of the major experimental facility and a diagnostic upgrade. To date all system failures (i.e., power supply malfunctions, insulator failures, etc.) have been resolved. However, as yet unresolved is a failure mode of anomalous anode-cathode plasma closure velocities that causes the ion pulse duration to be shortened. We believe that this phenomenon may be attributed either to poor beam uniformity (creating localized high energy density plasmas) or to a diode instability. Both these explanations are being investigated.

REFERENCES

1. M. A. Harrison, Scientific Editor, *Magnetic Fusion Energy Annual Report—October 1976 through September 1977*, Lawrence Livermore Laboratory, Rept. UCRL-50002-77 (in preparation).
2. C. C. Damm, J. H. Foote, A. H. Futch, R. K. Goodman, R. S. Hornady, E. E. Osher, and G. D. Porter, *Streaming Plasma Measurements in the Baseball II-T Experiment*, Lawrence Livermore Laboratory, Rept. UCRL-52279 (1977).
3. J. E. Osher and G. Melin, "A Streaming Plasma Ion Source for 2XIIB Stabilization," *Bull. Am. Phys. Soc.* **22**, 1192 (1977).
4. *F. H. Coensgen, Project Leader, TMX Major Project Proposal*, Lawrence Livermore Laboratory, Rept. LLL-Prop-148 (1977).
5. B. G. Logan, D. E. Baldwin, J. H. Foote, A. K. Chargin, R. L. Hinkle, R. O. Hussung, and C. C. Damm, *Improved Magnetic Field Line Design for TMX*, Lawrence Livermore Laboratory, Rept. UCID-17635 (1977).
6. James H. Foote, "Drift Surface Calculations for the Tandem Mirror Experiment and the Mirror Fusion Test Facility," *Bull. Am. Phys. Soc.* **22**, 1065 (1977).
7. F. H. Coensgen, Project Leader, *MX Major Project Proposal*, Lawrence Livermore Laboratory, Rept. LLL-Prop-142 (1976). [Note: The MX designation was later changed to Mirror Fusion Test Facility (MFTF).]
8. C. C. Damm, J. H. Foote, A. H. Futch, R. K. Goodman, R. S. Hornady, E. E. Osher, and G. D. Porter, *Streaming-Plasma Measurements in the Baseball II-T Mirror Experiment*, Lawrence Livermore Laboratory, Rept. UCRL-52279 (1977).
9. F. W. Grover, *Inductance Calculations* (Van Nostand, 1946), p. 110.
10. C. F. Barnett, J. A. Ray, E. Ricci, and M. I. Wilker, *Atomic Data for Controlled Fusion Research*, Oak Ridge National Laboratory, Rept. ORNL-5206 (1977).
11. T. K. Fowler, Lawrence Livermore Laboratory, private communication (1977).
12. *The ABC's of Radiation Hardening Programs*, IRT Corporation, Rept. INTEL-RT-4251-002 (1976).
13. C. C. Damm and G. D. Porter, *Suppression of Secondary Electrons in Mirror Machines by the Use of Fins*, Lawrence Livermore Laboratory, Rept. (in preparation).
14. D. W. Deis, D. H. Cornish, D. G. Hirzel, and A. R. Rosedahl, "Strain-Critical Current Data for Large Multifilament Nb_3Sn Conductors," in *Proc. Seventh Symp. on Engineering Problems of Fusion Research, Knoxville, 1977* (IEEE, 1977).
15. J. Hengevoss and E. A. Trendelenburg, *Continuous Cryotrapping of Hydrogen and Helium by Argon at 4.2 K*, Physics Research Laboratory, Balzers Aktiengesellschaft für Hochvakuumtechnik und Dünne Schichten, Balzers, Furstentum Liechtenstein (1962).
16. Lawrence Livermore Laboratory, Internal Document UCIR-1102-77-1 (1977). Readers outside the Laboratory who desire further information on LLL internal documents should address their inquiries to the *Technical Information* Department, Lawrence Livermore Laboratory, Livermore, California 94550.

17. D. R. Nethaway, R. A. Van Konynenburg, M. W. Guinan, and L. R. Greenwood, *Neutron Spectra from 30 MeV Deuterons On A Thick Beryllium Target*, Lawrence Livermore Laboratory, Rept. UCRL-[illegible] (19[illegible]).

18. H. R. Higgs and F. H. Hammad, *J. Nucl. Mater.* 55, 1[illegible] (19[illegible]).

19. R. E. Aamodt, Y. C. Lee, C. S. Liu, and M. N. Rosenbluth, "Nonlinear Dynamics of Drift Cyclotron Instability," *Phys. Rev. Lett.* 39, 1660 (1977).

20. J. A. Byers, B. I. Cohen, W. C. Condit, and J. D. Hanson, *Hybrid Simulation of Quasineutral Phenomena in Magnetized Plasma*, Lawrence Livermore Laboratory, Rept. UCRL-79437 (1977), to be published in *J. Comp. Phys.*

21. J. A. Byers, "Computer Simulation of Field Reversal in Mirror Machines," *Phys. Rev. Lett.* 39, 1476 (1977).

22. S. C. Luckhardt and H. H. Fleischmann, "Anomalous Fast Particle Losses from Strong Electron Rings in Quadrupole Stabilized Mirror Fields," *Phys. Rev. Lett.* 39, 747 (1977).

23. B. V. Chirikov, "A Universal Instability of Many Dimensional Oscillator Systems," Institute of Physics, Novosibirsk, USSR (1977), to be published in *Phys. Rep.*

24. R. H. Cohen, *Tandem Mirror Rate Code and Cyclic Burning of Alphas in Tandem Reactors*, Lawrence Livermore Laboratory, Rept. UCID-17844 (1977).

25. A. M. Karo, M. A. Gardner, and J. R. Hiskes, Ab Initio *MC-SCF Ground State Potential Energy Curves for LiH⁻, NaH⁻, and CsH⁻*, Lawrence Livermore Laboratory, Rept. UCRL-79609 (1977), to be published in *J. Chem. Phys.*

26. J. R. Hiskes, Lawrence Livermore Laboratory, Internal Document UCIR-853 (19[illegible]).

CKM